Fall 2019

Numerical Modeling and Field Investigation of Nearshore Nonlinear Wave Propagation

Elham Sharifineyestani
Old Dominion University, sharifin.e@gmail.com

NUMERICAL MODELING AND FIELD INVESTIGATION OF NEARSHORE NONLINEAR WAVE PROPAGATION

by

Elham Sharifineyestani
B.A. June 2008, University of Arak, Iran
M.S. September 2012, Sharif University of Technology, Iran

A Dissertation Submitted to the Faculty of
Old Dominion University in Partial Fulfillment of the
Requirements for the Degree of

DOCTOR OF PHILOSOPHY

CIVIL AND ENVIRONMENTAL ENGINEERING

OLD DOMINION UNIVERSITY
November 2019

Approved by:

Navid Tahvildari (Director)

Ma Gangfeng (Member)

Richard P. Hale (Member)

ABSTRACT

NUMERICAL MODELING AND FIELD INVESTIGATION OF NEARSHORE NONLINEAR WAVE PROPAGATION

Elham Sharifineyestani
Old Dominion University, 2019
Director: Dr. Navid Tahvildari

First, a phase-resolving frequency-domain wave model that solves nonlinear wave-wave interactions is improved to account for wave dissipation and modulations over viscoelastic mud layer. Model results show satisfactory agreement with laboratory measurements. The model is then used to investigate the combined effect of mud viscoelasticity and nonlinear wave-wave interactions on surface wave evolution using cnoidal and random wave simulations. In general, qualitative measures such as shape of cnoidal waves or pattern of variation in H_{rms} of random waves are dictated by direct mud-induced damping which, due to resonance effects, has a substantially different structure over viscoelastic mud compared to viscous mud. Nonlinear interactions affect spectral shape and distribution of energy loss across the spectrum. Subharmonic interactions cause indirect damping of high frequencies but ameliorate damping of harmonics around mud's resonance frequency. Therefore, neglecting mud elasticity can result in significant errors in estimation of bulk wave characteristics and spectral shape.

Next, a phase-resolving frequency-domain model for wave-current interaction is improved to account for wave modulations due to viscoelastic mud. Results indicates that copropagating currents decrease frequency-dependent damping at low frequencies while they increase it at higher frequencies. The opposite is true for counterpropagating currents. The impact of currents at high frequency increases with increase in mud shear modulus and it is observed in both monochromatic and random wave simulations. The Performance of two mud-

induced wave evolution models are compared. One model assumes that the mud layer is thin and the other is applicable to mud of arbitrary depth. It is found that a model based on thin-mud assumption overestimates damping over viscous mud in both monochromatic and random wave scenarios. However, for viscoelastic muds, this model slightly underestimates and overestimates damping for monochromatic and random wave scenarios, respectively.

Finally, a preliminary field measurement and data analysis of wave and flow over a seagrass meadow is conducted. In addition, a computational model for hydrodynamics of wave-vegetation interaction is linked to a computational biophysical model for seagrass growth. As a result of this integration, the wave-vegetation model provides improved information on leaf orientation to the seagrass growth model.

This dissertation is dedicated to my family who encouraged me to pursue my dreams: my mother who always encourages me to be a strong woman, my father who always works hard to support his family and encourages his kids to be more and more successful, my sister who is my best friend and my emotional supporter, my older brother who always encourages me to be more successful and gives me brilliant ideas, my younger brother who always gives me more hope and energy in my life, and my husband who is my love.

ACKNOWLEDGMENTS

Firstly, I would like to express my sincere gratitude to my advisor Dr. Navid Tahvildari for the continuous support of my Ph.D. study and related research. His guidance helped me in all the time of research and writing of this dissertation.

Besides my advisor, I would like to thank the rest of my dissertation committee: Dr. Gangfeng Ma and Dr. Richard P. Hale, for their time and constructive comments.

TABLE OF CONTENTS

Page

LIST OF FIGURES

Figure Page

CHAPTER 1

INTRODUCTION

Cohesive sediments are ubiquitous in coastal waters. The mud deposited in river deltas is distributed in the nearshore by waves, tides, and wave-induced, storm-driven, and ambient currents. As a result, sediments in the majority of the world's coasts are heterogeneous and mixed mud/sand sediment composition is common (Holland and Elmore, 2008). Therefore, to reliably estimate wave energy and wave-induced coastal erosion, it is essential to characterize mud behavior and its influence on surface waves accurately.

Field and laboratory experiments have shown stronger wave dissipation over mud compared to sandy beaches. Observations of Ardhuin et al. (2003) show 50-75% loss in swell energy over 100-km wide sandy beaches on the North Carolina Virginia continental shelf. In contrast, Wells and Coleman (1981) documented a 90% wave energy loss over a 20-km distance on the muddy coast of Surinam. High wave damping rates over mud have also been observed in laboratory experiments of Gade (1958), where 80% of surface wave energy was dissipated by fluid mud over only 2.6 wavelengths.

A reliable model for wave evolution over mud requires an accurate characterization of mud behavior. Different rheological models have been adopted for mud behavior, from which the most common ones are viscous fluid (e.g. Gade, 1958; Dalrymple and Liu, 1978; Ng, 2000), viscoelastic medium (e.g. Macpherson, 1980; Hsiao and Shemdin, 1980; Maa and Mehta, 1990; Jiang and Mehta, 1995; Zhao et al., 2006; Liu and Chan, 2007; Mei et al., 2010), and Bingham plastic (Mei and Liu, 1987; Chan and Liu, 2009). It should be noted that all these theoretical models are based on linearized equations of motion. Dalrymple and Liu (1978) developed a

theory for waves propagating over a mud layer of arbitrary depth topped by a layer of water. In most shallow coastal areas, the mud layer is typically much thinner than the overlying layer of water and this allows for derivation of approximate analytical solutions for surface wave-mud interactions (Mei and Liu, 1987; Ng, 2000; Mei et al., 2010). Ng (2000) obtained an analytical solution for the case where the mud layer is thin and is of the same order of magnitude as the bottom boundary layer. The same thin mud assumption was applied by Liu and Chan (2007) to viscoelastic mud. In a viscoelastic medium, viscosity dissipates wave energy while elasticity acts as a restoring force that modulates frequencies (Macpherson, 1980). Viscoelastic media are particularly significant due to the possibility of resonance. The resonance effect, which is due to elasticity in the Voigt model (Macpherson, 1980; Maa and Mehta, 1990; Piedra-Cueva, 1993), increases the dissipation rate of surface waves with frequencies around the natural frequency of oscillation of the mud layer. The impact of resonance in viscoleastic mud is beyond wave dissipation and modulation. Ng and Zhang (2007) developed an analytical formulation for mass transport under progressive waves over a thin layer of viscoelastic mud and showed that resonance in the mud layer can substantially decrease or increase transport in the water layer compared to viscous mud, and may even change the direction of the drift.

Surface waves can lose energy over mud through direct and indirect pathways. In direct damping, surface wave energy that moves the mud layer is dissipated within the layer due to mud viscosity. However, field and laboratory experiments indicate that both high (Sheremet and Stone, 2003; Almashan and Dalrymple, 2015) and low (Elgar and Raubenheimer, 2008) surface wave harmonics exhibit higher damping than what is anticipated merely from direct coupling of waves with muddy seabed. Torres-Freyermuth and Hsu (2014) discuss that low-frequency wave dissipation dominated by nonlinear energy transfer occurs in low Ursell numbers. Ursell number

is defined as $U_r = \delta/\mu^2$, where $\delta = H_{rms}/2h$, $\mu = kh$, and H_{rms} is root mean square of wave, h is depth of water, and k is wave number. An additional pathway of indirect energy dissipation is the generation and damping of interfacial waves. The two-layer clear water/mud system supports the generation of interfacial waves a t water/mud interface (lutocline) which can grow to the point of breaking and cause mixing in the water column. Theoretical and laboratory studies show that a surface waves can trigger a pair of opposite-traveling oblique interfacial waves through subharmonic interactions (e.g. Hill and Foda, 1996; Jamali et al., 2003a; Tahvildari and Jamali, 2012). Tahvildari et al. (2016) studied this interaction among long waves and showed that accounting for damping in interfacial boundary layers is essential for adequate estimation of interfacial wave damping, which can affect surface damping rate through nonlinear energy transfer. These studies assume that the water/mud system behave as a two-layer inviscid or lightly viscous fluid. Hill and Foda (1999) examined the phenomenon in a system of clear water overlying viscoelastic medium and showed that viscoleasticity reduces interfacial wave growth rate.

Numerical wave models have enabled studying wave-mud interaction in complex wave conditions. Among rheological models of mud, the viscous model is most commonly used in numerical models due primarily to straightforward implementation. The Ng (2000) mechanism has been incorporated in operational phase-averaged models SAWN (Winterwerp et al., 2007; Kranenburg et al., 2011) and WAVEWATCH III (Rogers and Orzech, 2013) as well as frequency-domain phase-resolving models (e.g. Kaihatu et al., 2007; Kaihatu and Tahvildari, 2012; Safak et al., 2017). Simulations using phase-resolving models confirm that nonlinear interactions can cause energy transfer from high to low frequencies. Mud-induced wave dissipation mechanism has also been incorporated in phase-resolving time-domain models.

Torres-Freyermuth and Hsu (2010) developed a two-dimensional model based on Reynolds-averaged Navier-Stokes equations and used two-phase flow equations for fine sediment transport in turbulent flow. It was shown that second-order energy transfer across the spectrum causes stronger wave dissipation rate at lower and higher harmonics compared to principal harmonics. Mud was assumed to be a viscous fluid.

As noted by Chou et al. (1993), mud demonstrates complicated rheological behavior and idealizing it as a homogenous viscous fluid can result in inaccuracies in predicting wave propagation. For instance, Hsu et al. (2013) show that although viscous fluid assumption can describe mud behavior under energetic waves, the mud layer exhibits non-Newtonian behavior in low energy conditions. Jain and Mehta (2009) discuss that among various proxies assumed for mud behavior, viscoelastic medium assumption can predict wave attenuation over the widest range of wave action and sediment properties. Several previous studies have used viscoelastic models to mimic mud behavior. Macpherson (1980) studied surface wave attenuation in a two-layer system where the bottom layer is described by the viscoelastic Voigt model. It was shown that for a given mud viscosity, wave frequency, and water depth, increasing elasticity can decrease wave dissipation. Piedra-Cueva (1993) extended the work of Macpherson (1980) to include boundary layer effects at water/mud interface. More recently, Liu and Chan (2007) (hereafter referred to as LC) developed an analytical solution for wave damping over a thin viscoelastic layer. It was shown that the balance between mud viscosity and elasticity results in complexities in predicting wave dissipation rate. This model has recently been implemented in the phase-averaged model SWAN (Beyramzade and Siadatmousavi, 2017). However, in shallow waters, strong nonlinear triad interactions may result in inaccuracies in phase-averaged wave models and phase-resolving wave models can simulate wave propagation more reliably. The

combined effect of nonlinear wave-wave interactions and wave coupling with viscoelastic mud on evolution of surface wave spectrum has not yet been studied.

In the first part of this research (Chapter 2), we develop a new numerical wave-mud interaction model by coupling a mechanism for wave dissipation and modulation evolution by viscoelastic muds in a numerical wave model. The model results for dissipation of monochromatic surface waves is validated with laboratory experiments of Soltanpour and Samsami (2011) and Zhao et al. (2006). To the best of our knowledge, detailed measurements of surface wave spectrum over viscoelastic mud is not currently available, thus it is not possible to validate the model for its performance on spectral evolution. The coupled model is then used to examine nonlinear evolution of monochromatic and random surface waves. In addition to reliable wave prediction, a numerical wave model with a more versatile mud-induced wave dissipation/modulation mechanism enables a more comprehensive approach for inverse deduction of mud parameters from wave data. For instance, Tahvildari and Kaihatu (2011) use the Kaihatu et al. (2007) wave-mud interaction model, which includes a viscous mud damping mechanism, as the forward model in their inversion scheme. Such an inverse model becomes more versatile if a viscoelastic forward model is used instead.

Although wave-mud interaction has been the subject of many recent studies (Kaihatu et al., 2007; Tahvildari and Kaihatu, 2011; Liao et al., 2015; Safak et al., 2017; Tahvildari and Sharifineyestani, 2019), only a few studies consider the effect of currents on wave-mud interaction. However, substantial mud deposition occurs in river deltas and strong currents can interact with wave and mud in the vicinity of river inlets. Therefore, a model that incorporates current effects on waves can better predict mud-induced wave attenuation. Interaction between waves and currents change the linear and nonlinear properties of surface waves (Bretherton and

Garrett, 1968). Doppler shifting of frequencies is a linear effect of currents on waves that can result in nonlinear energy transfer across the wave spectrum (Kaihatu, 2009). Other nonlinear effects of currents have been previously studied focusing on large amplitude waves in the presence of adverse currents (Smith, 1976), waves near blocking condition (Crapper, 1972; Chawla and Kirby, 2002), and deep water waves (Turpin et al., 1983; Kirby, 1986)) and wave-wave iterations in shallow water for regular (Chen et al., 1999) and irregular (Kaihatu, 2009) waves.

In the second part of this research (Chapter 3), we extend the model developed in Chapter 2 to include the effect of currents and eliminates the limitation of thin-mud-layer assumption imposed by the Liu and Chan (2007) formulation. Therefore, the model proposed in Chapter 3 provides a more comprehensive predictive tool for wave propagation in coastal waters. For this purpose, we extend the model of Kaihatu and Tahvildari (2012) by generalizing the mud rheology to a viscoelastic solid. We utilize two models to represent mud-induced damping and modulation of surface wave in the wave model, namely Liu and Chan (2007) and Macpherson (1980), which enables applying the model to muds of arbitrary thickness.

In addition to muddy seafloors, hydrodynamic and wave energy in coastal areas could be affected by submerged aquatic vegetation (SAV). SAV is a critical habitat that can stabilize sediments, and attenuate storm surge and wave energy. While most previous studies on seagrasses have been focused on ecology of seagrasses, recent works suggest that SAV meadows can dissipate surface water waves (Nowacki et al., 2017). Biological properties of seagrasses such as shoot density (number of shoots per unit area), distribution, and length of shoots affect wave dissipation capacity of SAV. On the other hand, water depth and hydrodynamic variables, namely flow velocity and wave height, impact photosynthesis by affecting seagrass shoots orientation thus its

capacity to absorb light. Therefore, it is imperative to understand the two-way interactions between flow dynamics and seagrass biology. There has been a disconnect between models that simulate flow processes around vegetation and models that simulate seagrass photosynthesis that affect its capacity to modify flow. Therefore, representation of waves and flow in current SAV growth models (e.g. Zimmerman, 2003) are very limited. In chapter 4 we conducted an interdisciplinary study in which we focus on exploring the relationships between hydrodynamic and biophysical properties of seagrasses through field data analysis and computational studies.

This research is structured as follows. Following this introduction, Chapter 2 discusses the wave-current-mud interaction model, Chapter 3 presents the wave-current-mud interaction model. The model results for evolution of monochromatic and random surface waves, discussion and conclusions are outlined at the end of each chapter. Chapter 4 presents the relationships between hydrodynamic and biophysical properties of seagrasses using field data analysis and computational studies. Finally, the conclusion and recommendations for future research is provided in Chapter 5.

CHAPTER 2[1]

MODEL FOR WAVE PROPAGATION OVER VISCOELASTIC MUD

This wave-mud interaction model is comprised of a wave model based on the nonlinear spectral frequency-domain phase-resolving model of Kaihatu and Kirby (1995) and the mechanism for mud-induced wave dissipation and modulation is based on the LC model. For viscoelastic muds, these effects include wave attenuation and frequency modulation. The attenuation effect is represented by an added term to the equation that governs wave propagation, and frequency modulation is accounted for by correcting the wavenumbers computed by the wave model in the absence of mud.

2.1. Wave Model

The wave model of Kaihatu and Kirby (1995) is based on a nonlinear frequency-domain mild-slope formulation which solves the second-order nonlinear wave-wave interactions. The model uses parabolic approximation, thus is applicable to weakly two-dimensional waves (Radder, 1979), and assumes irrotational flow and mildly varying depth in the horizontal plane, h(x,y). We outline the essential components of the numerical model here and refer the interested reader to Kaihatu and Kirby (1995) for a comprehensive description of the wave model. In this model, the free surface, η, is expressed as,

$$\eta(x,t) = \sum_{n=1}^{N} \frac{A_n}{2} e^{i(\int k_n dx - \omega_n t)} + c.c., \qquad (1)$$

[1] This paper is based on the paper Tahvildari N, Sharifineyestani E. 2019. A numerical study on nonlinear surface wave evolution over viscoelastic mud. 154:103557. doi: https://doi.org/10.1016/j.coastaleng.

where A_n and ω_n are the amplitude and angular frequency of the nth harmonic, g is the gravitational acceleration, $i = \sqrt{-1}$, and $c.c.$ denotes the complex conjugate. Wavenumber k_n is associated with ω_n through the dispersion relation:

$$\omega_n^2 = g k_n \tanh(k_n h), \qquad (2)$$

where h is the depth of clear water above the muddy bed. The frequency-domain model for wave propagation over mildly varying depth in one horizontal dimension is given by Kaihatu and Kirby (1995):

$$A_{nx} + \frac{(CC_g)_{nx}}{(2CC_g)_n} A_n + D_n A_n \qquad (3)$$

$$= \frac{-i}{8(kCC_g)_n}\left(\sum_{l=1}^{n-1} R A_l A_{n-l} e^{i\Theta_{l,n-l}} + 2\sum_{l=1}^{N-n} S A_l^* A_{n+l} e^{i\Theta_{n+l,-l}}\right)$$

where C is phase velocity, C_g is the group velocity, and D_n is the dissipation rate. The subscript x refers to spatial gradient in x direction. The nonlinear interaction coefficients R and S govern the superharmonic and subharmonic interactions, respectively, and are given by,

$$R = \left(\frac{g}{\omega_l \omega_{n-l}}\right)[\omega_n^2 k_l k_{n-l} + (k_l + k_{n+l})(\omega_{n-l} k_l + \omega_l k_{n-l})] \qquad (4)$$

$$-\frac{\omega_n^2}{g}(\omega_l^2 - \omega_l \omega_{n-l} + \omega_{n-l}^2),$$

$$S = \left(\frac{g}{\omega_l \omega_{n+l}}\right)[\omega_n^2 k_l k_{n+l} + (k_{n+l} - k_l)(\omega_{n+l} k_l + \omega_l k_{n+l})] \qquad (5)$$

$$-\frac{\omega_n^2}{g}(\omega_l^2 - \omega_l \omega_{n+l} + \omega_{n+l}^2),$$

and the phase mismatches $\Theta_{l,n-l}$ and $\Theta_{n+l,-l}$ are given by:

$$\Theta_{l,n-l} = \int (k_l + k_{n-l} - k_n)dx, \qquad (6)$$

$$\Theta_{n+l,-l} = \int (k_{n+l} - k_l - k_n)dx. \qquad (7)$$

The energy dissipation in equation (3) is represented by the term $D_n A_n$ which can be due to wave breaking (e.g. Kirby and Kaihatu, 1997), wave-mud interaction (Kaihatu et al., 2007), wave-vegetation interaction (Kaihatu et al., 2018), or any other dissipative mechanism. It is noted that this approach does not account for turbulence-sediment interactions (e.g. Torres-Freyermuth and Hsu, 2010) or the feedbacks from the mud layer to surface forcing such as harmonic generation at water-mud interface (lutocline) (e.g. Tahvildari et al., 2016). However, the model is adequate for this study as the focus is to investigate the impact of mud viscoelasticity on surface wave evolution.

2.2. Model for Mud-Induced Surface Wave Evolution

In this section, we discuss the mechanism for wave dissipation and frequency modulation by viscoelastic muddy beds. The general approach is to compute wave dissipation rates and modulated frequencies by solving the complex dispersion relation of a two-layer system composed of a layer of clear water overlying a layer of mud. In general, the dispersion relation is a function of wave frequency, wavenumber, and thicknesses, densities and viscosities of the layers, and shear modulus of mud.

The wavenumber in dissipative systems is a complex number with the real part governing frequency modulation and the imaginary part resulting in wave dissipation (e.g. Macpherson, 1980). Finding the roots of the general dispersion relation in which no assumption is applied on the depth of the fluid layer involves a numerical search in the complex plane (e.g. Dalrymple and Liu, 1978; Piedra-Cueva, 1993), and since the roots are non-unique, obtaining the desired

solution can be challenging. Alternatively, the dispersion relation can be simplified by assuming that the mud layer is relatively thin (Ng, 2000; Liu and Chan, 2007), and derive an explicit solution to the dispersion relation which can be implemented in numerical wave models in a straightforward manner (e.g. Kaihatu et al., 2007; Beyramzade and Siadatmousavi, 2017).

In this study, we use the LC model for wave evolution over viscoelastic mud. Similar to the Ng (2000) model, the mud layer is assumed to be thin with respect to water depth and to be of the same order of magnitude as the mud boundary layer. The mud boundary layer is defined as:

$$\delta_{me} = \sqrt{\frac{2|\nu_{me}|}{\omega}} \qquad (8)$$

where ν_{me} is the effective kinematic viscosity of mud given by Macpherson (1980),

$$\nu_{me} = \nu_m + \frac{iG_m}{\omega\rho_m}, \qquad (9)$$

where ν_m, G_m, and ρ_m are mud viscosity, shear modulus, and density, respectively. This equation describes a Voigt solid. LC derived the dispersion relation for a two-layer system composed of inviscid water overlying a thin layer of viscoelastic mud and obtained and analytical solution for complex wavenumber. The dimensionless real part of the wavenumber, k_r, and the surface wave dissipation rate, D_m, are given by,

$$k_r h = k_1 h - \frac{(k_1 h)^2 \gamma\left(\frac{\delta_{me}}{h}\right)}{\sinh 2k_1 h + 2k_1 h}\left[2\lambda - \frac{\Omega_M \sinh 2\lambda\Omega_M + \Omega_P \sin(2\lambda\Omega_P)}{\cosh(2\lambda\Omega_M) + \cos(2\lambda\Omega_P)}\right] \qquad (10)$$

$$D_m = \frac{(k_1 h)^2 \gamma\left(\frac{\delta_{me}}{h}\right)}{\sinh 2k_1 h + 2k_1 h}\left[\frac{\Omega_P \sinh 2\lambda\Omega_M - \Omega_M \sin(2\lambda\Omega_P)}{\cosh(2\lambda\Omega_M) + \cos(2\lambda\Omega_P)}\right] \qquad (11)$$

where

$$\omega^2 = gk_1 \tanh k_1 h, \quad (12)$$

$$\lambda = \frac{d}{\delta_{me}} \quad (13)$$

$$\Omega_P = \cos\frac{\theta}{2} + \sin\frac{\theta}{2}, \quad (14)$$

$$\Omega_M = \cos\frac{\theta}{2} - \sin\frac{\theta}{2}, \quad (15)$$

$$\tan\theta = \frac{G_m}{\omega\rho_m\nu_m}, \quad (16)$$

$$\gamma = \frac{\rho_w}{\rho_m} \quad (17)$$

where k_1 is the surface wavenumber in the absence of mud, and h and d are the thicknesses of the water and mud layers, respectively. The damping rate, D_m, depends on wave frequency. Figure (1) shows the variation of analytical damping rate with surface wave frequency for various values of mud shear modulus. In this figure, $\zeta = \sqrt{\nu_m/\nu_w}$ = 100, where ν_w is the kinematic viscosity of water, $d = 0.20$ m, $h = 2.00$ m, $\rho_m = 1111$ kg/m ^{3}, and density of water, ρ_w, is 1000 kg/m ^{3}.

Wave damping over viscoelastic mud is considerably different from viscous mud (Figure (1)). In the case of purely viscous mud, the damping rate is smallest in the low and high end of the frequency range and varies relatively mildly in between. The variation of damping rate for viscoelastic muds is more pronounced around a certain frequency due to the resonance effect. Resonance occurs when the surface wave frequency approaches the natural frequency of oscillation in the mud layer and results in amplification of interfacial waves. As a result, a high shear stress is developed within the mud layer and the surface wave is dissipated at a high rate due to mud viscosity.

The maximum damping rate varies non-monotonically with shear modulus. As seen in Figure (1), for the parameters used here, the maximum damping rate increases with mud shear modulus over G = [50,300] Pa up to $G_m = 100$ Pa and decreases thereafter. On the other hand, the frequency at which the maximum damping rate occurs (f_m) increases monotonically with G in this range. However, the variation of damping rate with G is more complex in lower G values (Figure (2)). Figure (2a) shows that while increase in G is still associated with increase in maximum damping rate in this range of G, the trend in variation of f_m with G becomes non-monotonic such that f_m decreases up to a certain G and increases thereafter. This pattern is consistent at low G_s is consistent irrespective of mud viscosity. As seen in Figure (2b), the minimum f_m occurs at around 11, 4, and 1 Pa, for mud viscosity of $\nu_m = 0.0130, 0.0072$, and 0.0013 m ^{2}/s, respectively.

In addition to direct viscous damping, which is computed by analytical damping rates, the ultimate dissipation rate of frequencies depends on nonlinear energy transfer across the spectrum (Kaihatu et al., 2007). Therefore, it is essential to study wave evolution using a spectral model that resolves nonlinear wave-wave interactions. The approach taken in development of this model is similar to that in Kaihatu et al. (2007). The analytical solution for direct damping rates, which is computed from equation (11), is used in equation (4) which is then solved numerically for spatial evolution of harmonic amplitudes over a domain.

The wave and mud models have several underlying assumptions that need to be preserved for the coupled model to be valid. This is particularly important as the resonance phenomenon can induce relatively large interfacial oscillations and velocities within the mud and water layers. The wave model is based on weakly nonlinear fully dispersive mild slope equations, and the analytical LC model is derived from linear equations of motion. In this study,

the depth of the mud layer is assumed to be constant, and bottom slope is zero. Furthermore, we limit the study to one-dimensional wave propagation to focus on energy transfer across the spectrum and eliminate complications due to two-dimensional effects such as diffraction, hence the parabolic approximation made in the derivation of the wave model holds. Therefore, the limiting condition for the coupled model is based on the condition for validity of the LC model, i.e. the flow needs to be almost linear.

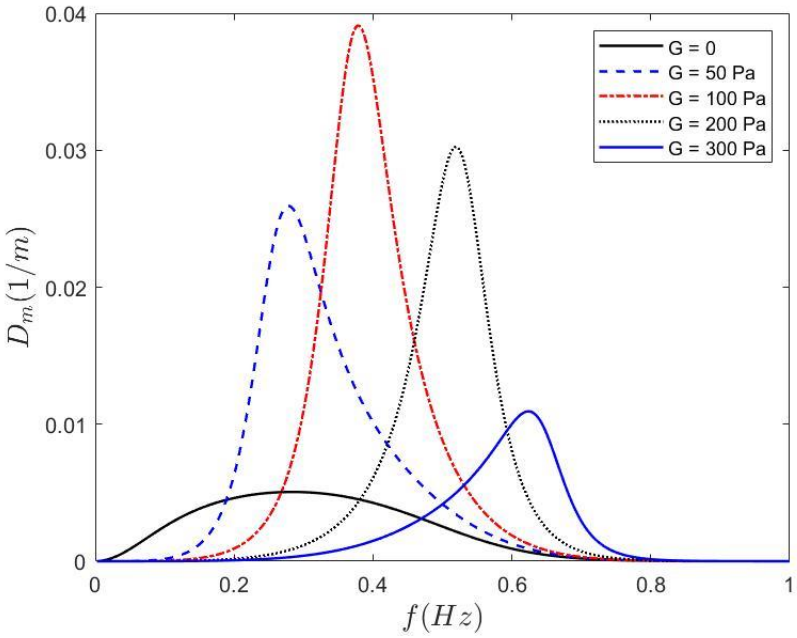

Figure 1. Variation of analytical damping rate of surface waves with frequency for different values of mud shear modulus. ($\zeta = 100, h = 2.00\ m, d_m = 0.20m, \rho_m = 1111\ kg\ /\ m^3$)

The horizontal momentum equation for flow in the mud layer is given by:

$$\frac{\partial u_m}{\partial t} + u_m \frac{\partial u_m}{\partial x} = -\frac{1}{\rho_m}\frac{\partial p_m}{\partial x} + \nu_{me}\left(\frac{\partial u_m^2}{\partial x^2} + \frac{\partial u_m^2}{\partial z^2}\right) \qquad (18)$$

where u_m is the velocity in the mud layer. Using the following dimensionless variables,

$$u_{*m} = \frac{u_m}{U}, \quad x_* = kx, \quad t_* = \omega t, \quad p_* = \frac{p}{\rho g h}, \quad z_* = \frac{z}{h}, \qquad (19)$$

where subscript asterisk shows dimensionless values and U is the characteristic velocity in the mud layer, the momentum equation becomes,

$$\frac{\partial u_{*m}}{\partial t_*} + \left(u_{*m}\frac{kU}{\omega}\right)\frac{\partial u_{*m}}{\partial x_*} = \left(-\frac{kgh}{U\omega}\right)\frac{\partial p_{*m}}{\partial x*} + \left(\frac{\nu_{me}U}{\omega}\right)\left(k^2\frac{\partial u_{*m}^2}{\partial x_*^2} + \frac{1}{h^2}\frac{\partial u_{*m}^2}{\partial z_*^2}\right). \qquad (20)$$

Therefore, the momentum equation can be linearized if $kU/\omega << 1$. This inequality can be examined using the expression for the velocity in mud layer. LC provides an equation for $\hat{u}_m$ which is the velocity amplitude after factoring out the temporal and spatial oscillatory term. Using this expression, we find that the largest value of ku_m/ω is 0.058 for the range of parameters used in this study, thus the coupling of the wave and mud-induced wave damping model is acceptable.

We note that theoretically, the thin-mud-layer assumption is valid if the mud layer thickness is small relative to wavelength, i.e. $kd \sim 1$, and $\mathcal{O}(d) \sim \mathcal{O}(\delta)$, where δ is the thickness of bottom boundary layer in mud. For the mud and water depths used to obtain the damping rates shown in Figure (1), $k_r\delta$ varies in [0.126, 0.32] and $k_r d$ varies in [0.037, 0.80] as surface wave frequencies vary in [0.1, 1.0] Hz. The thin-mud-layer assumption is valid for most of this frequency range. We note that while the mud layer may not seem to be relatively thin for high frequencies, e.g. $f = 1$ from the range of frequencies used here, the wave-mud interaction model may still perform satisfactorily. Kaihatu et al. (2007) shows that the wave-mud interaction model which has incorporated the viscous Ng (2000) model compares well with experiments even when the thin-mud-layer assumption is obviously violated. This observation may suggest that the portion of the mud layer that actively interacts with waves can still be considered thin even when the total thickness mud layer thickness is relatively large. The parameters used in Figure (1) are

the same as those used in Kaihatu and Tahvildari (2012), where waves over viscous mud underwent substantial dissipation.

2.3. Model Results

We demonstrate the results of the numerical model in this section. First, we validate the model with laboratory experiments and then utilize the model to show the effect of mud viscoelasticity on wave evolution. Monochromatic and random wave scenarios are simulated.

2.3.1. Model validation

As discussed earlier, mud can demonstrate different rheological behaviors under varying wave conditions. Additionally, mud properties such as density, viscosity, and layer thickness depend on hydrodynamic conditions. While these parameters may vary widely in the field, their values are measured only at a limited number of stations. In laboratory experiments, in contrast, the degree of uncertainty in parameter values and complexities in flow conditions are smaller and it is more realistic to assume spatially uniform quantities along and across a wave flume. Similarly, numerical wave models including the present model generally prescribe a certain mud rheology and assume constant mud characteristics over space and time. Therefore, it is more straightforward to obtain a quantitative comparison between numerical model results and laboratory data than field data. There are several experimental datasets on wave attenuation over mud (e.g. De Wit, 1996; Jiang and Mehta, 1996; Soltanpour and Samsami, 2011; Zhao et al., 2006). Here we validate the wave-mud interaction model with experiments of Soltanpour and Samsami (2011) and Zhao et al. (2006). Soltanpour and Samsami (2011) conducted a series of rheological tests and laboratory experiments on wave dissipation using natural and commercial muds. Using the tests which were carried out in oscillatory mode, they provided mud viscosity

and shear modulus as a function of water content and wave period. Here we use wave dissipation measurements over kaolinite with water content ratio of 99.3 %. Based on the empirical relationships provided in Soltanpour and Samsami (2011), mud kinematic viscosity and shear modulus are 0.038 m^2/s and 1852 Pa, respectively. The initial wave height, prior to propagating over the mud patch varies from 2.40 cm to 9.00 cm in different experiment runs. Figure (3a) shows that the attenuated wave height in the lee of a mud patch as computed from the numerical model (H_{mod}) compared well with measurements (H_{meas}) for both viscous and viscoelastic mud scenarios. However, the model with the viscoelastic mud-induced wave evolution shows and advantage over the model with viscous mud-induced wave dissipation. The Root Mean Square Error (RMSE) for simulated wave heights using viscoelastic and viscous mud models are 0.252 cm ($R^2 = 0.955$) and 0.535 cm ($R^2 = 0.845$), respectively.

For further validation, we use the laboratory results of Zhao et al. (2006). They conducted several tests in a wave flume and measured wave attenuation over mud in the absence and presence of currents. Among their experiments, only six were carried out using pure oscillatory flow and the rest included currents and waves simultaneously. In these six experiments, which are used here for model validation, the range of parameters are $h = 24 - 28$ cm, $d_m = 6 - 12$ cm, $\rho_m = 1190 - 1350$ kg/m ^{3}, and $G = 0.4 - 25$ Pa. Waves are monochromatic and mud shear modulus is estimated using a field-based empirical function obtained by Zhao et al. (2006). To compare model results with these experiments, we calculate the numerical spatial attenuation rates of wave height as,

$$H(x) = H_0 e^{-D_s x}, \qquad (21)$$

where H_0 is the incident wave height, $H(x)$ is wave height over mud, and D_s is the spatial damping rate of wave height. The equation assumes exponential attenuation of incident wave

height and is the same as that used by Zhao et al. (2006). Figure (3b) shows how the damping rate from the model compares with the data. Model runs with viscous mud mechanism are also included to assess improvement achieved through including mud's elastic effects. The RSME for the model with viscoelastic and viscous mud is 0.000759 m $^{-1}$ (R^2 = 0.998) and 0.00172 m $^{-1}$ (R^2 = 0.99), respectively.

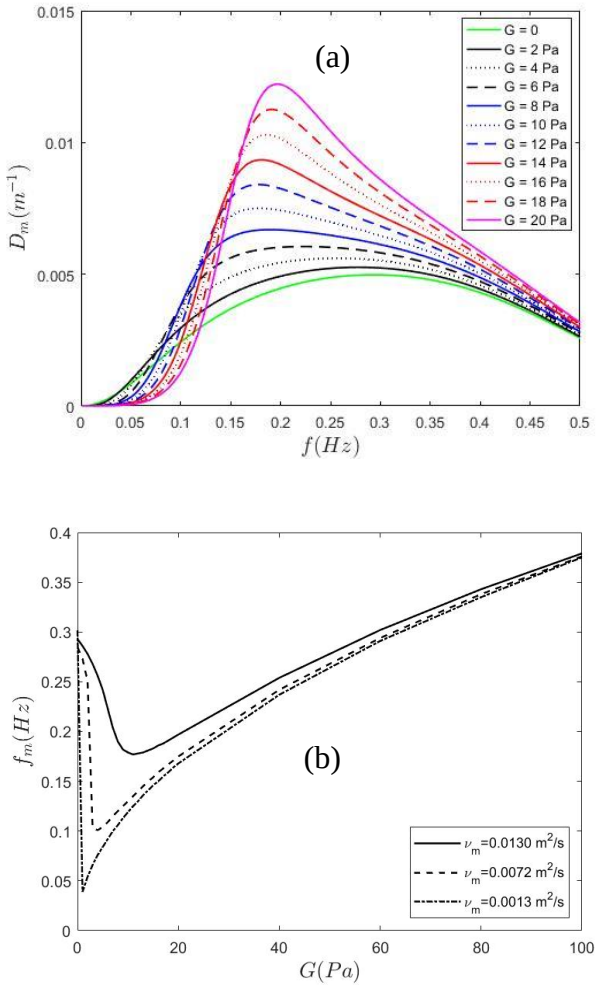

Figure 2. (a) Variation of analytical surface wave damping rate with frequency for small values of mud shear modulus, (b) variation of the frequency associated with peak damping with different mud shear moduli and three values of mud viscosity. ($\zeta = 100, \mathrm{h} = 2.00\ \mathrm{m}, \mathrm{d_m} = 0.20\mathrm{m}, \rho_\mathrm{m} = 1111\ \mathrm{kg}/\mathrm{m}^3$)

Therefore, both experimental sets confirm that the wave-mud interaction model that accounts for mud's elasticity can perform better compared to the wave-mud model with viscous mud mechanism.

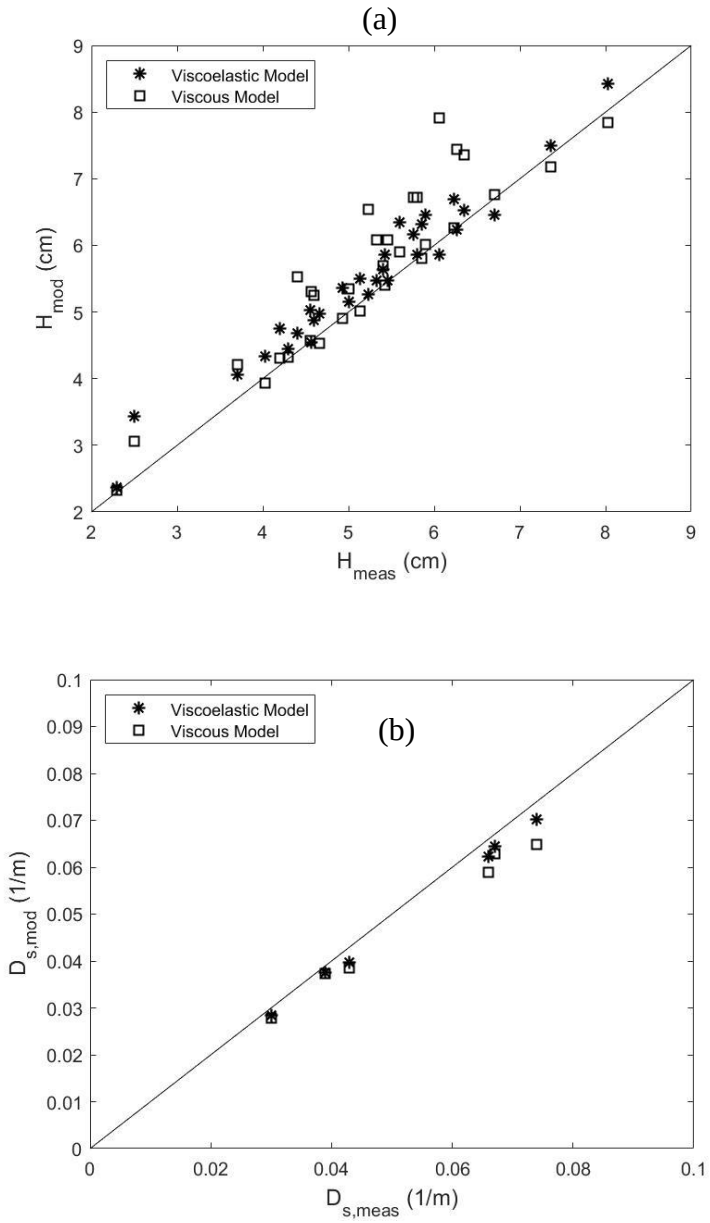

Figure 3. Comparison between model results and laboratory experiments: (a) Simulated attenuated wave heights (H_{mod}) is compared with experiments of Soltanpour and Samsami (2011) (H_{meas}), (b) Simulated wave attenuation rates ($D_{s,meas}$) is compared with experiments of Zhao et al. (2006) ($D_{s,meas}$).

2.3.2. Permanent form waves

The model is used to study the effect of viscoelasticity on surface wave evolution. To minimize complexities of wave characteristics, we first simulate the propagation of monochromatic waves over mud, which are described by cnoidal waves in the model. Cnoidal or permanent form waves are nonlinear canonical solutions of the Korteweg-deVries (KdV) equation in which various harmonics travel at the same speed. In this set of simulations, we use the permanent form solution developed by Kaihatu et al. (2007) for equation (3). Since the current model is in frequency domain, a cnoidal wave is generated by superposing the component amplitudes that are harmonics of a base frequency.

The simulations are conducted in a domain of length 1000 m with grid resolution $\Delta x = 0.025$ m. A total of 10 harmonics are used to generate a cnoidal wave with the base frequency of $f = 0.10$ Hz, and the mud patch is placed between $x = 300$ m and $x = 800$ m. The waveheight is $H = 0.10$ m, and the depth of water and mud layer are 1.00 m and 0.20 m, respectively. Figure (4) shows the combined effect of viscosity and elasticity on cnoidal waves for two values of mud viscosity, $\nu_m = 1.30 \times 10^{-2}$ m^2/s and 1.30×10^{-4}m^2/s, and three values of shear modulus $G = 0$,50 and 100 Pa. In the case with lightly viscous mud ($\zeta = 10$), increase in shear modulus reduces the overall wave dissipation such that the spectrum does not exhibit noticeable energy loss over mud with $G = 100$ Pa (Figure 4a). The maximum dissipation occurs over purely viscous mud ($G = 0$) and the difference between waveheights over muds with shear moduli $G = 50$ and 100 Pa is negligible. As seen in Figure (4b), an increase in mud viscosity not only increases attenuation of wave amplitudes, as expected, but also makes the difference between wave amplitudes over muds with $G = 50$ Pa and 100 Pa more pronounced, such that the wave over $G = 100$ Pa is clearly less damped.

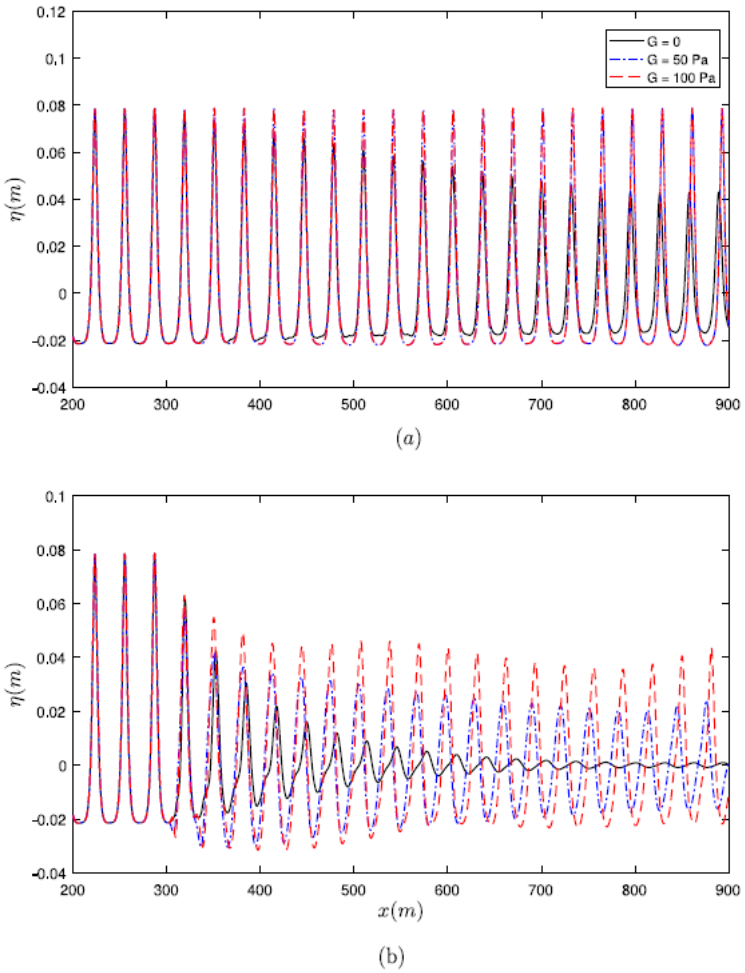

Figure 4. Evolution of cnoidal waves over viscoelastic mud with shear moduli of G = 0, 50, and 100 Pa, and viscosity of (a) $\vartheta_m = 1.30 \times 10^{-4}\ {}^{m^2}/_{s}$ and (b) $\vartheta_m = 1.30 \times 10^{-2}\ {}^{m^2}/_{s}$

In addition to impact on wave height attenuation rates, mud's elasticity results in frequency modulation which can manifest itself through modification in shape and phase of surface waves. Comparison between Figures (4a) and (4b) shows that increase in viscosity results in increase in phase difference between surface wave amplitudes (η). Furthermore, η over viscoelastic muds show a phase lag relative to η over viscous mud. It is noteworthy that this phase lag is larger over mud with $G = 50$ Pa. This variability in phase shift occurs over viscoelastic mud regardless of ν and G values. In Figure (5a), we examine phase variation of surface waves amplitude over muds with $\zeta = 10$, $d_m = 0.02$ m, $h = 1$ m, and five values of

shear modulus in low-G range, namely $G = 0,1,3,5$, and 25 Pa. Phase variation for higher G values for this parameters set was found to be negligible. We choose a low value for mud viscosity to isolate the effect of elasticity on phase shift. As seen, the phase difference between a wave over mud with $G = 1$ and viscous mud is negative while waves over muds with larger Gs shows a positive phase shift relative to the wave over mud with $G = 1$ Pa. The phase of η depends on k_r and wave frequency which is a function of k_r through the dispersion relation. Thus, we can examine variation of k_r with G to explore variations in wave phase. LC show how dimensionless k_r changes with dimensionless G ($G *= G/(\rho_m g h)$) for cases in which $d/h = 0.072$, $\rho_m/\rho_w = 0.50$, and $\omega *= \omega/(\rho_m g h) = 0.50$ (their Figure (12)). They show that over $G *= [10^{-5}, 10^{-2}]$, k_r gradually decreases to reach a minimum, then suddenly increases to reach a maximum, and decreases thereafter. We illustrate $k_r - G$ variation for the parameters used in Figure (5a) in Figure (5b) for f = 0.50 Hz as an example. Other frequencies in the spectrum follow a qualitatively similar pattern with different k_r values and the G at which the sudden jump in k_r occurs. This non-monotonic variation of k_r with G in the low-G range is a driver of the non-monotonic variation in phase shift. However, it should be noted that there are additional processes at play that complicate the connection between theoretical wave number of individual harmonics and the phase of η. As discussed earlier and shown in Figure (2b), there is another critical shear modulus before which f_m decreases and increases thereafter. Furthermore, each curve in Figure (5a) is a superposition of 15 coupled harmonics, thus nonlinear interactions between harmonics in the presence of mud can play a role in the phase of the cnoidal wave.

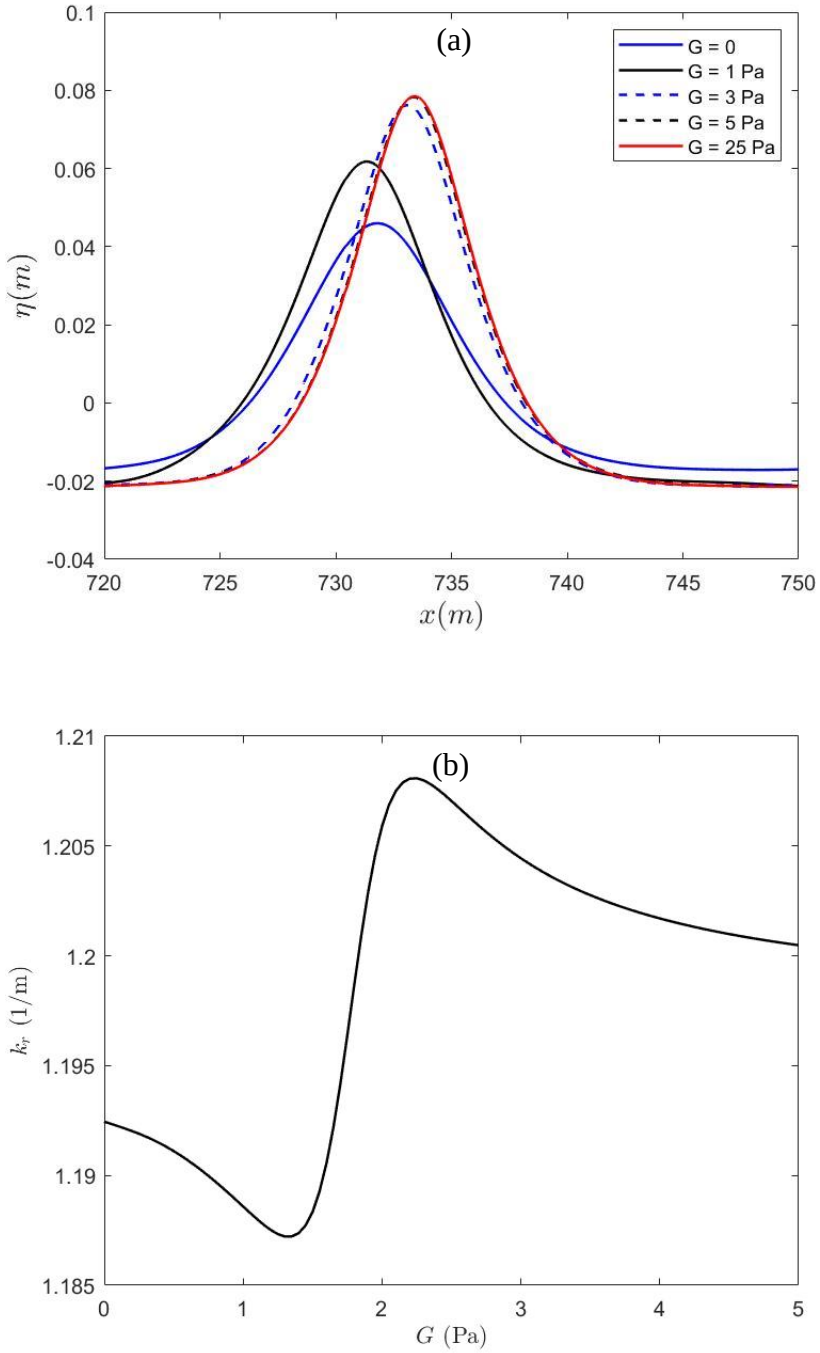

Figure 5. (a) Cnoidal waves over viscoelastic mud with shear moduli of $G = 0 - 25$ Pa, (b) variation of real component of surface wave number of frequency $f = 0.50\ Hz$ with mud shear modulus, $\zeta = 10, d_m = 0.02$, and $h = 1.00$ m.

Since the present model is phase-resolving, it enables investigating the combined effect of mud-induced dissipation and nonlinear wave-wave interactions on amplitude and phase of

frequency components in addition to bulk spectral characteristics. In the spectrum used here, the frequency range is [0.10, 1.00] Hz corresponding to $0.20 \leq kh \leq 4.03$. Figure (6a) shows the variation of amplitude spectrum of cnoidal waves for a case with $\zeta = 100$ and four values of shear modulus $G = 0{,}50{,}100,$ and 200 Pa. The figure shows the initial spectrum at $x = 0$ and the spectrum at the end of the mud patch at $x = 800$ m. As seen, regardless of the magnitude of shear modulus, high frequencies that are not long enough to interact with the bottom still undergo considerable damping. The damping of theses frequencies was also seen in the numerical simulation waves over viscous mud (Kaihatu et al., 2007; Safak et al., 2017).

The evolution of wave spectrum over viscoelastic mud can be analyzed by examining the dependency of analytical damping rates on frequency, which is strongly affected by resonance in the mud layer, and nonlinear energy transfer across the spectrum. Figure (6b) shows the variation of the analytical damping rate as a function of frequency over [0,1.00] Hz, for the same parameter values used in Figure (6a). The damping rates over muds with G = 50, 100, 200 Pa are smaller than those over purely viscous mud up to frequencies 0.19 Hz, 0.27 Hz, and 0.38 Hz, respectively, and surpass them beyond these frequencies. However, as seen in Figure (6a), frequency amplitudes are consistently larger over viscoelastic muds compared to viscous mud in low-frequency range. At higher frequencies, wave spectra over muds with $G = 50{,}100{,}200$ Pa intersect with the wave spectrum over viscous mud at 0.68 Hz, 0.80 Hz, and 0.95 Hz, respectively, which differ from the intersections between curves of analytical damping rates. As the analytical damping rates are obtained from linearized equations of motion, it can be inferred that this difference is due to nonlinear wave-wave interactions. To identify the source of this discrepancy more precisely, we run the model with subharmonic interactions deactivated (S = 0 in Equation 3).

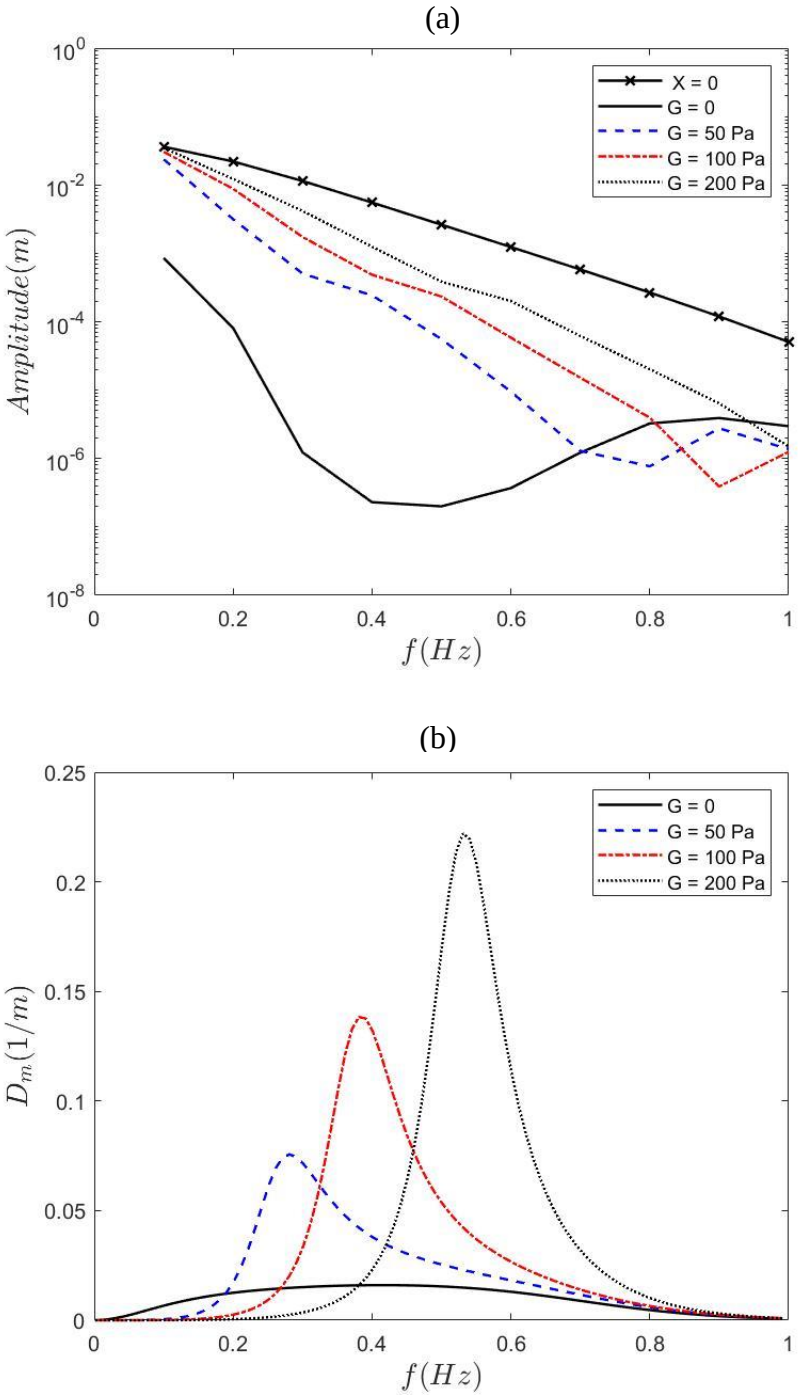

Figure 6. (a) Evolution of frequency amplitudes in a cnoidal wave spectrum over muds with difference shear moduli. The initial spectrum at x = 0 and the spectra at the end of mud patch (x = 800 m) are shown, (b) variation of analytical damping rate against frequency, $\vartheta_m = 1.30 \times 10^{-2}\ {}^{m^2}/_{s}$, $d_m = 0.02$, $h = 1.00$ m, and G =0, 50, 100, and 200 Pa.

The results, shown in Figure (7), indicate that the variation of frequency amplitudes can be described by the pattern of damping rate in low-frequency end of the spectra. As seen, the frequency amplitudes over viscoelastic muds with $G = 50, 100, 200$ Pa fall below the amplitudes over viscous mud at 0.145 Hz, 0.25 Hz, and 0.36 Hz, respectively, which are close to the frequencies at which the analytical damping rates of viscoelastic and viscous muds equate. Furthermore, the minimum frequency amplitude occur at 0.30 Hz (for G = 50, 100 Pa) and 0.40 Hz (for G = 200 Pa) which are close to frequencies that experience maximum damping rates. Note that the frequency increment in our numerical simulations is 0.1 Hz. On the high-frequency end of the spectrum, the change in frequency amplitudes with respect to incident wave spectrum is small. This is in agreement with the findings of Kaihatu et al.(2007) for viscous mud and suggests that damping of higher frequencies are due to subharmonic interactions regardless of the magnitude of mud shear modulus. Therefore, subharmonic interactions are the primary process that change the pattern of damping in high and low frequencies. The small difference between frequencies at which $Amplitude - f$ and $D_m - f$ curves intersect in the absence of subharmonic interactions can be attributed to superharmonic interactions.

At the extremely small viscosity values, mud acts as a purely elastic solid and its effect on surface wave is confined to frequency modulation. Figure (8) illustrates the evolution of a cnoidal eave spectrum over elastic muds with $G = 50{,}100$ Pa. Effect of subharmonic interactions is evident as low frequencies slightly gain energy at the expense of higher frequencies' loss of amplitude. The total damping rate over the spectrum is zero as expected.

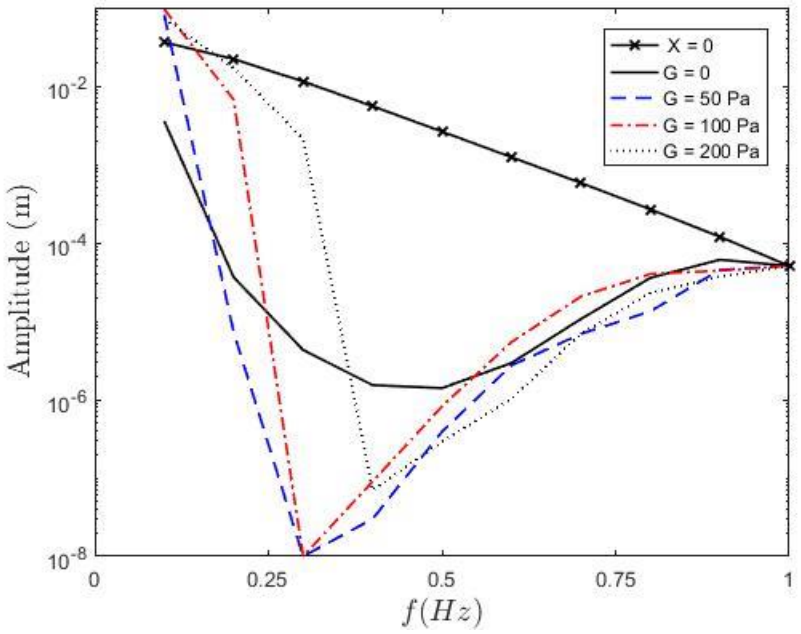

Figure 7. Evolution of the cnoidal wave spectrum over viscoelastic and viscous muds with subharmonic interactions deactivated. Wave and mud parameters and water depth are the same as those in Figure (6).

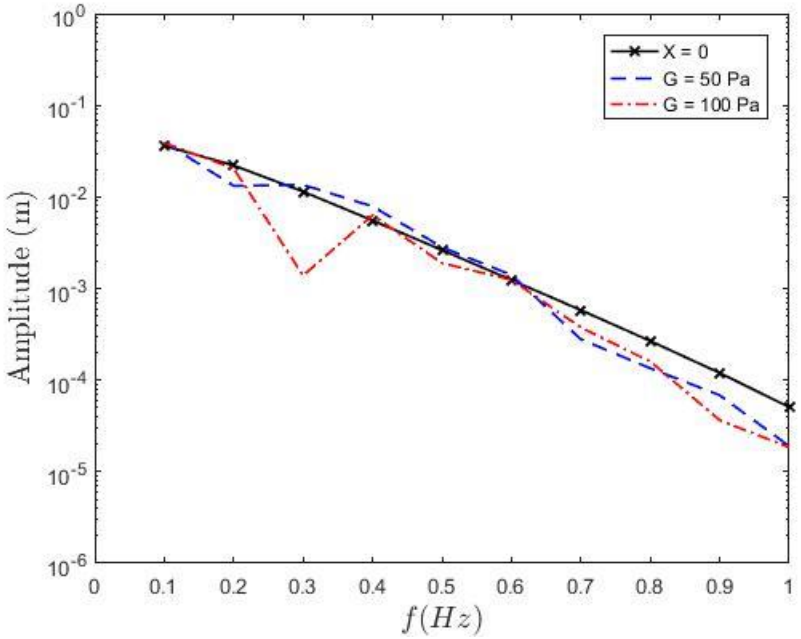

Figure 8. Evolution of frequency amplitudes in a cnoidal wave spectrum over elastic mud with different shear moduli. The initial spectra at x = 0 and the spectra at the end of mud patch (x = 800 m) are shown, $d_m = 0.20$, $h =$ 1.00 m, and G = 50, 100, and 200 Pa.

2.3.3. Random waves

In this section, we investigate the effect of mud viscoelasticity on evolution of random waves. We set up the model for a case that yields relatively high dissipation rates (ζ = 100 and d = 0.20 m) and use different values of shear modulus. The wave spectrum used here has the TMA form (Bouws et al., 1985). We study spectral evolution over mud by investigating the variation of root-mean-square waveheight (H_{rms}), as a bulk measure of wave characteristics, and examine alterations in spectral energy density over muds with different shear moduli. The H_{rms} of the initial spectrum is 0.34 m and two peak frequencies f_p = 0.06 and 0.40 Hz are chosen, resulting in Ursell numbers $U_r = 2.92$ and 0.04, where

$$U_r = \delta/\mu^2, \quad (22)$$

where $\delta = H_{rms}/2h$, and $\mu = kh$. We increase the length of domain to 4900 m for random wave simulations which corresponds to ~ 70 wavelength of the spectral peak for f_p = 0.06 Hz. As noted by Kaihatu and Tahvildari (2012), the spectrum reaches an equilibrium over this length and does not exhibit significant evolution beyond this point in the absence of mud. The mud patch is placed at $x = 1000 - 1500$ m.

As discussed earlier, linear wave theory for a two-layer water/Voigt solid system shows that resonance in the bottom layer results in significant dissipation of certain frequencies over the free surface. To highlight the impact of resonance in viscoelastic mud on random waves, we investigate the evolution of two spectra with peak frequencies $f_p = 0.06$ and 0.40 Hz. The mud and water layer specifications are $G = 100$ Pa, $d = 0.20$ m, $\zeta = 100$, and $h = 2.00$ m, resulting in the resonance frequency of $f_r = 0.40$ Hz. Figure (9a) compares the evolution of a spectrum with peak frequency $f_p = 0.06$ Hz over a viscous mud and a viscoelastic mud with $G = 100$ Pa.

The initial spectrum and the spectrum at the end of the mud patch are shown. As seen, all the frequencies in the spectrum experience a higher rate of dissipation over viscous mud, and the resonance frequency does not affect the spectrum since it is outside the frequency range. Evolution of a random wave spectrum with a peak frequency, $f_p = 0.40$ Hz, is shown in Figure (9b). In contrast to the case with $f_p = 0.06$ Hz, low frequencies undergo weaker dissipation over the viscoelastic mud compared to the viscous mud. However, the dissipation around the spectral peak, which corresponds to the resonance frequency, is significantly larger in the viscoelasic mud compared to the viscous one. The frequencies in the tail of the spectrum do not experience significant change over neither viscous nor viscoelastic mud. It is noteworthy that the spectral energy density, $S(f)$, over viscoelastic mud drops below that of viscous mud at $f = 0.27$ Hz which is equal to the frequency at which the damping rate over viscoelastic mud with $G = 100$ Pa becomes larger than that for the viscus mud (see Figure (1)). The spectra over viscous and viscoelastic muds converge at the end of the mud patch at $f \sim 0.60$ Hz which is consistent with the frequency at which the analytical damping rates for muds of different shear moduli become nearly equal. Therefore, direct damping by bed appears to be the dominant factor in overall pattern of damping across the spectrum.

Engineering designs are most commonly based on first-order bulk statistical measures of waves such as root-mean-square wave height (H_{rms}). Here we examine the effect of mud shear modulus on H_{rms} computed by the model. Figure (10) shows the spatial variation of H_{rms} with shear modulus for a wave spectra with peak frequencies 0.06 Hz and 0.40 Hz. The pattern of reduction in H_{rms} as a function of mud shear modulus follows the pattern of change in direct mud-induced wave damping (Figure (1)).

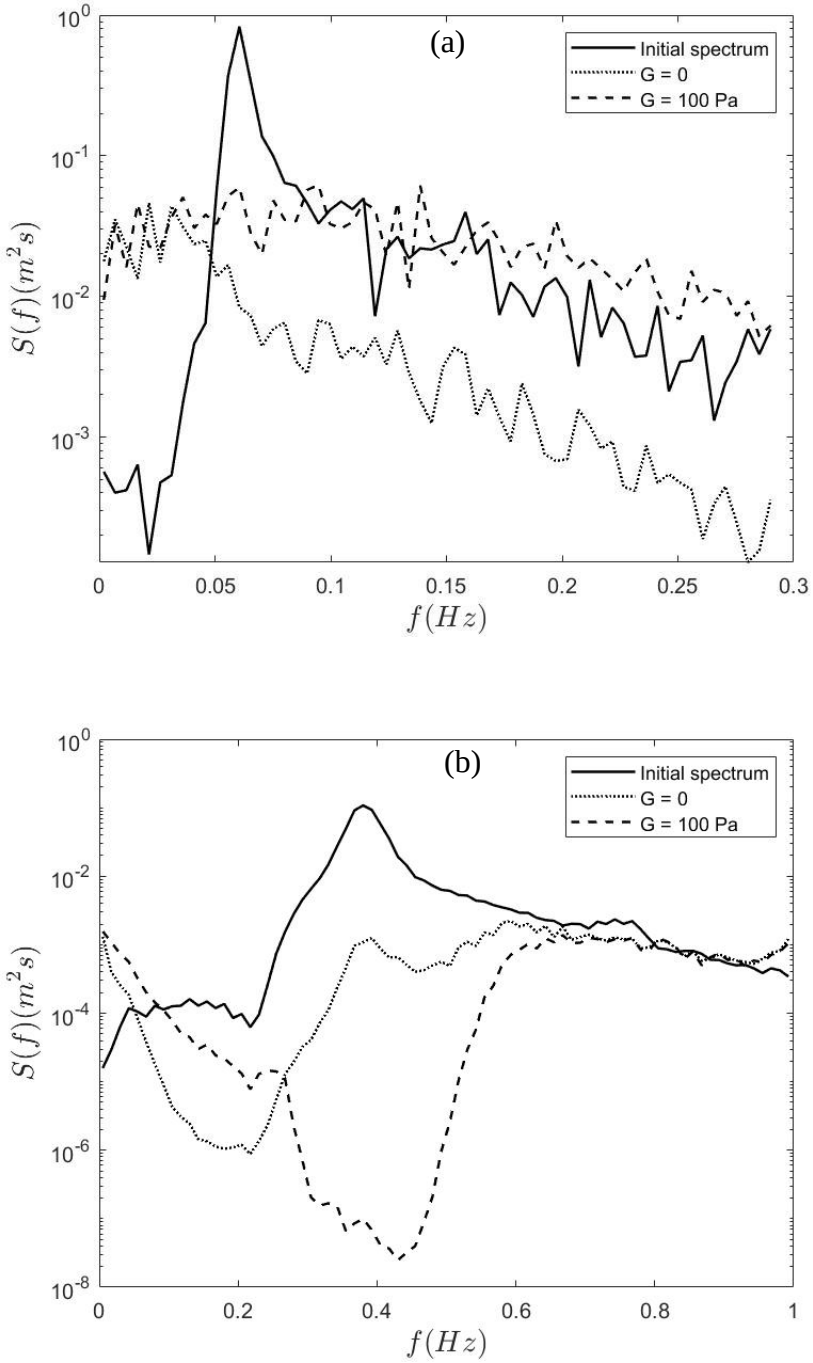

Figure 9. Spectral evolution of a random wave over muds with shear modulus of G = 0, and 100 Pa, ζ = 100, d_m = 0.20 m, and h = 2.00 m. The resonance frequency is f_r = 0.40 Hz and the peak frequencies are (a) f_p = 0.06 Hz and (b) f_p = 0.40 Hz. Solid line shows the initial spectrum and the dotted and dashed lines show the spectra at the end of the mud patch (x = 1500 m).

As seen in Figure (1) which has the same water depth and mud properties as in these random wave simulations, the damping rate is maximum for purely viscous mud and

monotonically decreases with increase in G in low frequencies. This pattern results in monotonic increase in H_{rms} damping with increase in G for the spectrum with the peak frequency of $f_p =$ 0.06 Hz (Figure (10a)). Direct damping also dictates the pattern of variation of H_{rms} with G for the spectrum with peak frequency at 0.40 Hz, in which H_{rms} initially decreases with increase in G up to $G = 100$ Pa and increases thereafter (Figure (10b)).

In order to examine the practical importance of mud viscoelasticity in realistic conditions, we study the attenuation of H_{rms} using the field parameters presented in Liao et al. (2015) where the effect of wave directionality on mud-induced wave dissipation was investigated in the central Chenier plain coast, Western Louisiana Shelf, USA. In the study, the range of parameters are $h = 2.89 - 4.16$ m, $d_m = 0.03 - 0.12$ m, $\nu_m = 0.079 - 3.17 \times 10^{-3}$ m^2/s, and $\rho_m = 1095 - 1206$ kg/m^3. We selected a parameter set as model input that is within this range to assess mud impacts on dissipation of random waves, namely $h = 2.89$ m, $d_m = 0.12$ m, $\nu_m = 2.5 \times 10^{-3}$ m^2/s, and $\rho_m = 1200$ kg/m^3. We vary G values from 0 to 100 Pa following LC and use an initial TMA spectrum in the model based on the spectral peak amplitude and period measured in the field. As seen in Figure (11), the attenuation rate of H_{rms} is largest over viscous mud (exceeding 50%) and decreases with increase in shear modulus to the point that no attenuation is seen over a mud with $G = 100$ Pa. Therefore, over this realistic set of values, disregarding mud elasticity can result in more than 50% error in H_{rms} prediction.

We now investigate the spatial evolution of surface wave spectrum in more details to highlight how mud elasticity affects nonlinear energy transfer among frequencies. Figure (12) shows the evolution of spectral energy density in the spectrum with f_p = 0.06 Hz over mud with G = 0, 50 and 100 Pa. Prior to the mud patch, transfer of energy to higher harmonics $2f_p$ and $3f_p$ occurs through superharmonic interactions.

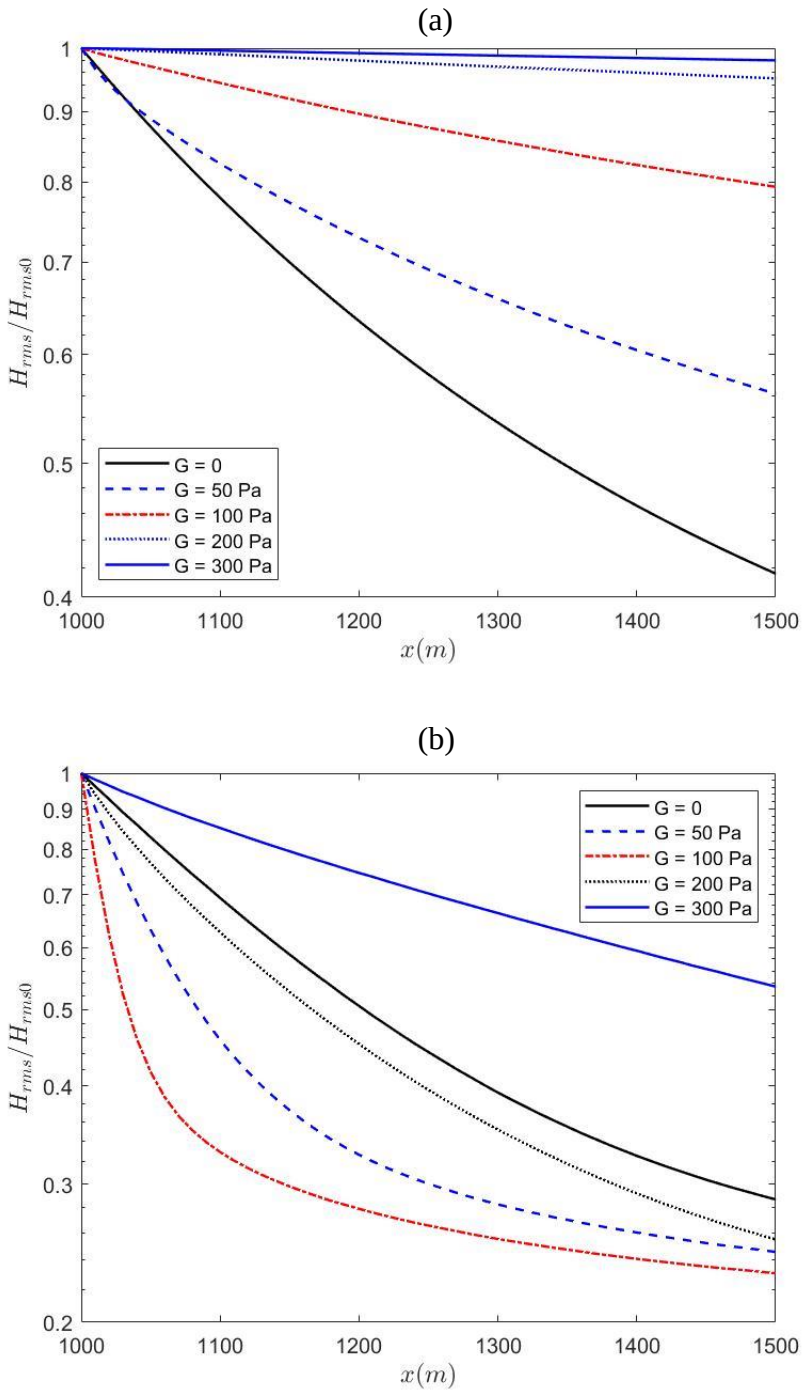

Figure 10. Spatial variation of random wave H_{rms} over viscoelastic muds with shear moduli of $G = 0 - 300$ Pa. The mud patch is located at $x = 1000 - 1500\ m$, $\zeta = 100$, $d_m = 0.20m$, $h = 2.00\ m$, and the peak frequency of initial spectrum is (a) 0.06 Hz and (b) 0.40 Hz. H_{rms0} is H_{rms} at $x = 1000$ m.

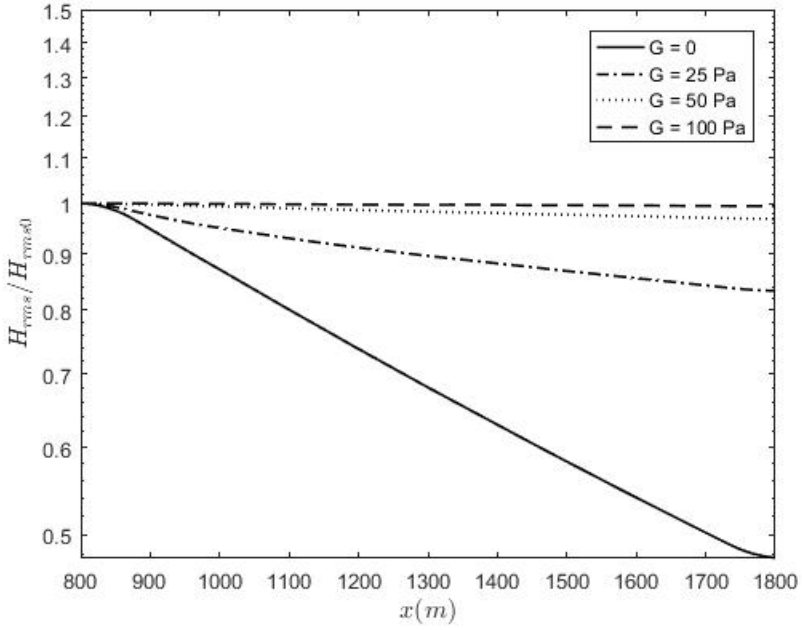

Figure 11. Spatial variation of random wave H_{rms} over viscoelastic muds with shear moduli of $G = 0 - 100$ Pa. The mud patch is located at x = 1000-1500 m, $d_m = 0.12m$, $h = 2.89\ m$, $\vartheta_m = 2.5 \times 10^{-3}$ and $\rho_m = 1200\ kg/m^3$. H_{rms0} is H_{rms} at $x = 1000$ m.

These harmonics propagate beyond the mud patch only over viscoelastic muds which induce lower damping rates than viscous mud. As seen, the spectral energy density in higher frequencies is largest over the mud with $G = 100$ Pa, while strong damping across the spectrum over viscous mud suppresses the generated harmonics. Figure (13) shows further details of the spectral evolution at 100 m increments over muds with $G = 0$ and 100 Pa. Over the distance from $x = 0$ up to the mud patch at $x = 1000$ m, nonlinear interactions act to transfer energy from the spectral peak to higher and lower frequencies to achieve a nearly uniform energy distribution across the spectrum. Higher spectral energy density ($S(f)$) at superharmonics $2f_p$ and $3f_p$ compared to neighbouring frequencies is evident. Over viscous mud, spectral energy density levels at the range $f > f_p$ drop below those in the initial spectrum at around $x = 1400$ m. In contrast, $S(f)$ values in this range of frequencies remain higher than those in the initial

spectrum over the viscoelastic mud. As seen in Figure (12c), the spectral peak is shifted towards higher frequencies over viscoelastic mud at $x = 1500$ m. Over both viscous and viscoelastic muds, damping is pronounced when $f_p < f$ range while if $f < f_p$, energy dissipation is not significant regardless of the magnitude of mud shear modulus.

Expectedly, resonance in viscoelastic mud strongly affects spectral evolution if the surface wave energy is concentrated around the resonance frequency. Figure (14) shows the spatial variation in spectral energy density over muds with shear moduli G = 0, 50, and 100 Pa for a spectrum with f_p = 0.40 Hz, and Figure (15) shows the spectra at the same stations as in Figure (13). The spectral evolution differs from the case with $f_p = 0.06$ Hz in several ways. First, the damping of the peak frequency is high over viscoelastic mud and is the highest over the mud with $G = 100$ Pa which has the resonance frequency of 0.40 Hz. This intense damping is evident from the beginning of the mud patch (Figure (15b)). On the other hand, the spectrum over viscous mud exhibits the lowest rate of dissipation such that peak frequency continues to have the highest energy density up to around x = 1400 m. Second, the energy level at the tail of the spectra suggests that the elasticity of the mud layer does not alter frequencies in this range significantly (Figure (15b-f)). Third, lower frequencies undergo weaker damping over viscoelastic mud, as evident in the spectra at x = 1200 m station and forward.

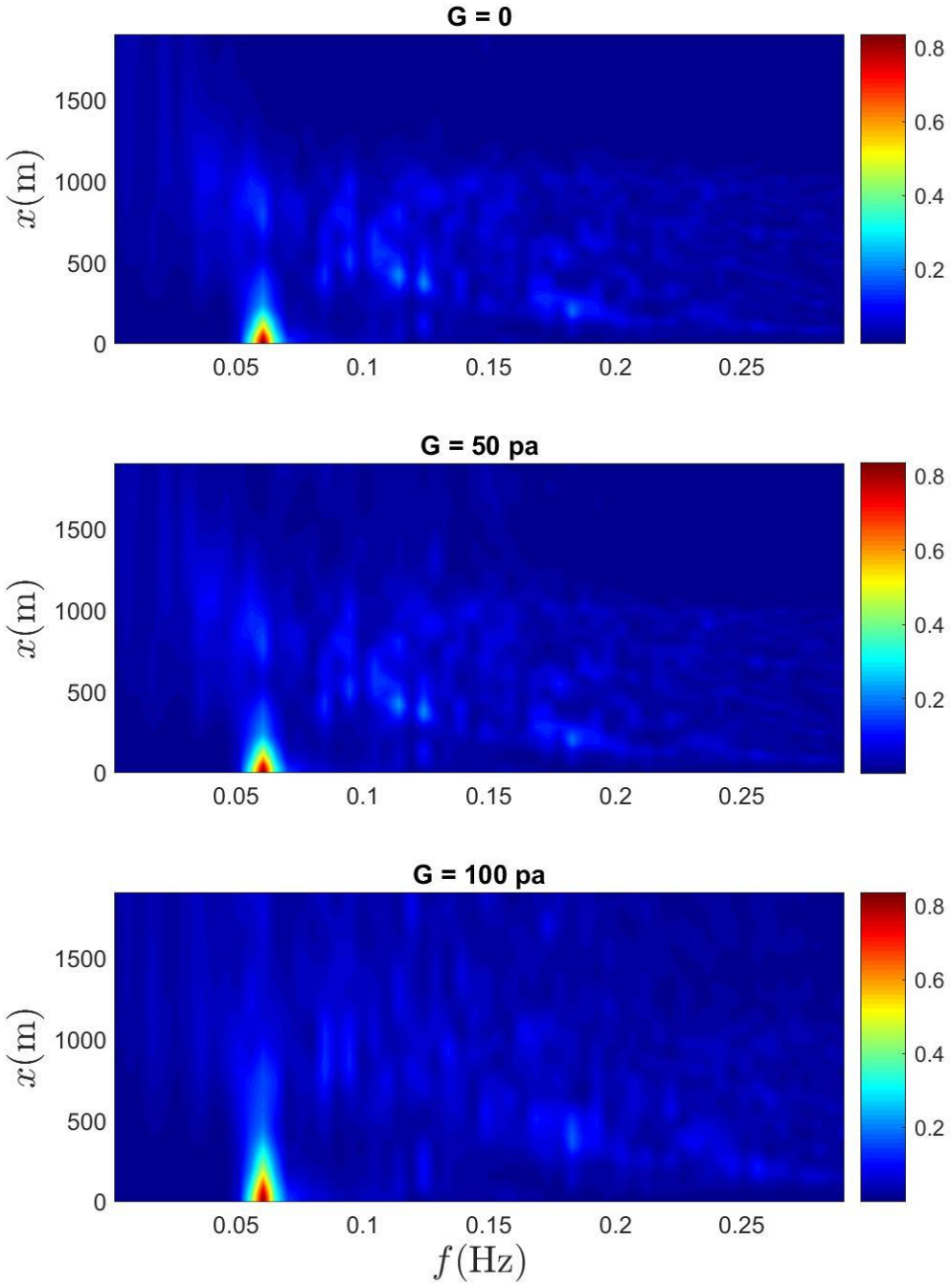

Figure 12. Spatial evolution of spectral energy density over muds with shear moduli of G = 0, 50 and 100 Pa. f_p = 0.06 Hz, $\zeta = 100, h = 2.00\,m, d_m = 0.20m$.

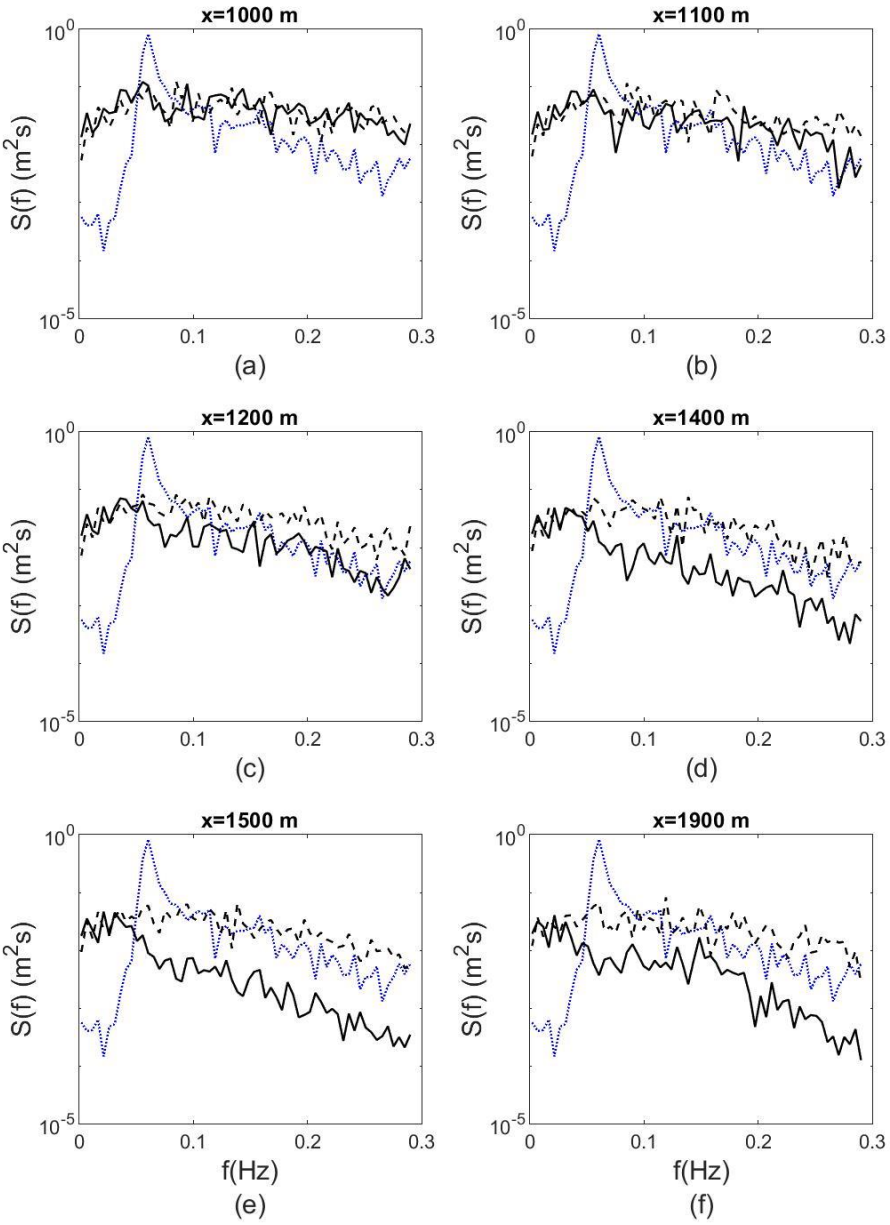

Figure 13. Surface wave spectrum over viscous (solid line) and viscoelastic (dashed line) mud with shear modulus of $G = 100$ (dashed line), at several locations. The initial spectrum is shown by a dotted line, $f_p = 0.06\,Hz,\ \zeta = 100, h = 2.00\,m, d_m = 0.20m$.

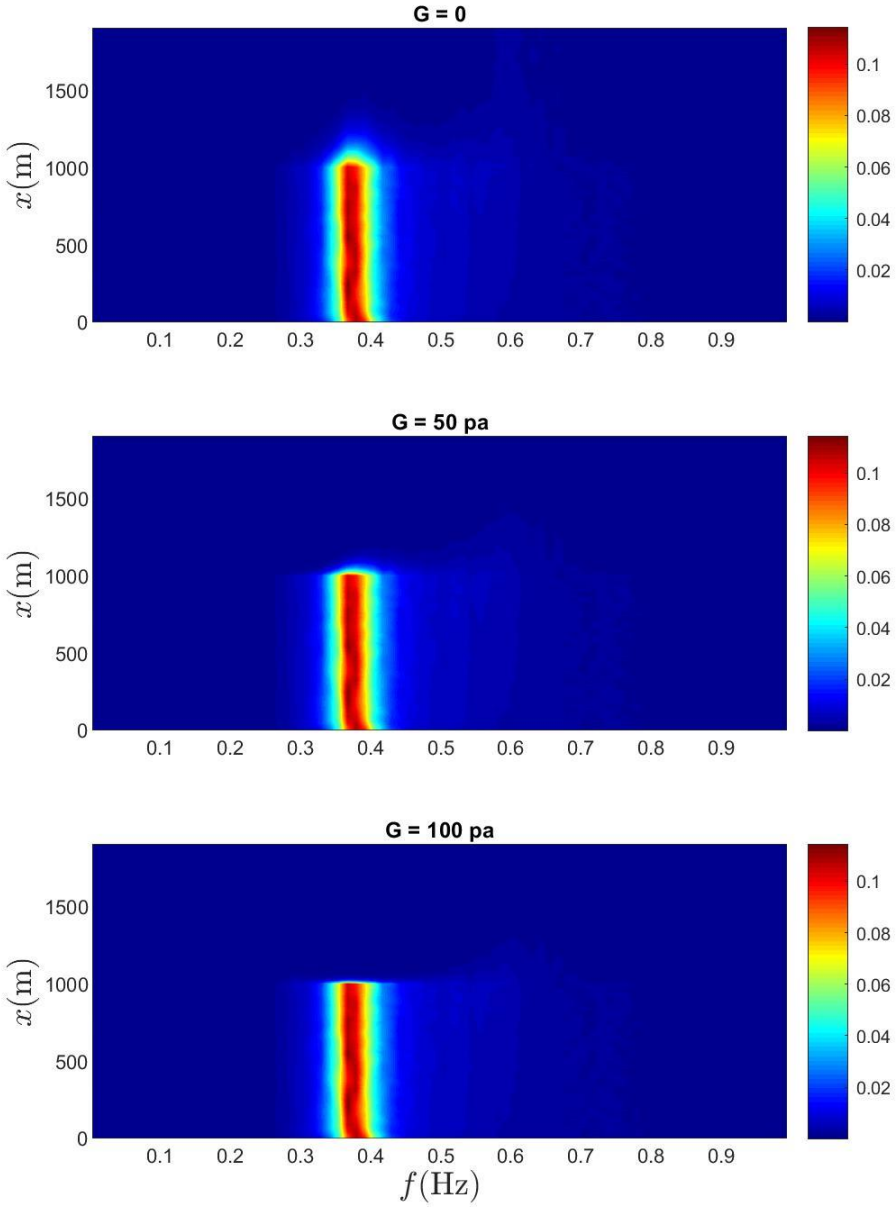

Figure 14. Spatial evolution of spectral energy density over muds with shear moduli of G = 0, 50 and 100 Pa, f_p = 0.40 Hz, ζ = 100, d_m = 0.20 m, h = 2.00 m.

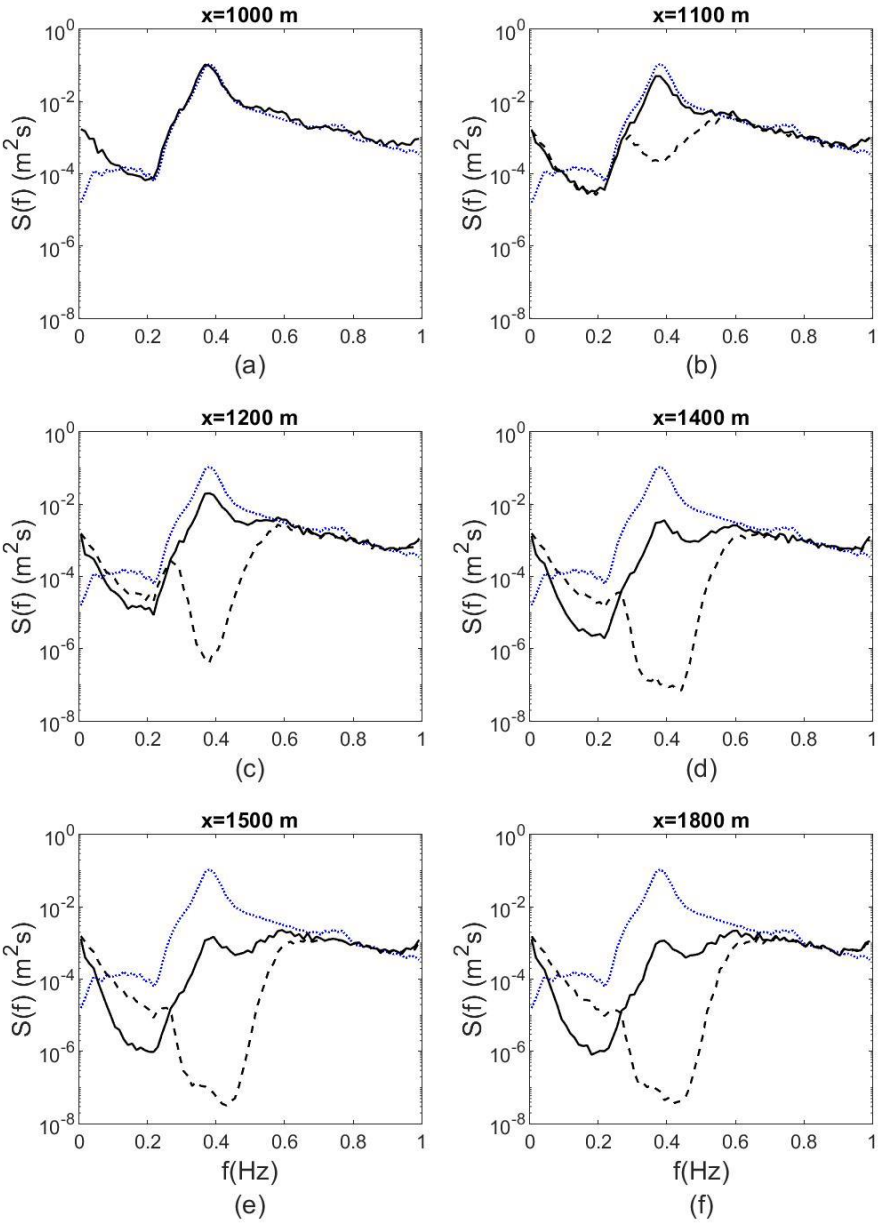

Figure 15. Surface wave spectrum over viscous (solid line) and viscoelastic (dashed line) mud with shear modulus of $G = 100\ Pa$ (dashed line), at discrete locations. The initial spectrum is shown by a dotted line, f_p = 0.40 Hz, ζ = 100, d_m = 0.20 m, h = 2.00 m.

It is noted that while the analytical damping rates are obtained using linear equations for a two-layer water/mud system, the wave model is based on the mild-slope equation for a homogeneous fluid thus the feedback from the mud layer to wave forcing is not considered. Previous research by Tahvildari et al. (2016) shows that transient nonlinear interactions between surface and interfacial waves over lutocline can result in significant damping of surface wave. We note that surface-internal wave interaction is a second-order phenomenon and direct damping by viscosity may dominate the process. However, over long distance and time, the process has the potential to drain considerable amount of energy from surface waves. Thus a comprehensive wave-mud interaction model should account for this high-order tow-layer process.

2.4. Discussion and Conclusions

In this chapter, the effects of mud viscoelasticity on evolution of surface waves is studied through numerical simulations. A new numerical wave-mud interaction model is developed by implementing an analytical model for mud-induced wave dissipation and modulation into a nonlinear frequency-domain phase-resolving model for surface wave propagation. The model enables studying the combined effect of mud viscoelasticity and nonlinear wave-wave interactions on evolution of surface wave spectrum. We compare the model with two experimental datasets and shows that not only the model compares well with laboratory measurements, but also its performances is superior to the model with viscous mud damping mechanism.

The model is used to simulate propagation of cnoidal waves over mud. The results show a strong dependency for wave amplitudes and phases on mud viscoelasticity. An earlier study by Kaihatu et al. (2007) shows that mud viscosity introduces a positive phase shift in surface wave

amplitude which is an increasing function of viscosity. In contrast, our results indicate that variation of phase difference can be non-monotonic over viscoelastic mud and depends on mud shear modulus for a given mud viscosity. The variability in wave phase can be attribute to non-monotonocity in variation of real part of surface wave number with mud shear modulus. Numerical simulations show that the evolution of the cnoidal wave spectrum over mud cannot be explained solely by examining the analytical damping rates of individual frequencies and nonlinear wave-wave interactions significantly affect frequency amplitudes. It was shown that, in agreement with previous studies that used viscous mud damping mechanism, subharmonic interactions can describe high damping in the high-frequency tail of the spectrum. The present work shows that this phenomenon is also present over viscoelastic muds, and may be independent of mud rheological model. It was also shown that the frequency-dependent damping in low-frequency end of the spectrum is dominated by the analytical damping rate of individual frequencies, which is highly affected by resonance in the mud layer.

Model results suggest that subharmonic interactions play a significant role in evolution of wave spectra through transfer of energy from high to low frequencies regardless of the magnitude of mud shear modulus. The results also indicate that in the absence of subharmonic interactions, low frequencies are damped substantially more strongly over viscoelastic muds compared to viscous mud indicating that subharmonic interactions substantially reduce damping of low frequencies in the presence of elastic effects.

The model is also applied to simulate random wave propagation. The pattern of spatial variation of H_{rms} over muds with different shear moduli can be explained by examining the distribution of analytical dissipation rates over frequencies. The highest analytical dissipation rates in the parameter space studied here belong to the mud with G = 100 Pa and the largest

reduction in H_{rms} is observed over mud with the same shear modulus. Resonance of the mud layer significantly affects the shape of random wave spectra, and intensity of this impact depends on the proximity of the spectral peak to resonance frequency; frequencies equal to resonance frequency experience the highest rate of dissipation. Similarly, the survival of higher harmonics which are triggered through superharmonic interactions largely depends on the relative magnitude of spectral peak and resonance frequencies. In the case where resonance frequency of the mud layer is out of the frequency range of the spectrum, superharmonics can maintain relatively high spectral energy density beyond mud patch only over the mud with a relatively high shear modulus. In contrast, if the spectral peak coincides with the resonance frequency, viscous mud damps the surface wave frequencies at a higher rate compared to viscoelastic mud only in low-frequency end of the spectrum and other frequencies experience higher damping over viscoelastic mud. The relatively weak damping of low frequencies over viscoelastic mud in this case can have implications in assessment of storm damage on coastal infrastructure as low frequencies in the spectrum have a higher likelihood of propagating to upland (e.g. Nwogu and Demirbilek, 2010). We note that dramatic spectral modulation as shown in Figure (9b) has not been documented in laboratory or field measurements. Therefore, these results call for new experiments to assess the impact of idealized viscoelastic bed or realistic mud that exhibits viscoelastic solid behavior on random surface wave spectrum.

The wave-mud interaction processes, including mud-induced wave attenuation, mud rheological behavior, and wave-induced mud fluidization, depend on wave properties, and bed permeability and porosity among other factors. The same mud specimen can exhibit different behaviors under different wave forcing and consolidation states making it challenging or even impossible to assign a single rhological model to mud. This underscores the need for models that

can simulate wave and mud behavior over a wide range of wave and mud parameters so that changing mud conditions can be captured. Jain and Mehta (2009) discuss the range of applicability of several mud rheological models for predicting surface wave attenuation as a function of solid volume fraction, $\phi = 1 - n$, where n is porosity, and a characteristic Pèclet number, which is defined as $Pe = \sigma d_p / K_p$ where σ is wave frequency, d_p is grain size, and K_p is permeability. They discuss that for relatively low values of Pe, as ϕ decreases, mud behavior progressively changes from viscoplastic solid to viscolestic solid to viscoleastic fluid and eventually to viscous fluid. This decrease in ϕ is accompanied by decrease in mud density. As Pe increases, the muddy bed behavior resembles a poroelastic solid. They also discuss that in low to moderate Pe values, viscoelastic solid (e.g. Voigt model) and fluid models (e.g. Maxwell model) can predict wave attenuation over the widest range of ϕ values. It is noted that in addition to mud porosity and permeability, the boundaries where mud transfers from one rheology to another is dependent on wave frequency. Jain and Mehta (2009) also compared the performance of fluid mud models, namely Maxwell and Jeffreys viscoelastic models and viscous model with laboratory measurement of wave attenuation. They shows that the Jeffreys model, which is a coupling of the Kelvin-Voigt model to a Maxwell element, outperforms the Maxwell model and both viscoelastic models compared better to experiments than the viscous model. Consequently, if ϕ is in moderate range of $\sim 0.20 - 0.40$, a viscoelastic solid model such as Voigt can represent mud behavior. If mud is in fluid state but solid volume fraction is small such that $\phi \sim 0.06 - 0.20$, a viscoelastic fluid model such as Jefferys or Maxwell would presumably be more appropriate, and if mud is in nearly complete fluid state such that $\phi < 0.06$, the viscous model should be more applicable.

The mud-induced wave evolution formulations used in the present wave-mud interaction model assumes the mud layer is thin. We examined the relevance of this assumption using reported field data reported in Liao et al. (2015). Their observed peak frequency of 0.15 Hz and total depths between 3.23 m and 3.76 m, result in a wavenumber of 4.53 rad/m which corresponds to $0.14 \leq kd \leq 0.54$. The spectral peak in their measurements is near the short wave range and since frequencies smaller than 0.10 Hz contain energy of an order of magnitude smaller than frequencies higher than the peak, most of the energy is confined in the range that mud can be considered thin. It should also be noted that although LC model is formally valid for thin mud layers, it may be applicable beyond this range. Through comparison with laboratory experiments, Kaihatu et al. (2007) showed that a wave-mud interaction that uses Ng (2000) mechanism (the $G = 0$ extreme of the LC model) performs well for relatively thick mud layers. This observation may indicate that even in thick mud layers, a thin top portion interacts with surface waves.

The results of the present work show that adequate characterization of mud layer and nonlinear wave processes are critical for accurate prediction of surface wave spectrum in the nearshore. By adding the effect of mud elasticity, the present model provides a more versatile predictive tool for wave propagation over muddy seabeds. There are several directions that the numerical model can be improved. In a comprehensive view, evolution of surface waves over mud is due to the combined effect of direct mud-induced dissipation and frequency modulation, nonlinear interactions among surface wave frequencies, wave-current interactions (e.g. Kaihatu and Tahvildari, 2012), and nonlinear interactions between surface and interfacial wave over lutocline (e.g. Hill and Foda, 1996; Jamali et al., 2003b; Tahvildari et al., 2016). The latter two processes are not considered in the chapter. Furthermore, the viscoelastic mud representation in

the present model assumes that the mud layer is thin. The expressions for damping rates and wavenumbers based on this assumption are straightforward to incorporate in a spectral wave model, and the coupled model may remain valid for thick mud layers. However, this wave-mud interaction model is formally limited to relatively thin layer of mud. Extension of the work to mud layer of arbitrary depth will involve finding the roots to a complex two-layer dispersion relation (Macpherson, 1980) using numerical methods. Extension of the model in these directions is studied in the next chapter.

CHAPTER 3 [2]

MODEL FOR WAVE PROPAGTION OVER MUD IN THE PRESENCE OF CURRENT

The coupled wave-current-mud interaction model integrates the wave-current interaction model of Kaihatu (2009) which simulates nonlinear propagation of waves in the presence of currents, and two mechanisms for mud-induced surface wave evolution formulated by Macpherson (1980) and Liu and Chan (2007).

3.1 Nonlinear Wave-Current Interaction Model

The wave-current interaction model is based on the Kaihatu (2009) model. In this model, second-order effects are added to the wave-current interaction model of Kaihatu and Kirby (1995) and energy transfer calculations in high frequencies are improved. This model is based on the mild-slope equations (Smith and Sprinks, 1975) and solves the nonlinear interactions among resonant triads (e.g. Philips, 1981). Since the model uses parabolic approximation, it is applicable to weakly two-dimensional waves (Radder, 1979). The governing equations assume irrotational flow and slow-varying depth. The ambient current, U, is constant in the vertical direction, z, but can change in the horizontal directions (x, y). Here we only describe the main components of the model and refer the reader to Kaihatu and Kirby (1995) and Kaihatu (2009) for more details. The velocity potential function is given by,

$$\phi(x, y, z) = \phi_0(x, y) + f_n(k_n, h, z)\phi_n(k_n, \omega_n, x, y, t), \qquad (23)$$

[2] This chapter is based on the manuscript "Numerical modeling of current effects on nonlinear surface wave propagation over viscoelastic mud", Sharifineyestani E., Tahvildari N., in review in Ocean Modeling Journal

where subscript n denotes the nth harmonic, the derivative of the zeroth order term, ϕ_0, in the horizontal direction gives the ambient current: $U = \nabla\phi_0$, h is water depth, k is wavenumber, ω is wave frequency. The time-periodicity and the vertical variability of the flow are represented by ϕ_n and f_n, respectively and are given by,

$$f_n(z) = \frac{\cosh k_n(h+z)}{\cosh kh}, \quad (24)$$

$$\phi_n = -\frac{igA_n}{2\sigma_n} e^{i\int k_n dx - \omega_n t} + c.c. \qquad (25)$$

where A_n is the amplitude of the nth surface wave harmonic, σ_n is the intrinsic frequency of the nth harmonics, g is the gravitational acceleration, $i = \sqrt{-1}$, and $c.c.$ shows the complex conjugate. The propagation of surface waves over slowly varying depth in one horizontal dimension is given (e.g. Eldeberky and Battjes, 1996) in frequency domain as,

$$\frac{\partial A_n}{\partial x} + \frac{\sigma_n}{2(C_{gn}+U)}\left[\frac{\partial}{\partial x}\left(\frac{C_{gn}+U}{\sigma_n}\right)\right]A_n + D_n A_n \qquad (26)$$

$$= \frac{-i}{8(C_{gn}+U)\sigma_n}\left(\sum_{l=1}^{n-1} RA_l A_{n-1} e^{i\Theta_{l,n-1}} + 2\sum_{l=1}^{N-n} SA_l^* A_{n+1} e^{i\Theta_{n+l,-1}}\right)$$

where C_{gn} and D_n are the group velocity and the dissipation rate of the nth harmonic, respectively. The nonlinear interaction coefficients R and S represent the super- and sub-harmonic interactions, respectively. The Kaihatu (2009) model includes a correction to A_n to account for second-order effects in the dynamic free-surface boundary condition. The resulting corrected harmonic amplitude, B_n, is calculated as,

$$B_n = A_n + \frac{1}{4g}\left[\sum_1^{n-1} IA_l A_{n-l} e^{\Theta_{l,n-l}} + 2\sum_1^{N-n} JA_l^* A_{n+l} e^{\Theta_{n+l,l}}\right] \qquad (27)$$

where I and J are nonlinear interaction coefficients.

At the leading order, ambient currents modify wave frequencies through Doppler shift. Two frequencies need to be defined to quantify this effect. The absolute frequency, ω, is measured with respect to a fixed reference frame, and the intrinsic frequency, σ, is measured with respect to the coordinate system that is moving at the speed of the background current. The relationship between these two frequencies is,

$$\omega = \sigma + kU \quad (28)$$

where $\sigma^2 = gktanh(kh)$. The term $D_n A_n$ in equation (26) represents energy dissipation which can be due any interaction between waves and the surrounding environment, e.g. depth-limited breaking, mud, or aquatic vegetation.

3.2 Model for Surface Wave Evolution over Viscoelastic Mud

The effect of viscoelastic muds on surface waves include viscous dissipation and frequency modulation due to elasticity. In dissipative media, the wave number or frequency is considered to be a complex wave number and their imaginary part represents a spatial or temporal damping rate, respectively (e.g. Macpherson, 1980). Frequency modulation is represented by changes in the real part of wave number or frequency. Therefore, solving wave evolution over mud require solving a complex dispersion relation of a two-layer mud/water system which depends on wave characteristics, and properties of water and mud layers. In this study, we use the viscoleastic mud models of (Macpherson, 1980) and (Liu and Chan, 2007) to investigate current effects on mud-induced wave evolution. Since the model of (Liu and Chan, 2007) is a the thin-mud limit of (Macpherson, 1980), comparison between results using these two models sheds light on the effect of thin-mud-layer assumption on surface wave evolution.

3.2.1 Macpherson (1980) Model

Macpherson (1980) investigated surface wave attenuation in a two-layer system composed of an inviscid water overlaying a viscoelastic layer of solid that represented sediment and was described by the Voigt model. He used the Navier-Stokes equations but substitution mud viscosity with a complex number that represented viscoelasticity ν_{me} formulated as,

$$\nu_{me} = \nu_m + \frac{iG_m}{\sigma\rho_m}, \qquad (29)$$

where the real and imaginary parts represent mud's viscosity and elasticity, respectively. In this equation, ν_m, G_m, ρ_m are mud's viscosity, shear modulus of elasticity, and density, respectively. The viscosity of the water is neglected and it is assumed that its density is smaller than that of mud. Also, shear stress and mixing at water-mud interface are neglected. The dispersion relation for this two-layer system is given by,

$$\frac{\rho_w(\sigma^4 - g^2k^2)\tanh(kh)}{gk\tanh(kh) - \sigma^2} + \rho_m gk + T'k^3 \quad (30)$$

$$+\rho_m(2k^2\nu_{me} - i\sigma)^2\left[\frac{\left(2k^2 - \frac{i\sigma}{\nu_{me}}\right)[lC_mC_l - kS_mS_l] - 2k^2l}{\left(2k^2 - \frac{i\sigma}{\nu_{me}}\right)[lS_mC_l - kC_mS_l]}\right]$$

$$-4\rho_m k^3 {\nu_{me}}^2 l\left[\frac{\left(2k^2 - \frac{i\sigma}{\nu_{me}}\right) - 2k[kC_mC_l - lS_mS_l]}{2k[lS_mC_l - kC_mS_l]}\right] = 0$$

where $C_m = \cosh(kd)$, $C_l = \cosh(ld)$, $S_m = \sinh(kd)$, $S_l = \sinh(ld)$, $l = (k^2 - \frac{i\sigma}{\nu_{me}})^{0.5}$ and T' is the surface tension which is assumed to be negligible here. Solving this dispersion relation for wave number, k, gives the modulated frequency, k_r (Re(k)) and damping rate, D_m (Im(k)). This dispersion relation should be solved numerically, and it should be noted that the roots in the

complex plane may be non-unique making the solution procedure at times laborious and the correct root ambiguous (Mendez and Losada, 2004). This non-uniqueness problem can make implementation into predictive wave models difficult, unless relevant roots are precalculated and implemented (Ng and CHIU, 2009).

3.2.2 Liu and Chan(2007) Model

In the Liu and Chan(2007) model for viscoelastic mud, the dispersion relation has been simplified by assuming that the mud layer is thin. This assumption allows derivation of explicit solutions for real and imaginary part of the wave number from a complex dispersion relation and eliminates the possibility of obtaining multiple roots. The implementation of the solution in spectral wave models is straightforward (Tahvildari and Sharifineyestani, 2019). The basic assumption in this formulation is that the mud layer is thin and is of the same order of magnitude as the bottom boundary layer within mud:

$$k_r a \approx k_r d_m \approx k_r \delta_{me} \ll 1 \quad (31)$$

where k_r is the real part of wave number and in non-dimensional form is as follows:

$$k_r h = k_1 h - \frac{(k_1 h)^2 \gamma\left(\frac{\delta_{me}}{h}\right)}{\sinh 2k_1 h + 2k_1 h}\left[2\lambda - \frac{\Omega_M \sinh 2\lambda\Omega_M + \Omega_P \sin(2\lambda\Omega_P)}{\cosh(2\lambda\Omega_M) + \cos(2\lambda\Omega_P)}\right], \quad (32)$$

and δ_{me} is the mud boundary layer given by,

$$\delta_{me} = \sqrt{\frac{2|\nu_{me}|}{\sigma}}, \qquad (33)$$

where ν_{me} is the effective kinematic viscosity of mud (e.g. Macpherson, 1980). Liu and Chan (2007) (referred to as LC hereafter) derived the dispersion relation for a two-layer system composed of inviscid water overlying a relatively thin layer of viscoelastic mud and obtained an

analytical solution for the complex wavenumber. The imaginary part of the complex wave number is the spatial damping rate, D_m, and in non-dimensional form is given by,

$$D_m h = \frac{(k_1 h)^2 \gamma\left(\frac{\delta_{me}}{h}\right)}{\sinh 2k_1 h + 2k_1 h}\left[\frac{\Omega_P \sinh 2\lambda\Omega_M - \Omega_M \sin(2\lambda\Omega_P)}{\cosh(2\lambda\Omega_M) + \cos(2\lambda\Omega_P)}\right] \qquad (34)$$

where

$$\sigma^2 = g k_1 \tanh k_1 h, \qquad (35)$$

$$\lambda = \frac{d_m}{\delta_{me}}, \qquad (36)$$

$$\Omega_P = \cos\frac{\theta}{2} + \sin\frac{\theta}{2}, \qquad (37)$$

$$\Omega_M = \cos\frac{\theta}{2} - \sin\frac{\theta}{2}, \qquad (38)$$

$$\tan\theta = \frac{G_m}{\sigma \rho_m \nu_m}, \qquad (39)$$

$$\gamma = \frac{\rho_w}{\rho_m} \qquad (40)$$

where k_1 is the surface wavenumber for a single layer fluid in the absence of mud, and h and d_m are the depth of water and mud layers, respectively.

3.2.3 Comparison between Viscoelastic mud models

The damping rates obtained from three viscoelastic mud models is shown in Figure (16). The figure shows variation of damping rates for viscous and viscoelastic mud with shear modulus of G=100 Pa using formulations of Liu and Chan (2007) (equation 34) and Macpherson (1980) (equation 30), and values extracted from Piedra-Cueva(1993). In this figure, is $\zeta = \sqrt{\nu_m/\nu_w}$ =100, where ν_w is the kinematic viscosity of water, $d_m = 0.06$ m, $h = 0.30$ m, $\rho_m = 1370$ kg/m ^{3}, $\rho_w = 1000$ kg/m ^{3}and frequency changes between $0 - 1.7$ Hz. As seen, the

variation of damping with $d_m.\sqrt{\omega/\nu_m}$ is non-monotinic for both viscous and viscoelastic scenarios and resonance effect, which is manifested by intensified damping, is evident for the viscoelastic case at $d_m.\sqrt{\omega/\nu_m}$ of around 2. A surface wave with a frequency equal to the natural frequency of oscillation in the mud layer resonates with the mud layer and amplifies interfacial motions which results in intensified viscous damping. All the three formulations show the resonance effect and agree well in the range of parameters used.

Figure (17) shows the variation of damping rate (D_m) with surface wave frequency (f) for various values of mud shear modulus and currents. The damping rates shown in this figure assume that relative viscosity is $\zeta = \sqrt{\nu_m/\nu_w}$ = 100, $d_m = 0.12$ m, $h = 1.00$ m, $\rho_m = 1111$ kg/m ^{3}, the density of water is ρ_w = 1000 kg/m ^{3}. The damping rates are smallest at the low and high ends of the frequency range and their variation depends on mud shear modulus and current velocity. Viscous mud consistently causes the highest dissipation rate at low frequencies, regardless of the current magnitude. As seen in the figure, the variation of D_m with f is stronger over viscoelastic muds compared to viscous mud. The highest damping over viscoelastic mud occurs at a frequency equal to mud's resonance frequency as it triggers large oscillations and subsequent viscous damping within the mud layer. As seen in Figure (17), for the parameters studied here, the maximum damping rate consistently increases with mud shear modulus up to $G_m = 100$ Pa and decreases thereafter. The effect of currents on damping rate is shown in the same figure. Three current magnitudes of $U = 0, \pm 0.15$ m/s corresponding to Froude numbers $Fr = U/\sqrt{gh} = 0, \pm 0.05$ are used. As seen, for the viscous case and when $f < 0.5$ Hz, the wave damping rate over opposing current is larger than both the cases without current and with co-propagating current. This trend is reversed for $f > 0.5$ Hz. The case with viscous mud damping is the same as that studied in Kaihatu and Tahvildari(2012) but with thinner mud layer. The same

trend in $D_m - f$ variation is seen for viscoelastic muds as seen in Figure (17), and it is noted that reversal in trend occurs at 0.5 Hz regardless of the value of mud shear modulus. As mud shear modulus increases, current effects on damping rates become more pronounced for frequencies larger than 0.5 Hz.

The total energy of a frequency over mud depends on direct damping, which is calculated using equations (30), and (34), and its energy loss or gain due to nonlinear energy transfer across the spectrum (Kaihatu et al., 2007; Safak et al., 2017; Tahvildari and Sharifineyestani, 2019). Therefore, the evolution of surface waves over mud is adequately understood only if a spectral model with capability of resolving nonlinear wave interactions is utilized. To address this, we incorporate mechanisms for viscoelastic mud-induced evolution in a nonlinear frequency-domain spectral model for wave-current interaction developed by Kaihatu (2009), and apply the coupled model to solve the spatial evolution of surface waves.

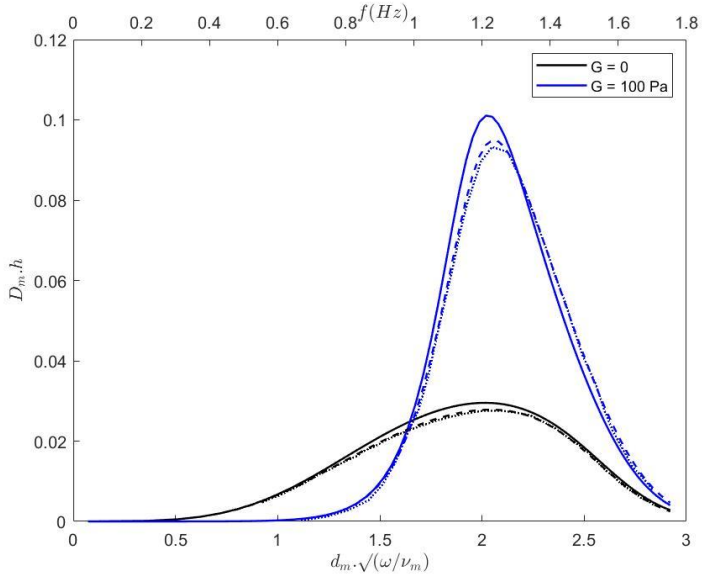

Figure 16. Surface wave damping rate as a function of frequency for different shear moduli of mud using formulation of Liu and Chan(2007) (solid line), Macpherson(1980) (dashed line) and Piedra-Cueva (1993) (dot line), $\zeta = 100$, $h = 0.30$ m, $d_m = 0..09$ m, and $\rho_m = 1370$ kg/m ^{3}.

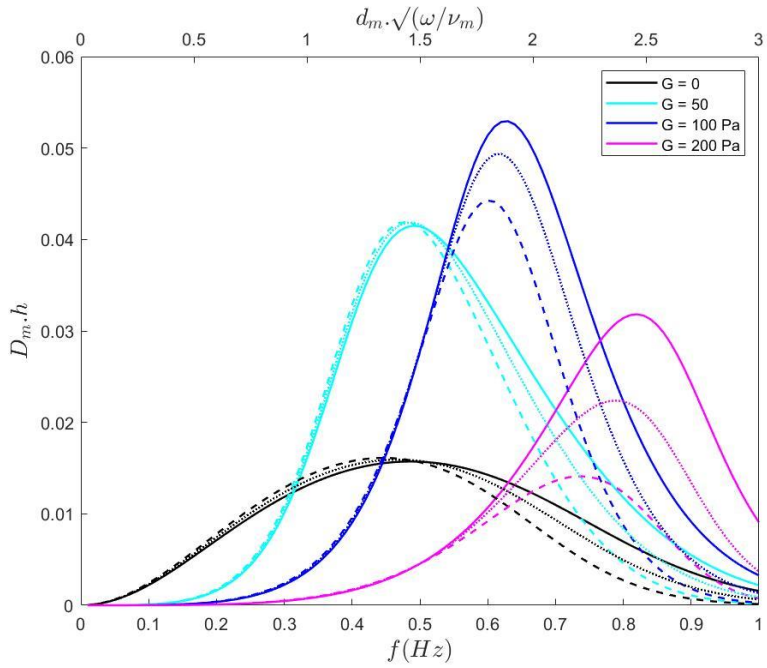

Figure 17. Surface wave damping rate as a function of frequency for different shear moduli of mud in the presence of co-propagating current with $U = +0.15$ m/s (solid line), without current (dot line), and in the presence of counter-propagating current with $U = -0.15$ m/s (dashed line), $\zeta = 100$, $h = 1.00$ m, $d_m = 0.12$ m, and $\rho_m = 1111$ kg/m ^{3}.

3.3 Model results

The results of the numerical model are presented in this section. First, we validate the model with laboratory experiments and then utilize the model to show the effect of mud viscoelasticity on wave evolution in the presence of currents. Monochromatic and random wave scenarios are simulated.

3.3.1 Model validation

As discussed earlier, mud can show different rheological properties under various wave conditions. Properties of bottom mud layer such as density, viscosity, and thickness can vary widely in the filed depending on hydrodynamic conditions and consolidation. There is no control over these conditions in the field making comparison between field data and numerical models complicated. In contrast, the uncertainty in properties of the mud layer and complexities in flow

conditions are smaller in laboratory experiments. Therefore, there is closer correspondence between laboratory experiments and numerical wave models as they generally assume that the mud rheology and properties are constant over time and space. While there are some labrotary datasets on wave dissipation over mud (e.g. De Wit, 1996; Jiang and Mehta, 1996; Soltanpour and Samsami, 2011) there are a limited number of studies on the wave-mud interactions in the presence of currents. Here we utilize the experimental data in Zhao et al. (2006) to validate our model. The range of parameters used in their experiments is: $d_m = 06 - 12$ cm, $h = 24 - 28$ cm, $\rho_m = 1190 - 1400$ kg/m ^{3}, $G = 0.4 - 25$ Pa, wave period $= 0.82 - 1.61$ s, and wave height $1.8 - 10$ cm. The damping rate is calculated using the following equation and compared with reported values in Zhao et al. (2006):

$$H(x) = H_0 e^{-D_s \cdot x}, \qquad (41)$$

where D_s indicates surface wave damping rate. Figure (3) shows the comparison between the damping rates acquired from the wave-current-mud interaction model, in viscous and viscoelastic modes, and the laboratory experiments of Zhao et al. (2006). While the model compares well with lab data using either viscous and viscoelastic mud mechanisms, the model with viscoelastic mechanism shows a slightly better performance. The RMSE of the viscoelastic and viscous mud models are 0.00255 m^{-1} (with $R^2 = 0.99$) and 0.00342 m^{-1} (with $R^2 = 0.98$), respectively. We also compared the attenuated height of monochromatic waves as reported from several experiments of Zhao et al. (2006) with those obtained from the present model. Figure (19) shows a satisfactory comparison between the model and experimental data.

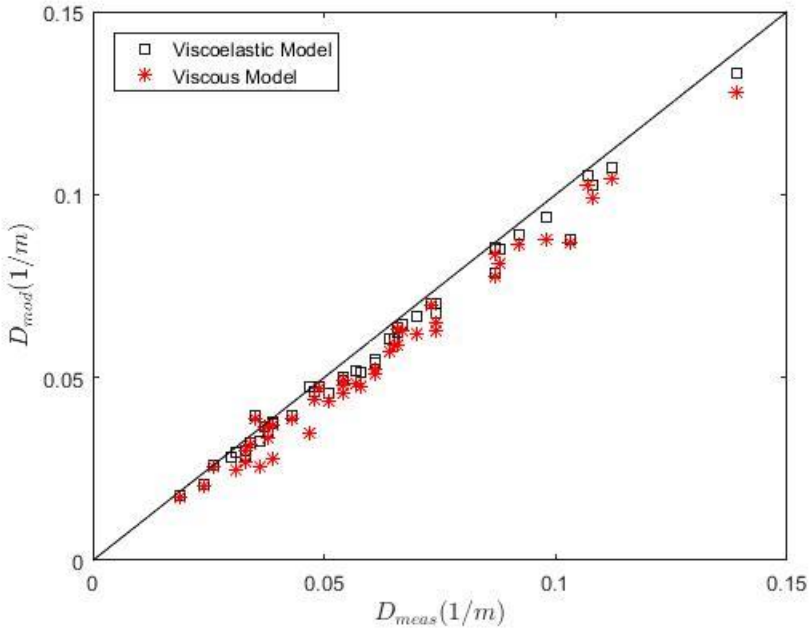

Figure 18. Comparison between the attenuation rate from the present model and laboratory experiments of Zhao et al. (2006).

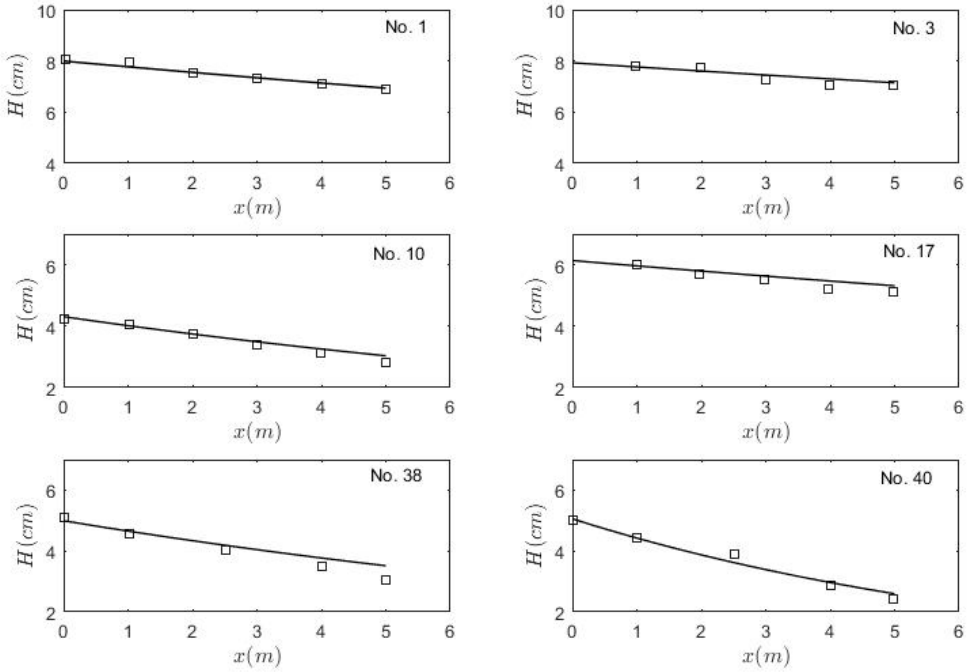

Figure 19. Comparison between the attenuated wave heights from the present model (black line) and experiments of Zhao et al. (2006) (squares).

3.3.2 Effect of current on propagation of monochromatic waves over mud

In this section, the wave-current-mud interaction model is utilized to assess the impact of currents on wave energy dissipation due to a viscoelastic mud layer. Consistent with the underlying assumption in the model for mud behavior, the mud layer is assumed to be relatively thin. We simulate the evolution of monochromatic waves using cnodial waves. While multiple frequencies are present, they propagate at the same speed and their superposition creates the permanent form solution to equations (26) and (27) (Kaihatu, 2001). Investigating the evolution of permanent wave solution is informative since we can assess the combined effect of nonlinearity and frequency-dependent mud-induced dissipation without the complexities that an irregular wave spectrum, containing numerous frequencies, introduces in wave evolution. The permanent form solution used in our simulations is developed by Kaihatu (2009) (equation 26) and is produced by superposition of the component amplitudes that are harmonics of a fundamental frequency.

The variation of amplitude spectrum of cnoidal waves with frequency for different magnitudes of shear modulus, $G = 0 - 200$ Pa, is shown in Figure (20). The simulations are performed in a domain of length 1000 m in which the mud patch is placed at $x = 300 - 800$ m and the grid resolution is $\Delta x = 0.025$ m. A total of 10 harmonics are utilized for generation of a cnoidal wave with the fundamental frequency of $f = 0.10$ Hz. The wave height is $H = 0.1$ m, and the current has three values of $0, \pm 0.15$ m/s corresponding to the Froude numbers $F_r = U/\sqrt{gh} = 0, \pm 0.05$. The values of mud layer thickness and water depth are 0.12 and 1.00 m, respectively, and the relative viscosity is $\zeta = \sqrt{\nu_m/\nu_w} = 100$. The range of frequency is $0.10 \leq f \leq 1$ Hz corresponding to $0.20 \leq kh \leq 4$. This range of frequencies, mud properties, and water depth were selected such that mud layer remains dynamically thin, consistent with the LC model.

The initial spectrum at $x = 0$ and the spectrum in the lee of the mud patch at $x = 800$ m are shown in the figure. Generally, it is seen that damping decreases as G increases regardless of the direction of the current. For viscous mud, frequencies smaller than $f = 0.6$ Hz experience stronger damping in the presence of an opposing current than a following current. However, this trend changes in larger frequencies such that opposing current results in weaker dissipation. As mud's shear modulus increases, the frequency at which the change in dissipation trend occurs increases to $f = 0.82$ Hz for $G = 50$ Pa and $f = 0.92$ Hz for $G = 100$ Pa. No change in trend is observed for a mud with $G = 200$ Pa.

The trend in dependency of mud-induced dissipation on mud's shear modulus cannot be explained entirely by frequency-dependent damping rates (Figure (17)). As discussed earlier, the damping rates in the presence of an opposing current is stronger than those in the presence of following current for frequencies less than ≈ 0.5 Hz regardless of shear modulus. However, the point of reversal in this trend is ≈ 0.60 Hz which shifts to higher frequencies as G increases. Since the damping rates of LC are computed using linearized equations of motion, it can be concluded that nonlinear wave-wave interactions are responsible for this slight inconsistency. To better understand the reason of this difference, the model is run with subharmonic nonlinear interactions deactivated. Model simulation results for cases with and without currents with subharmonic interactions are deactivated are shown in Figure (21). Figure (21) indicates that the variation of amplitudes with frequency follows the pattern of direct damping rate. As seen, when there is no current the amplitude spectrum over viscous mud intersect with viscoleatsic mud with shear modulus $G = 100$, and 200 Pa at 0.5 Hz and 0.65 Hz respectively, which are close to the intersection frequencies of viscoelastic and viscous damping rates in Figure (17). The intensity of damping across frequencies can shift to lower or higher end of the spectrum depending on the

direction of the current. As seen in the Figure (21), for a viscoelastic mud with G = 100 Pa, damping in the presence of a following current is stronger than that in the presence of an opposing current in the range of mid to high frequencies as a following (opposing) current shifts more energy to higher (lower) frequencies where they experience higher (weaker) damping (Figure 17). It is also noted that on the high-frequency end of the spectrum, the change in frequency amplitudes with respect to incident wave spectrum is small. This is in agreement with findings of Tahvildari and Sharifineyestani (2019) for waves over viscoelastic mud in the absence of currents and with Kaihatu and Tahvildari (2012) for waves over viscous mud in the presence of currents indicating that damping of higher frequencies are due to subharmonic interactions regardless of the magnitude of mud shear modulus, and presence and direction of currents.

Figure (22) shows the spatial variation of the root-mean-square wave height (H_{rms}) of the spectrum shown in Figure (20) for different values of mud shear modulus. As expected, H_{rms} follows the pattern reported in Kaihatu and Tahvildari (2012) for viscous mud where damping in the presence of the following current is less than that in the presence of opposing current. For scenarios with $G = 50{,}100$ Pa, H_{rms} shows undulations with x and at the end of the mud patch the wave is most heavily and most weakly damped in the presence of a following and an opposing current, respectively. The trend in H_{rms} variation reverts to that over viscous mud for a viscoelastic mud with $G = 200$ Pa, in which the opposing and following current results in low damping but damping in the presence of opposing current is more than that than the following current. The variation of H_{rms} with space is attributed to frequency-dependent damping rate (Figure (17)). Most of the energy in the cnoidal wave spectrum is confined in frequencies lower than 0.50 Hz where D_m is consistently higher for opposing currents for viscous mud and

viscoelastic mud with $G = 200$ Pa. However, as discussed earlier, D_m is larger for opposing currents for muds with $G = 50$ and 100 Pa over low frequencies while D_m for a following currents exceeds that of an opposing current for larger frequencies in the $0 < f < 0.50$ Hz range.

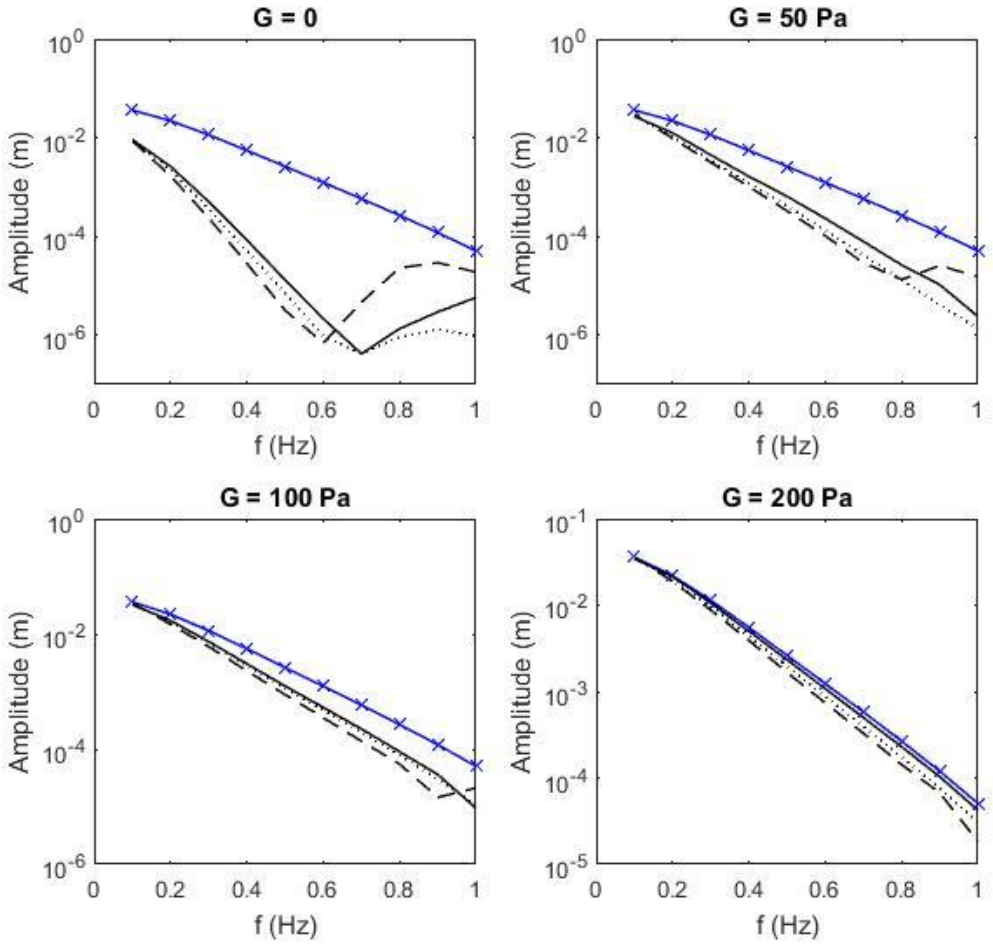

Figure 20. Propagation of cnodial wave spectrum over mud with shear moduli of $G = 0 - 200$ Pa. Blue-solid-x line: the initial spectrum at $x = 0$, black-solid line: the spectrum for $U = +0.15$ m/s, black-dashed line: the spectrum for $U = -0.15$ m/s, and black-dot line: the spectrum for $U = 0$, at the end of mud patch ($x = 800m$). $h = 1.00$ m, $d_m = 0.12$ m, and $\rho_m = 1111$ kg/m ^{3}.

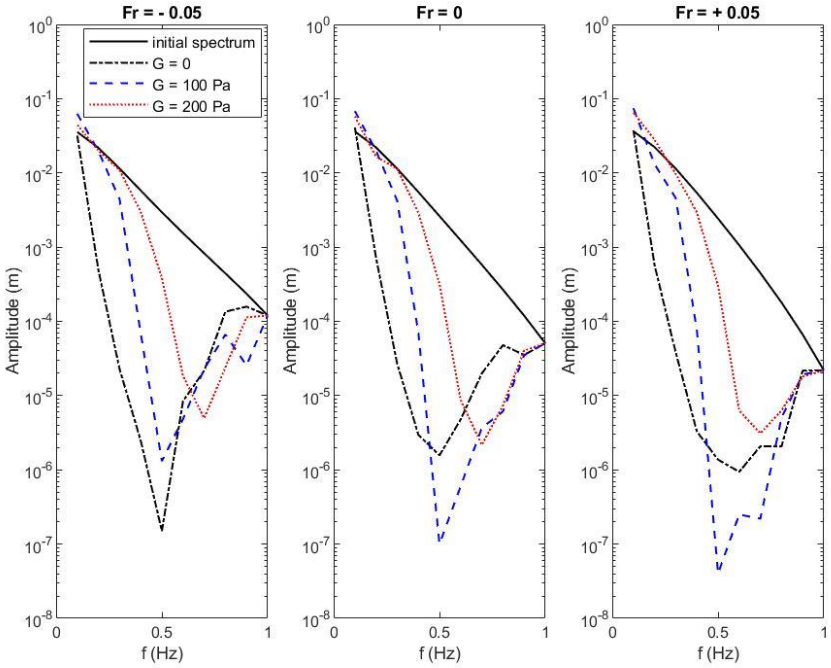

Figure 21. Evolution of a cnoidal wave spectrum over muds with subharmonic interactions deactivated. Wave and mud parameters and water depth are the same as those in figure (20).

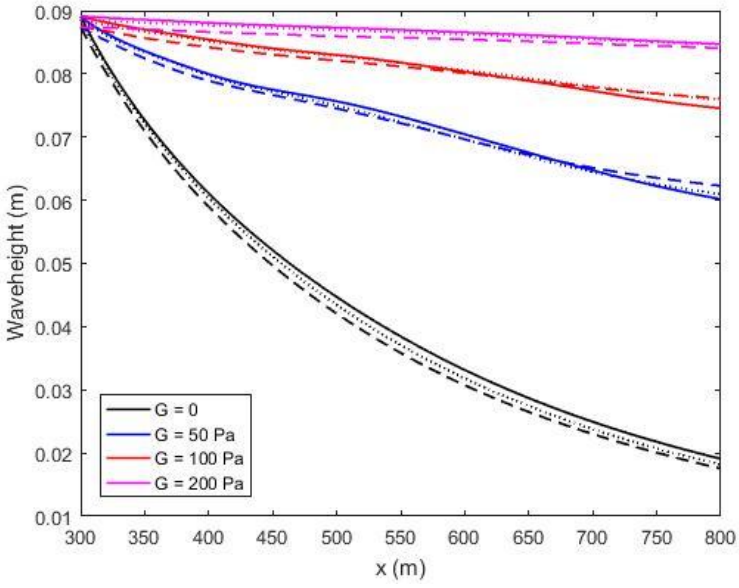

Figure 22. Spatial variation of cnodial wave H_{rms} over viscous ($G = 0$) and viscoelastic mud with shear moduli of $G = 50 - 300$ Pa. dot-line: $U = 0$, solid-line: $U =$ +0.15 m/s , and dashed-line: $U =$ -0.15 m/s. The mud patch is located at x = 300-800 m, ζ = 100, h = 1.00 m, $d_m = 0.12$ m, and $\rho_m = 1111$ kg/m ^{3}.

3.3.3 Effects of currents on the propagation of random wave spectra over mud

The impacts of currents on the random wave evolution over viscoelastic mud is investigated in this section. The simulations use the TMA form spectrum (Bouws et al., 1985) and are performed in a domain of length 4900 m in which mud is placed between $1000 - 1500$ m. The H_{rms} of initial spectrum and depth of water are 0.24 m and 2.00 m, respectively resulting in the Ursell number of 2.08, where

$$U_r = \frac{\delta}{\mu^2}, \qquad (42)$$

where $\delta = \frac{H_{rms}}{2h}$, and $\mu = kh$.

The evolution of two spectra with peak frequencies $f_p = 0.0625$ and 0.26 Hz are investigated. The mud and water layer properties are $d = 0.20$ m, and $\zeta = 100$ which result in the resonance frequency of $f_r = 0.26$ Hz for $G = 50$ Pa. We used the mud properties that result in relatively high damping rates ($\zeta = 100$ and $d = 0.20$ m) and ran the model for various magnitudes of shear modulus. With these specifications, we chose the frequencies in a range which results in $k_r . d_m < 1$ corresponding to a relatively thin mud layer.

The evolution of random wave spectra with peak frequency of $f_p = 0.0625$ Hz over viscous and viscoelastic muds is shown in Figure (24) and the corresponding damping rate is shown in figure (25). As seen in Figure (24), the initial spectrum and the spectrum at the end of the mud patch (x = 1500 m) are shown for $Fr = \pm 0.15$ and shear moduli of $G = 0{,}100$ Pa. In the scenario with viscous mud (Figure (24a)), while energy level in low to mid-range frequencies in the presence of opposing current is comparable to that in the presence of following current at the end of the mud patch, higher frequencies clearly undergo stronger damping in the presence of an opposing current. The difference between wave damping in the presence of following and

opposing currents is smaller over viscoelastic mud compared to viscous mud (Figure (24b)). It is noted that spectrum expands quickly in frequency regardless of mud shear modulus and current direction and there is no apparent peaks in the spectrum at the lee of mud. Kaihatu and Tahvildari (2012) simulation also indicate that the spectrum with relatively high U_r (2.08) undergoes rapid broadening over frequency while a spectrum with a smaller U_r (e.g. 0.78) maintains its structure.

The spatial evolution of several frequencies, namely the subharmonic ($f_p/2$), first (f_p), second ($2f_p$), and third ($3f_p$) harmonics of peak frequency is shown in Figure (24c-f). As expected, the spectra undergoes some evolution initially where the subharmonic gains some energy at the expense of the first three harmonics, but the subharmonic and harmonics reach an equilibrium state. The dissipation is stronger over viscous mud compared to viscoelastic mud, particularly for higher harmonics.

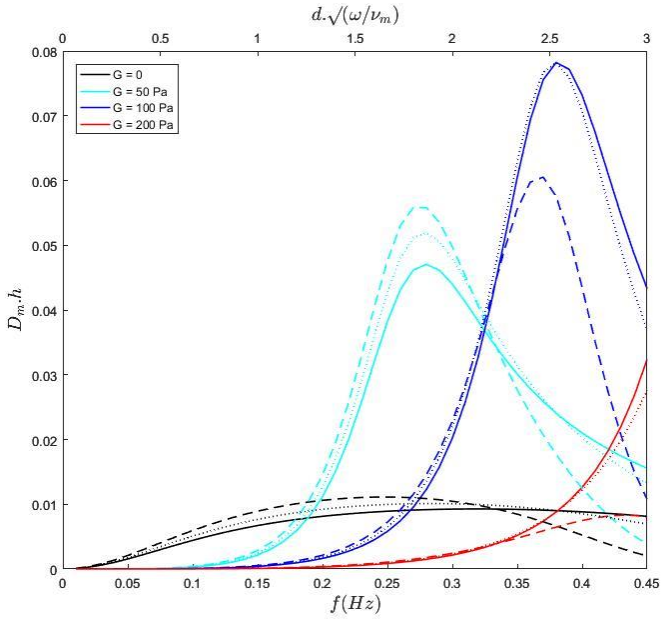

Figure 23. Variation of surface wave damping rate with frequency for different values of mud shear modulus. Solid line: Fr $= +0.15$ m/s, dot line: Fr $= 0$, and dashed line: Fr $= -0.15$ m/s. ($\zeta = 100$, h $= 2.00$ m, $d_m = 0.20$ m, and $\rho_m = 1111$ kg/m ^{3}).

Figure (25) shows the spatial variation of H_{rms}. Similar to the case with cnoidal waves, the damping due to opposing current is stronger than that in the following current over viscous mud while the trend reverses as mud shear modulus increases. It is noteworthy that this reversal in trend is consistent with x for all G values for a random wave spectrum and the undulations seen for a cnoidal wave (Figure (22)) are not present.

As discussed earlier, a significant property of viscoelastic mud is its capacity to resonate with the surface wave. To better evaluate the resonance effects on a random wave spectrum, we simulated the propagation of a spectrum with peak frequency at $f = 0.28$ Hz which is equal to the frequency at which maximum direct damping occurs due to resonance for a mud layer with shear modulus of $G = 50$ Pa. Figure (26) shows the spatial variation of H_{rms} of this spectrum for various values of shear modulus of elasticity ($G = 0 - 300$ Pa) and currents with $F_r = 0, \pm 0.15$. As seen, H_{rms} initially decreases over mud with increase in G up to $G = 50$ Pa and the opposing current results in more damping for muds with G up to 100 Pa along the domain consistently. However, H_{rms} damping decreases for G higher than 50 Pa and for $G = 200$ Pa, a following currents results in more damping in the beginning of the mud patch whereas the opposing currents results in stronger damping from $x = 1250$ m and onward. The following current intensifies mud-induced damping along the domain consistently over a mud with $G = 300$ Pa. It is apparent that the strongest overall damping occurs when the random wave is propagating over a mud with shear modulus $G = 50$ Pa as expected from the pattern of direct mud-induced wave damping (Figure (23)). It is noteworthy that spatial variability in damping rate of H_{rms} is affected by G and U such that for $G = 0$ and 50 Pa, initial damping rate of H_{rms} is stronger at

the beginning of the mud patch compared to the rate at its end where the H_{rms} curve becomes nearly horizontal. However, this variability is weaker for muds with $G = 0{,}200$ and 300 Pa.

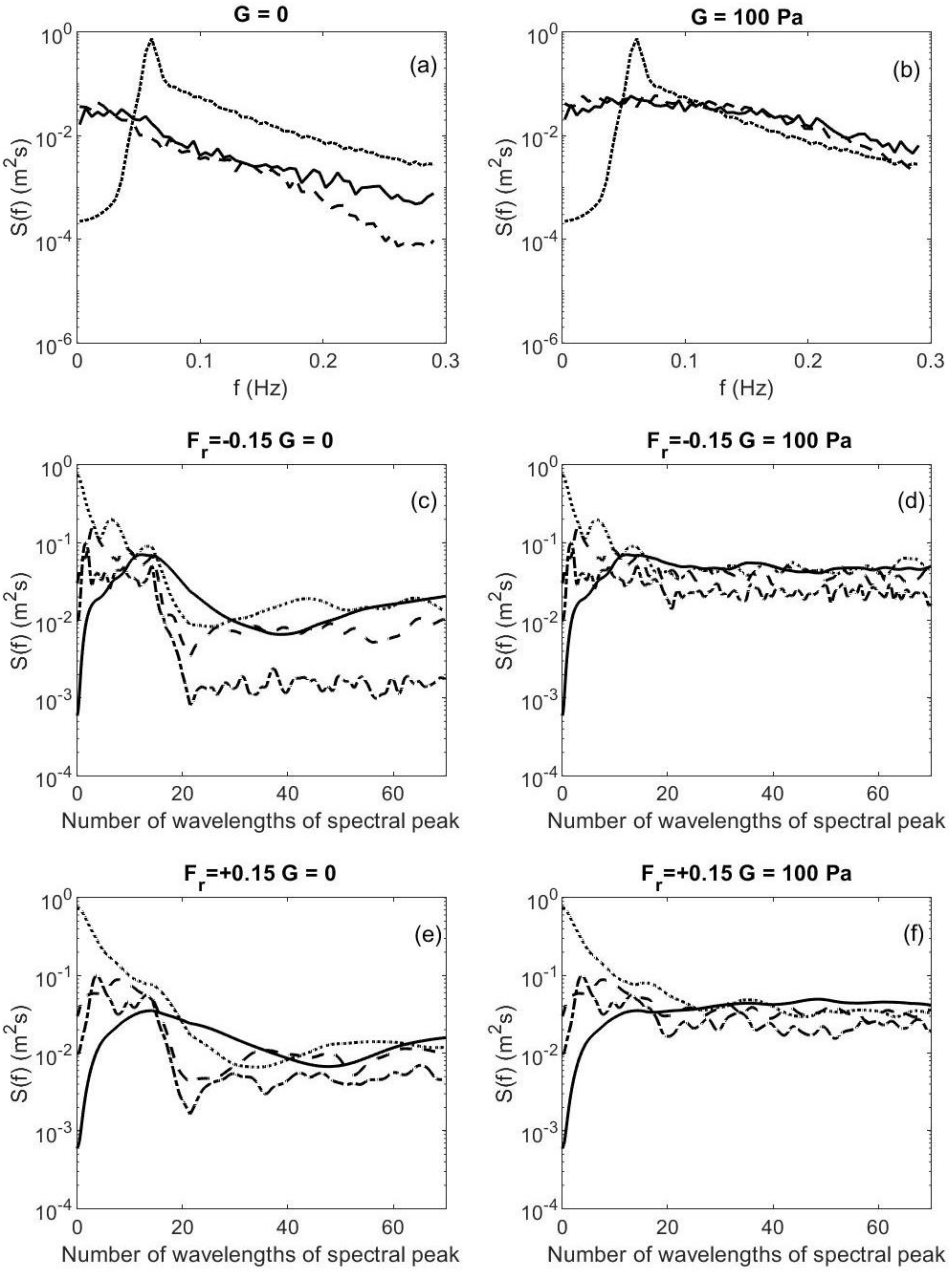

Figure 24. Evolution of random wave spectra with peak frequency of $f_p = 0.0625$ Hz for two values of mud shear modulus of $G = 0$ and 100 Pa ($U_r = 2.08$, $h = 2.00$ m, $d_m = 0.20$ m, and $\rho_m = 1111$ kg/m ^{3}). In (a) and (b): dot-line is initial spectra at $x = 0$, solid-line is spectra at $x = 21L_p$ for $Fr = +0.15$, and dashed-line is spectra at $x = 21L_p$ for $Fr = -0.15$ (L_p is the wavelength of spectral peak). (c-f) show energy density at spectral peak (dot-line), second (dashed line), and third (dashed-dot line) harmonic of the peak, and subharmonic of the peak ($f_p/2$) (solid line).

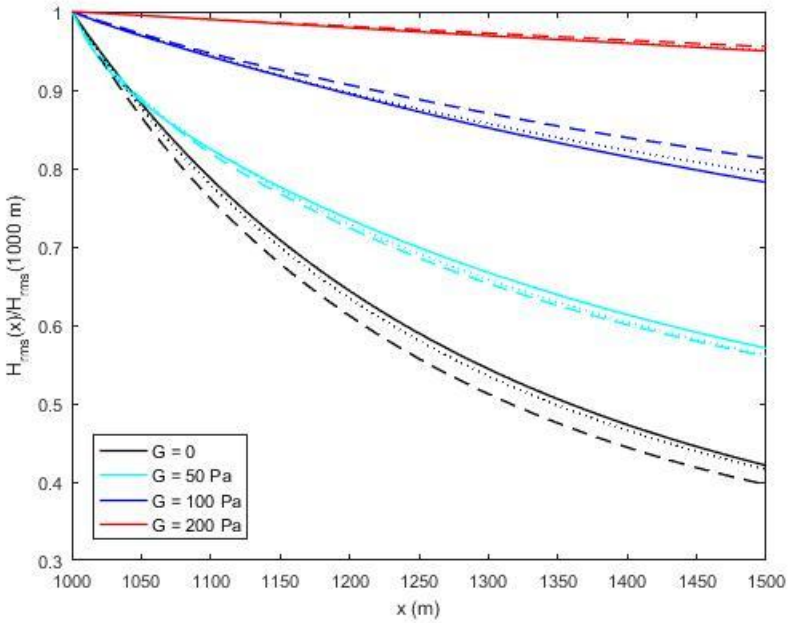

Figure 25. Spatial variation of random wave H_{rms} over viscoelastic mud with shear moduli of $G = 0 - 300$ Pa with $Fr = +0.15$ (solid line), $Fr = 0$ (dot line), and $Fr = -0.15$ (dashed line). Simulation parameters are the same as in Figure (24).

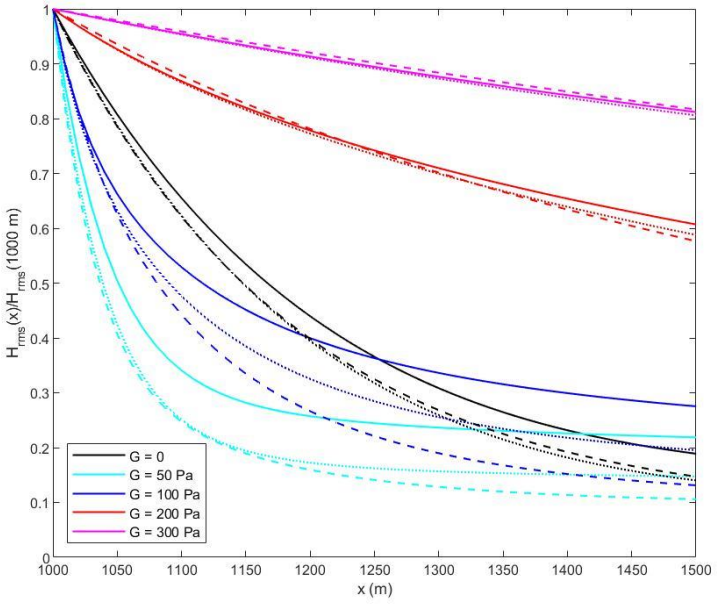

Figure 26. Spatial variation of random wave H_{rms} over viscoelastic mud with shear moduli of $G = 0 - 300$ Pa in presence of currents with $Fr = +0.15$ (solid line), $Fr = 0$ (dot line), and $Fr = -0.15$ (dashed line). Simulation parameters are the same as those in Figure (25) but the spectral peak frequency is 0.28 Hz.

3.3.4 Propagation of cnodial and random wave spectra over a mud layer of arbitrary depth

In this section, the model is used to investigate the effect of mud layer thickness on wave dissipation and evolution. As discussed earlier in the section 2.2.2, the damping mechanism of Liu and Chan (2007) is applicable when the thickness of mud layer is as the same order of magnitude as the thickness of mud boundary layer. However, the Macpherson (1980) model does not apply such limitation on mud layer thickness. To assess the effect of mud layer thickness on waves, we use the dissipation mechanicsm of Macpherson (1980) as the damping coefficient in the model (equation 26) and compare the results with the model that uses the thin-mud model of Liu and Chan (2007). As before, we use both monochromatic and random wave scenarios.

As mentioned in the section 2.2.3, for a thin mud layer the damping rates obtained from the LC and Macpherson (1980) models are similar (Figure (16)). However, the damping rates diverge for the relatively thick mud layer as expected. As shown in Figure (27), damping rates from the Liu and Chan (2007) model are larger than those obtained from the Macpherson (1980) model for viscous mud. For viscoelastic mud with shear modulus of $G = 200$ Pa, the damping rate from Macpherson (1980) is slightly larger than that calculated from the Liu and Chan (2007) for frequencies smaller than 0.22 Hz. However, D_m from the LC model is larger than that from the Macpherson (1980) model for frequencies larger than 0.22 Hz and this difference is most substantial around the resonance frequency, which is 0.26 Hz in this case.

Figure (28) shows the variation of a cnoidal wave spectrum with frequency for $G = 0$ and 200 Pa. Mud specifications are the same as those used to calculate D_m in Figure (17) while water depth and mud thickness are 0.8 m and 0.4 m, respectively. Also, a wider range of frequency ($0 - 1.85$ Hz) is considered. The figure shows the initial spectrum at x = 0 and the spectrum in the end of the mud patch at x = 800 m. Over viscous mud, the LC model (which becomes

identical to the Ng (2000) model when G =0) clearly overestimates damping in low frequencies while it slightly underestimates it in high tail of the spectrum. Over a viscoelastic mud with $G = 200$ Pa, the LC and Macpherson (1980) models give comparable damping rates over high and low frequencies but differ considerably over $0.5 < f < 1$ Hz range.

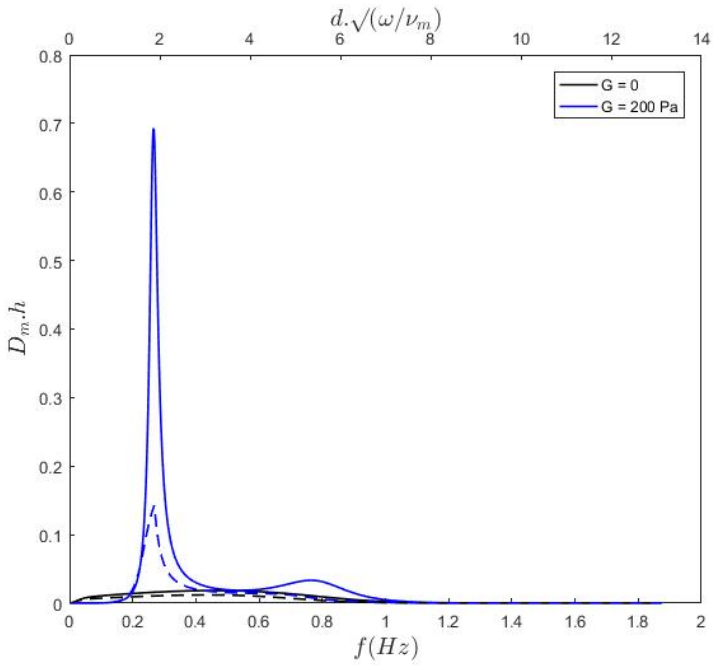

Figure 27. Variation of surface wave damping rate with frequency for mud with shear modulus $G = 0$ and 200 Pa. Solid line: LC model, dashed line: MacPherson (1980) ($\zeta = 100$, $h = 0.8$ m, $d_m = 0.4$ m, and $\rho_m = 1111$ kg/m ^{3}).

Figure (29) shows the corresponding spatial variation of cnodial H_{rms} of the viscous and viscoelastic muds. The figure shows that for the viscoelastic case with $G = 200$ Pa, the Macpherson (1980) and LC models are almost identical while for the viscous case, the Macpherson (1980) model shows weaker damping than the LC model. The damping rate from both models converge for long mud patches.

Next, we investigate the evolution of random waves over relatively thick mud. The shear moduli used are $G = 0{,}200$ Pa and other mud properties are the same as those used in results

shown in Figure (28). Figure (30) shows that in the scenario with viscous mud the wave model with the LC mud model overestimates damping across the spectrum compared to the one with Macpherson (1980) model, consistent with damping pattern of permanent form waves shown in figure (27). The pattern is more complex for the viscoelastic case such that for low frequencies ($f < 0.22$ Hz), the Macpherson (1980) model results in more slightly stronger damping compared to the LC model while it results in weaker damping over higher frequencies ($f > 0.22$ Hz). As seen, the distinction between two models is stronger for the case with viscous mud compared to viscoelastic mud. The same result is seen in the Figure (29) which shows the spatial variation of random wave H_{rms} over viscous and viscoelastic muds. As seen, similar to cnodial scenario for the viscoelastic case with $G = 200$ Pa, the Macpherson (1980) and LC models are almost identical while for the viscous case, the LC model shows stronger damping than the Macpherson (1980) model.

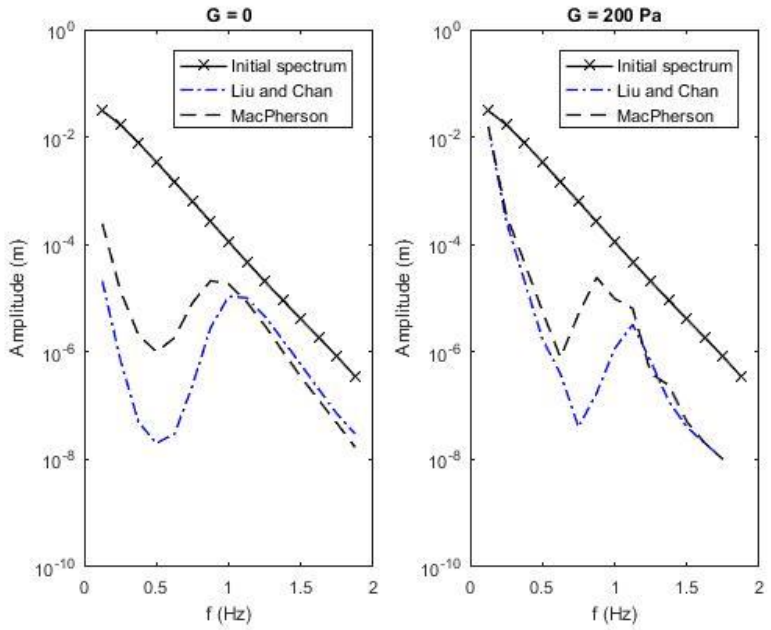

Figure 28. Propagation of cnodial wave spectrum over mud with shear modulus of $G = 0{,}200$ Pa, $h = 0.80$ m, $d_m = 0.40$ m, and $\rho_m = 1111$ kg/m ^{3}

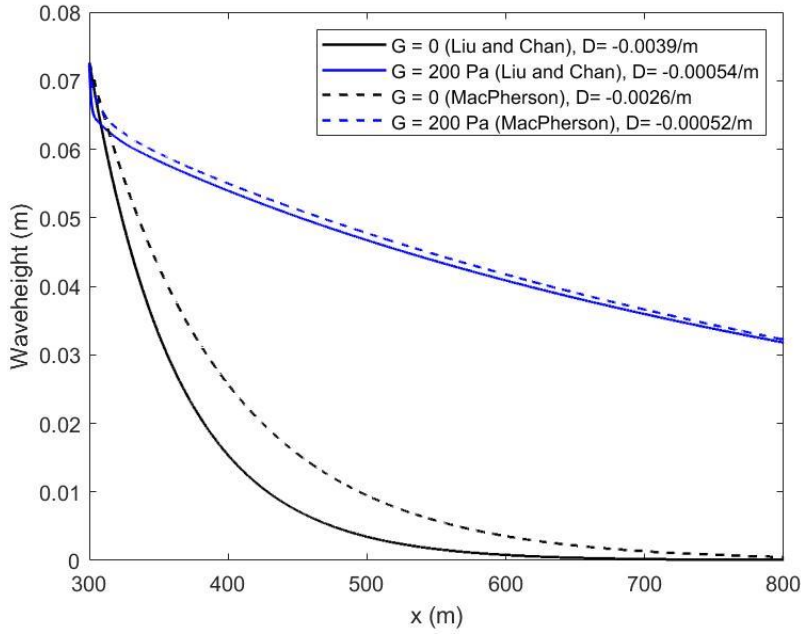

Figure 29. Spatial variation of cnodial wave H_{rms} over viscous ($G = 0$) and viscoelastic mud with shear modulus of $G = 200$ Pa. solid-line: Liu and Chan, dashed-line: MacPherson. The mud patch is located at x = 300-800 m, ζ = 100, h = 0.80 m, $d_m = 0.40$ m, and $\rho_m = 1111$ kg/m ^{3}.

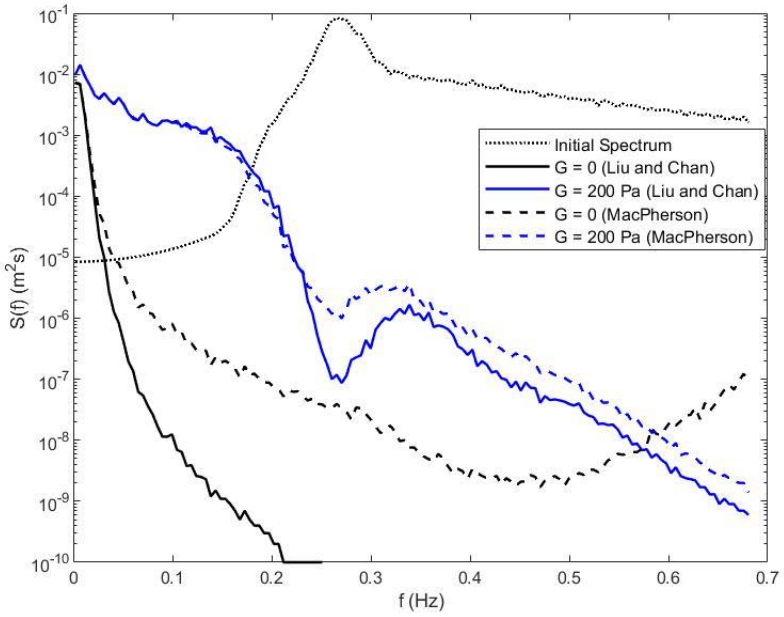

Figure 30. Propagation of random wave spectrum over mud with shear modulus of $G = 0{,}200$ Pa. $h = 0.80$ m, $d_m = 0.40$ m, and $\rho_m = 1111$ kg/m ^{3}.

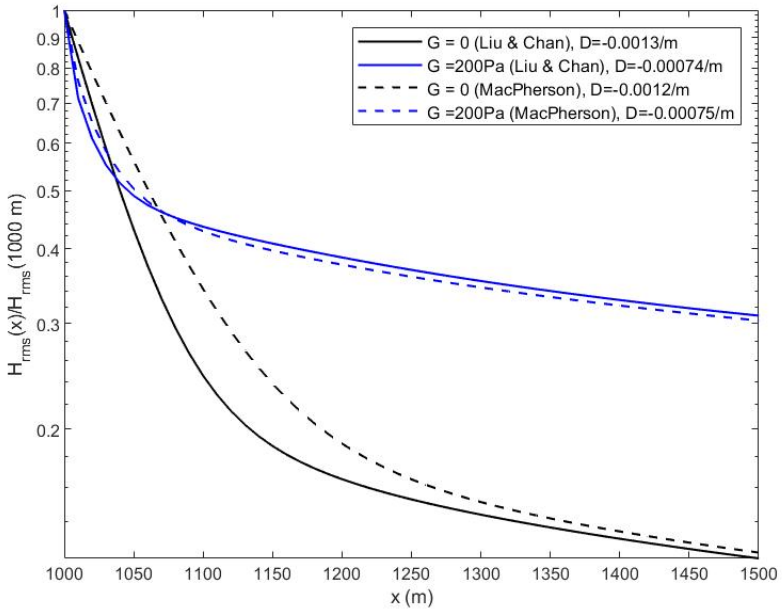

Figure 31. Spatial variation of random wave H_{rms} over viscous ($G = 0$) and viscoelastic mud with shear modulus of $G = 200$ Pa. ζ = 100, h = 0.80 m, $d_m = 0.40$ m, and $\rho_m = 1111$ kg/m ^{3}.

3.4 Summary and Conclusions

In this chapter, we investigate the wave propagation over viscoelastic muds in the presence of currents numerically. A nonlinear frequency-domain phase-resolving wave-current-mud interaction model is improved in two aspects. First, the mud-induced wave mechanism in the model is improved to account for mud elastic effects, thus enabling simulation of wave propagation over viscoelastic muds. Second, a requirement in earlier similar models that assumed the mud layer to be thin is eliminated by incorporating a mechanism for mud-induced wave evolution for mud of arbitrary thickness. The model shows satisfactory comparison with published laboratory data on wave dissipation over mud in the presence of currents. Furthermore, the model compares better with laboratory data on wave height compared to a wave model with viscous mud-induced wave damping mechanism.

The frequency-dependent damping obtained from the thin-mud wave damping model (LC) compares well with the model for arbitrary depth Macpherson (1980) if the mud layer is thin. For viscous muds, the thin-mud model slightly underestimates damping rates while for viscoelastic muds, it yields smaller damping rates than the Macpherson (1980) model in lower frequencies and larger damping rates over higher frequencies. The thin-mud model substantially overestimates damping over viscoelastic mud around the resonance frequency, thus using the LC model or its widely used viscous equivalent, the Ng (2000) model, can result in overestimation or underestimation of wave damping if mud layer is dynamically thick. Co-(counter-)propagating currents decrease (increase) frequency-dependent damping at low frequencies while they increase (decrease) it at higher frequencies. The impact of currents at high frequency increase with increase in mud shear modulus. This effect is observed in both monochromatic and random wave spectra.

First, we investigated the propagation of monochromatic waves over viscoelastic muds. With increasing in shear modulus G, damping decreases regardless of the direction of the current. For $G < 200$ Pa it was observed that there is a frequency before which counter-propagating currents results in stronger dissipation than co-propagating currents while after which the opposite happens. As mud shear modulus increases, this frequency shifts to higher frequencies until it is not seen any longer for the case with shear modulus of $G = 200$ Pa. The trend in dependency of mud-induced dissipation on mud's shear modulus cannot be illustrated only by direct damping and frequency amplitudes are affected by the nonlinear wave-wave interactions. In fact, with deactivating the subharmonic interactions, the frequency amplitudes follows the pattern of direct damping rate. Also, it was shown that the variation of amplitude with frequency is small on the high-frequency tail of the spectrum as reported by earlier studies in the

propagation of waves over viscoelastic mud in the absence of currents (Tahvildari and Sharifineyestani (2019)) and over viscous mud in the presence of currents (Kaihatu and Tahvildari (2012)), denoting that the subharmonic interactions are responsible for damping of higher frequencies regardless of the magnitude of mud shear modulus, presence or direction of currents. Spatial variation of H_{rms} over muds with different shear moduli is described by frequency-dependent damping rate. For viscous mud, the pattern in H_{rms} follows the pattern reported in Kaihatu and Tahvildari (2012) where the opposing currents results in more dissipation than following currents. However, for the viscoelastic muds the pattern was different than the viscous mud such that for the cases with smaller shear moduli (here $G = 50, 100$ Pa), some spatial undulations were seen at the end of mud patch at which mud is most heavily and most weakly dissipated in the presence of a following and an opposing current, respectively. With increasing in shear modulus, (here $G = 200$ Pa), the opposing as well as following current results in low damping but damping in the presence of opposing current is more than that than the following current.

The model is then applied to simulate random wave propagation. For the viscous mud, while there was a comparable damping in the presence of opposing current in low to mid-range frequencies, stronger damping was observed in the presence of opposing current at the end of mud patch as earlier studies were indicated. The distinction between wave damping in the presence of following and opposing currents was smaller over viscoelastic mud in comparison with viscous mud. Since a spectrum with high U_r (2.08) was utilized in the simulations, it expands quickly in frequency regardless of mud shear modulus and current direction and there was not observed apparent peaks in the spectrum at the lee of mud in agreement with the earlier studies indicating that the spectrum with relatively high U_r (2.08) undergoes rapid broadening

over frequency while an spectrum with a smaller Ur (e.g. 0.78) maintains its structure. Like the cnodial scenario, the opposing currents results in more damping than the following currents for the viscous mud while the opposite happens when mud shear modulus increases. It is noteworthy to mention that the spatial undulations seen for a cnoidal wave were not observed for the random waves and this reversal in trend was consistent spatially for all G values.

Resonance is an important property of viscoelastic mud that affects the shape of random wave spectra. We simulated the propagation of a spectrum with a peak frequency equal to resonance frequency which results in highest rate of dissipation and considered the resulted significant wave height. H_{rms} spatially follows the pattern in direct damping such that with increasing in shear modulus up to $G = 50$ Pa it increases and after that decreases. Furthermore, with increasing in shear modulus up to $G = 100$ Pa the opposing current results in more damping than the following current over the domain consistently. However, for $G = 200$ Pa this trend only is seen in the end part of mud patch and the following currents results in more damping in the beginning part of the mud patch. With increasing in shear modulus (here $G = 300$ Pa), the following current strengthens mud-induced damping consistently over the mud patch. It is notable to mention that spatial variability in damping rate of H_{rms} is influenced by G and U such that for $G = 0$ and 50 Pa, initial damping rate of H_{rms} is stronger at the beginning of the mud patch in comparison with the rate at its end where the H_{rms} curve becomes nearly horizontal. However, this variability is weaker for muds with $G = 0$, 200 and 300 Pa.

To investigate the wave propagation over a mud layer of arbitrary depth, both cnodial and random wave solutions were examined for two cases of viscous and viscoelastic mud with $G = 200$ Pa. The distinction between two models is more stronger for viscous mud compared to viscoelastic mud. In the cnodial scenario, for the viscous mud, the LC model overestimates

damping in lower frequencies and underestimate slightly over higher frequencies compared to the Macpherson (1980) model. This overestimation in damping by LC model is seen across the spectrum for viscous mud in the random wave scenario. The pattern is more complicated for the viscoelastic case. In the permanent form solution, while two models show a comparable damping over low and high frequencies, they show considerably different damping over mid-range frequencies ($0.5 < f < 1$). In the random scenario, the Macpherson (1980) model shows slightly stronger damping compared to LC model in low frequencies and weaker damping over higher frequencies. Also, the spatial variation of cnodial and random wave were considered for both viscous and viscoelastic muds. H_{rms} is almost identical for both LC and Macpherson (1980) models for viscoelastic mud while the LC model shows stronger dissipation over the viscous mud compared to Macpherson (1980) model.

CHAPTER 4

THE RELATIONSHIPS BETWEEN HYDRODYNAMIC AND BIOLOGICAL PROPERTIES OF SEGRASSES USING FILED DATA AND COMPUTATIONAL MODELING

In this chapter, we carry out preliminary field data acquisition and analysis of wave and flow in a sheltered estuary over a seagrass meadow in the South Bay, located in the Eastern Shore of Virginia. An array of sensors including pressure gauges and an acoustic doppler velocimeter were deployed to obtain variations in important hydrodynamic variables over the meadow. Furthermore, a computational model for hydrodynamics of wave-vegetation interaction is linked with a computational biophysical model for seagrass growth. This integration results in improvement in prediction of SAV growth as the wave-vegetation model improved information on leaf orientation that controls photosynthetic light absorption by the submerged plant canopy.

It is stressed that both field measurements and computational model coupling are preliminary steps that are taken in investigation of the role of seagrasses in mitigating climate change and sea level rise impacts on coastal infrastructure. Although the present work is limited in scope, it served to build the expertise needed to carry out more comprehensive research in the area. For example, field measurements are carried out only in two areas and detailed field planning was not conducted for the study. However, the field equipment acquired through the study, preliminary design of field work and the subsequent data analysis built the capacity to carry out more detailed field exploration that is currently undergoing in PI's lab.

4.1 Study Area and Instrumentation

The study area is a restored seagrass meadow in the South Bay, located in the Eastern shore of Virginia. Two RBR-SoloD|Wave pressure sensors and one Nortek Aquadopp Acoustic Doppler Current Profiler (ADCP) were deployed in the study site south of an inlet between the wreck island and the Cobb Island as seen in Figure (32). Field measurement were carried out meadow from July 16th to August 16th, 2018. The instruments were deployed in the direction of dominant waves, i.e. northeast/southwest and the distance between instruments was about 10 m.

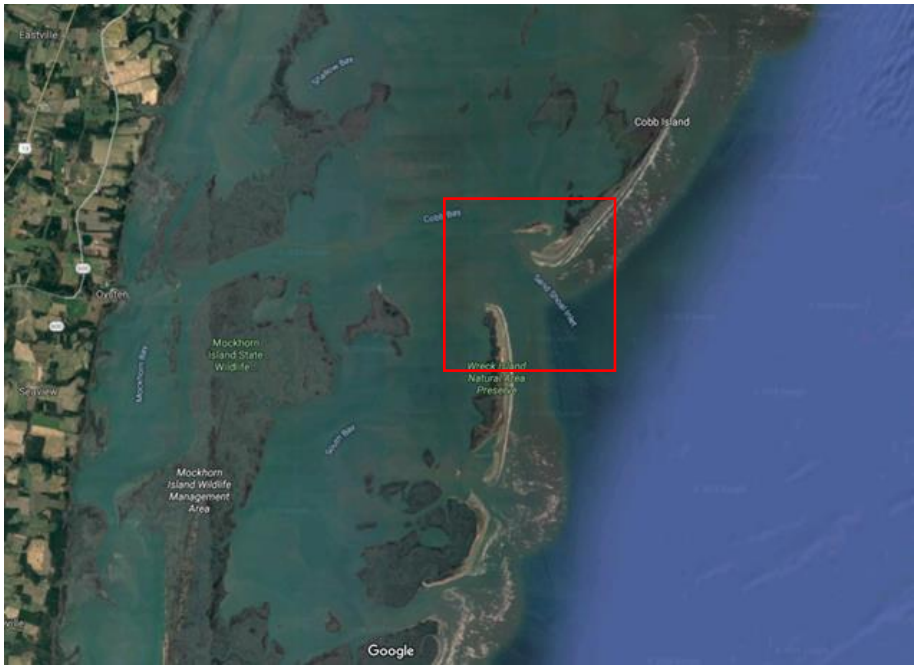

Figure 32. The study area in the Eastern Shore of Virginia (Google Maps)

The Aquadopp collected the current profiles data every 10 minutes and is also equipped with a pressure sensor that measures pressure at 2 Hz frequency over burst (durations at which data is

collected continuously, the sensor goes dormant between bursts) of 5000 seconds. The RBR sensors recorded pressure continuously at the rate of 8 Hz.

4.1 Field Data Analysis

4.1.1 Methods

The data from pressure sensors is processed to obtain instantaneous wave height and wave spectral characteristics. The following equation was applied to calculate the significant wave height (average of top $1/3$ of wave height in the record), H_s:

$$H_s = 4\sqrt{m_0} \qquad (43)$$

where m_0 is the variance of the water surface elevation spectra $S(w)$, which is defined as:

$$m_0 = \int S(w)\, dw \qquad (44)$$

and the mean wave period, T_m, represent the following ratio:

$$T_m = \frac{m_0}{m_1} \qquad (45)$$

where m_1 is the first moment of $S(w)$, defined as:

$$m_1 = \int S(w)^2\, dw \qquad (46)$$

In this study, the following formula is applied to compute wave energy density flux, F, for all frequencies at two RBR locations:

$$F = \frac{1}{2}\rho g a_i^2 C_{g,i} \qquad (47)$$

Where ρ, g, a_i, and $C_{g,i}$ are water density, gravitational acceleration, amplitude of frequency *i*, and group velocity of frequency *i*, respectively. The amplitude of wave frequency *i* is defined as:

$$a_i = \frac{H_i}{2} = \sqrt{2\,S(w)dw} \qquad (48)$$

Wave dissipation between two RBR's locations is computed as (e.g. Nowachi et al., 2017):

$$\epsilon_i = \frac{F_n - F_{n-1}}{\Delta x\, cos\theta} \qquad (49)$$

where Δx is the distance between two points and θ is the angle between the direction of dominant wave and the transect orientation. The total wave energy dissipation is determined by the summation of energy dissipation of each frequency *i*.

4.2 Field Data

4.2.1 Wave characteristics and dissipation using spectral analysis method

Wave characteristics and spectra were calculated with Oceanlyz code version 1.4 (Karimpour, 2017) from water level data measured using RBR pressure sensors. To utilize the code, the record is divided into bursts of 30-minute duration. Variation of significant wave height against time (30 days) for two locations (RBR1615 and RBR1705) are shown in Figure (33). Per this figure, the wave height has a range of 0-0.22 meter at both sites, and as seen, two major events occur in days 26th and 27th of deployment. Wave heights do not show a considerable difference in two locations due to proximity of the deployment points. The variation of wave height against water depth is shown in the Figure (34). As seen, the largest waves occur the largest depth. This is expected as the larger depth can support propagation of larger waves without breaking.

Wave dissipation was computed using Equation 49 and its variation with wave height is shown in Figure (35). The record shows that larger waves undergo stronger dissipation. It is

noted that some waves exhibit negative dissipation which indicates their gain of energy between the two wave gauge locations.

For a more detailed analysis, we selected three different wave bursts and investigated the variation of dissipation with frequency for these bursts. Figure (36) shows the wave dissipation versus frequency for three different times (Burst 895, 1138, and 1316). As seen in the figure, most dissipation occurs in the frequency range of 0.5-0.8 Hz for the bursts 895 and 113 while in burst 1316, most dissipation is seen in the frequency range of 0.4-0.7 Hz. Next, we calculated the wave spectra for these bursts (Figure (37)). As seen in the figures, most of the wave energy was in the range of 0.5-0.8 Hz at both sites. It is seen that there is not a considerable dissipation between two sites as the energy in the two spectra are comparable.

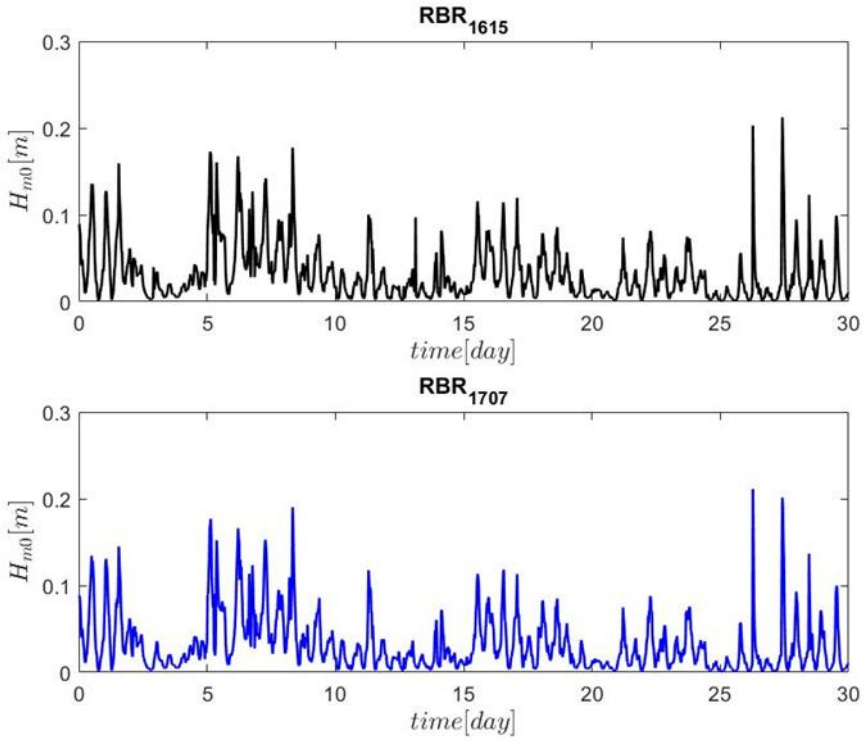

Figure 33. The variation of significant wave height with time for two RBRs of No. 1615, and No. 1707

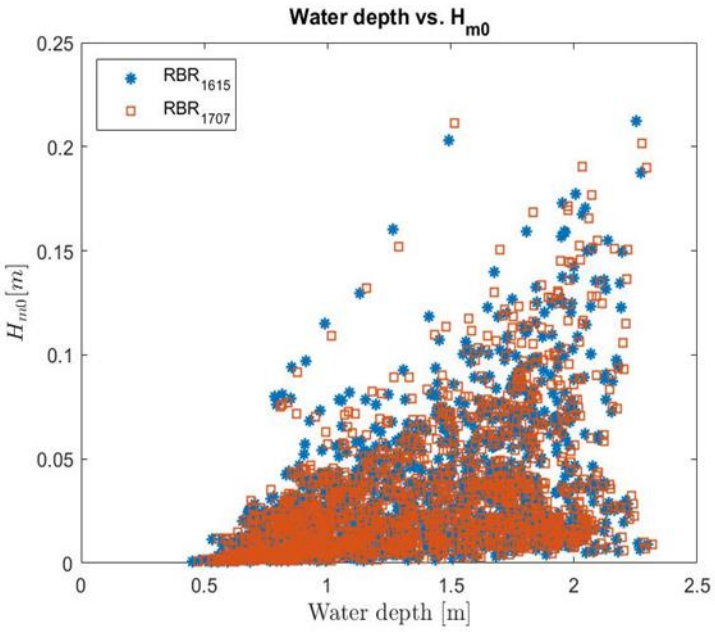

Figure 34. Variation of significant wave height with

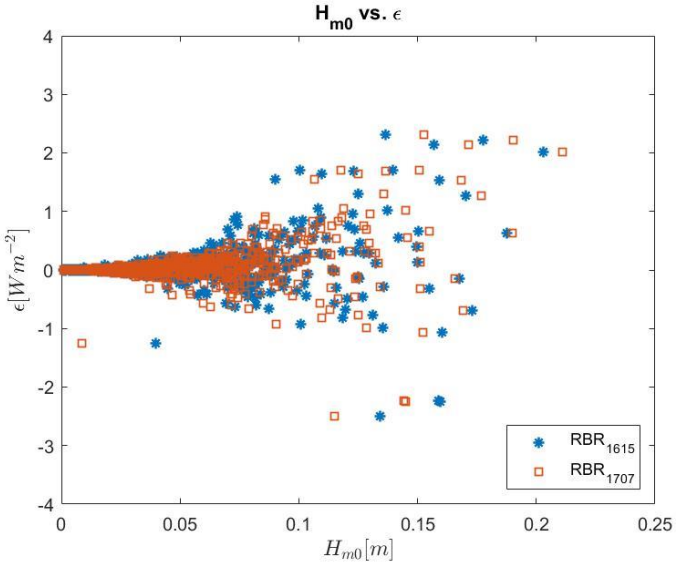

Figure 35. Variation of wave dissipation with significant wave height

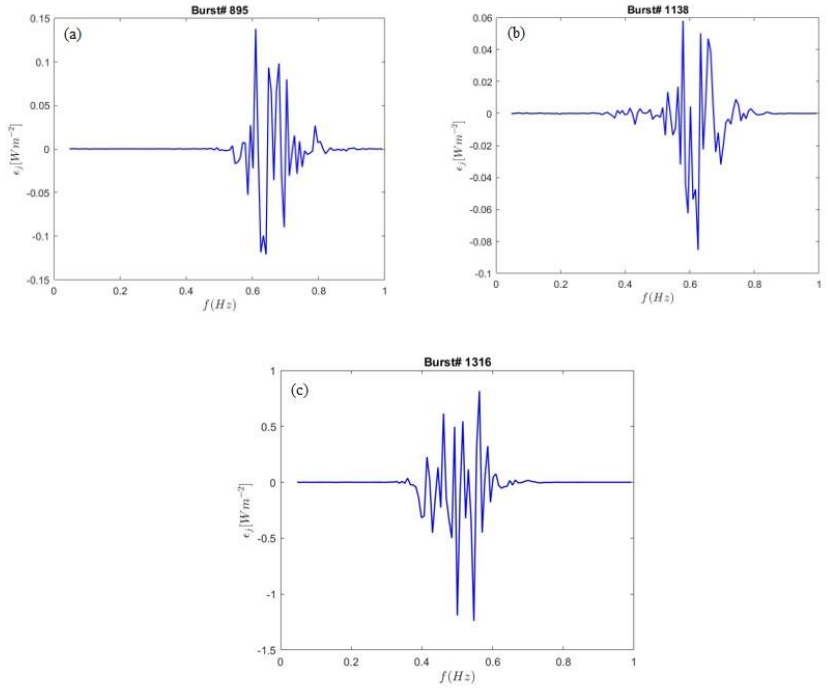

Figure 36. Wave dissipation versus frequency for three different bursts

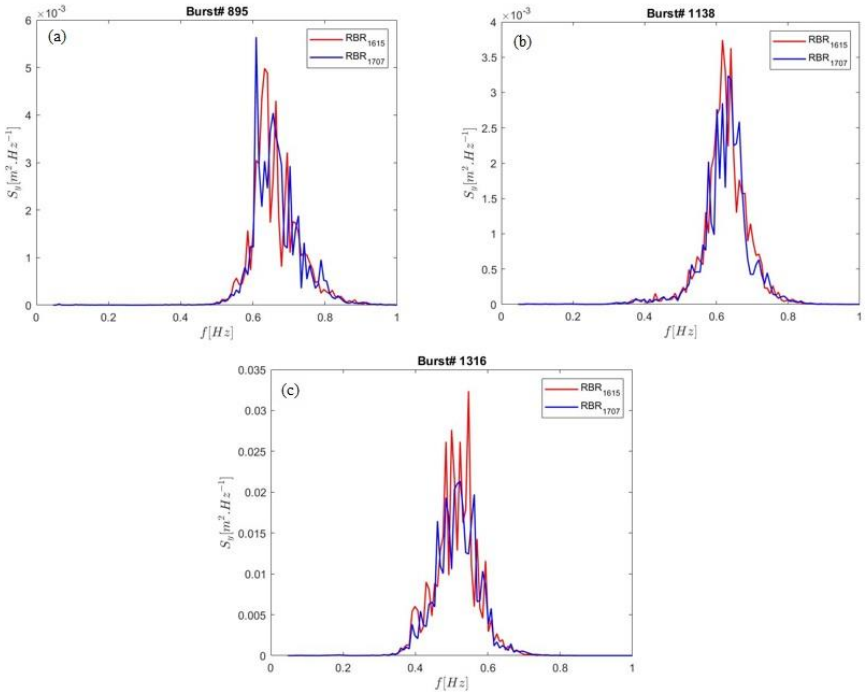

Figure 37. Energy density spectrum of water elevation spectra versus frequency for three different wave bursts

4.3 Computational Modelling

A computational model for hydrodynamics of wave-vegetation interaction is coupled with a computational model for biophysics of seagrass growth. The wave-vegetation interaction model is developed by Tahvildari (2016) and the biophysical seagrass model is the GrassLight model developed by Zimmerman and Gallegos (2016) and Zimmerman, (2003). The GrassLight model is a numerical model of radiative transfer and photosynthesis in submerged plant canopies and has been used to explore the relationship between plant canopy architecture, irradiance distribution, and photosynthesis within plant canopy. In the GrassLight model, the bending angle of the seagrass canopy β is defined as the angle between the canopy orientation and vertical axis and is dependent on the current velocity and initial bending angle. Zimmerman (2003) showed the nonlinear relationship between the leaf bending angle of the seagrass canopy, the total amount of irradiance absorbed ($\sum E_d$), and the biomass-specific photosynthesis (P_d) within the simulated canopies. Zimmerman (2003) quantified the increase in light absorbed by the simulated canopy with increase in leaf bending angle as the horizontal area of projected leaf increases. Furthermore, increasing in the leaf bending angle results in initial increase and eventual decrease in canopy photosynthesis.

With understanding the importance of the leaf bending angle on photosynthesis and light absorbed within the plant, we investigated the effect of leaf bending angle of flexible plant stem in the presence of both current and waves on photosynthesis within the plant. We used the numerical model of Zeller et al. (2014) to simulate the motion of flexible plants under waves and currents. The model uses linear wave theory to force the stems and solves the instantaneous position of vegetation stems. Tahvildari (2016) incorporated this model into a nonlinear Boussineq-type wave model (e.g. Wei et al., 1995, Shi et al., 2013) to enable application of the

Zeller et al. (2014) model for the wave propagation problem. In this preliminary study, we use the basic model of Zeller et al. (2014) and will leave more sophisticated study of nonlinear wave propagation for future studies. In the vegetation stem dynamics model of Zeller et al. (2014), every plant stem is divided in a few segments connected by joints by which the plant stem rigidity is determined. Since there is no limitation on the rigidity of plant segments, the vegetation dynamic model can simulate the motion of arbitrary flexible plants in the presence of wave action. Different forces such as gravity, buoyancy, inertial, drag, lift, and skin fraction were considered in the model. The leaf bending angle was calculated and averaged between segments and used as input in the biological model of *GrassLight* (Zimmerman, 2003; Zimmerman and Gallegos, 2016) which solves seagrass biomass growth. Other parameters that impact flow input to the *GrassLight* model such as current velocity, significant wave height, and initial wave period were obtained from our field measurements explained earlier in section 4.2.

4.3.1 Results of linking biological and hydrodynamic computational models

In the hydrodynamic model, each blade is divided to 10 segments (Figure (38)). The current velocity, significant wave height, and initial wave period were measured at 0.1 m/s, $H_{mo} = 0.16$ m, $T_0 = 1.66$ s, respectively. These values are calculated using our field data analysis.

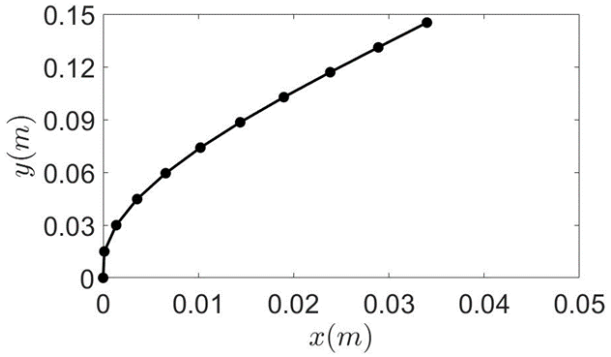

Figure 38. The blade shape after current and wave action; every blade is divided by 10 segments.

Figures (39) and (40) show the variation of leaf bending angle with time in two conditions: without wave (Figure (39)), and with wave action (Figure (40)). As seen in the figures, the numerical model predicts β at a value that is close to the GrassLight model in the presence of uniform currents. But the flow model used in GrassLight underpredicts the blade angle, thus the photosynthesis rate it predicts can be inaccurate. Leaf bending angle changes due to the oscillatory flow by surface waves is shown in Figure (40), and as seen, the error in the GrassLight model estimates for β grows under wave crest. This can intensify the errors in prediction of photosynthesis in submerged seagrass canopies.

Figure (41) shows the variation of the daily biomass-specific photosynthesis of the simulated seagrass canopy with time. As seen in the figure, the daily biomass-specific photosynthesis is constant with time when there is no wave. However, wave velocity results in the sinusoidal variation of daily biomass-specific photosynthesis. The relationship between the leaf bending angle of blade with daily biomass-specific photosynthesis of the seagrass canopy is shown in Figure (42). As seen, photosynthesis decreases with increasing in the leaf bending angle.

4.4 Summary and Conclusions

In conclusion, the existing flow model in the GrassLight model is simplistic and can results in inaccuracies in prediction of seagrass blade bending angle. We show that using realistic parameters obtained from field in this project, the flow in GrassLight underpredicts bending angle by around 10%. If the measured wave action is added to the blade dynamics model, this underprediction can grow up to 25% under wave crest. This discrepancy is translated to

GrassLight model's prediction of biomass-specific photosynthesis (P_d) such that P_d becomes oscillatory with time and peak under wave crest. We note that the average P_d over a wave period is comparable to the average value obtained from uniform currents. However, it should be noted that light irradiance, which is of paramount importance in photosynthesis, is a function of time in the day. Therefore, simple averaging of P_d under waves and comparing it with its values under uniform flow will not reflect the impact of light availability, thus it is imperative to incorporate a time-varying function for blade orientation in models for seagrass photosynthesis for more accurate predictions of P_d. We also note that the seagrass dynamics model used here is for a single blade and the impact of neighboring blades in a canopy on blade orientation is not considered. In a future research, we will investigate vertical variability in the flow on canopy-scale seagrass growth and flow and seagrass impact on sediment resuspension.

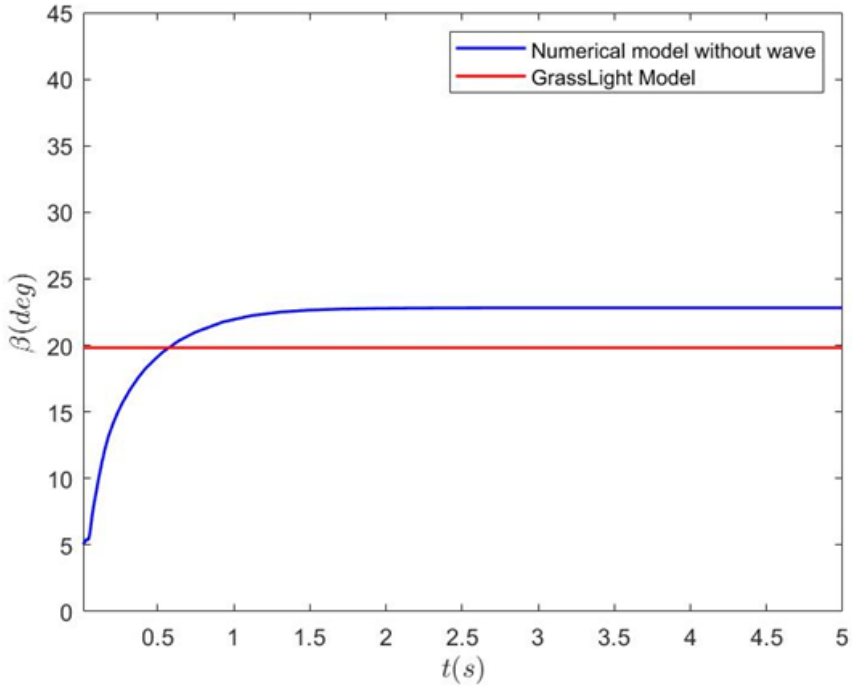

Figure 39. Variation of leaf bending angle with time without wave

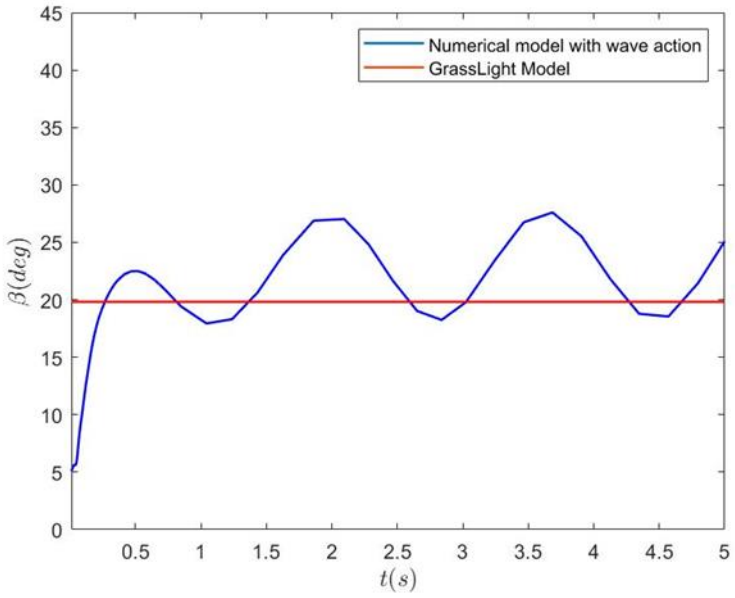

Figure 40. Impact of leaf bending angle under waves on daily biomass-specific photosynthesis of the simulated seagrass canopy with time.

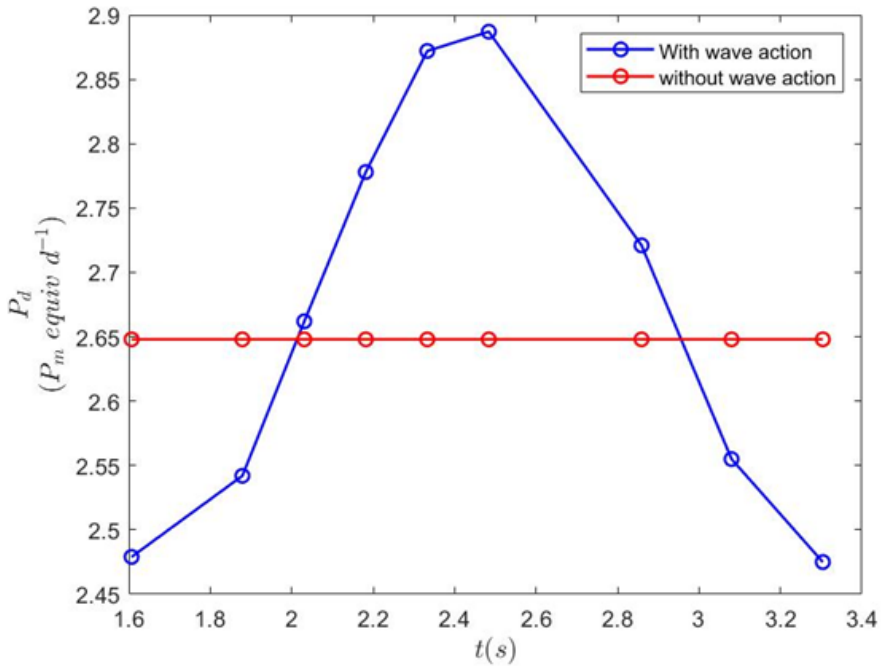

Figure 41. Variation of leaf bending angle with time in the presence of wave

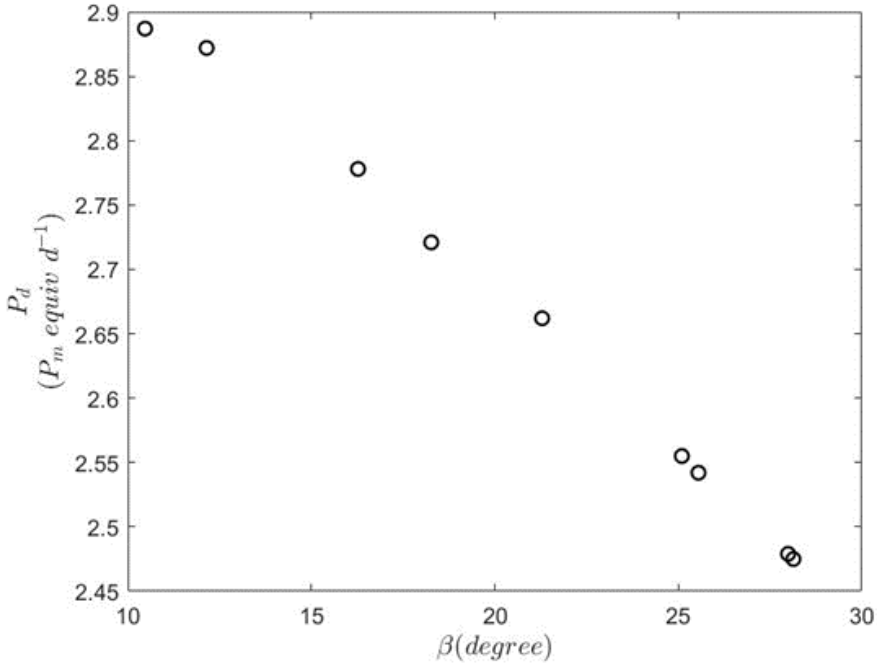

Figure 42. Impact of leaf bending angle on daily biomass-specific photosynthesis of the simulated seagrass canopy.

CHAPTER 5

CONSLUSION AND RECOMMENDATION FOR FUTURE RESEARCH

In this research, the effects of mud viscoelasticity on the evolution of nonlinear waves are investigated through numerical modeling. First, a mud-induced model based on a thin-mud assumption is incorporated in a phase-resolving frequency-domain model to study the mud elastic effect on the propagation of nonlinear wave over viscoelastic muds. Model results indicate that ignoring mud's shear modulus can result in substantial errors in predicting bulk wave characteristics, such as root-mean-square wave height, as well as nonlinear energy transfer across a spectrum that affects the shape of the spectrum. Therefore, adequate characterization of the mud layer and nonlinear wave processes are essential for reliable prediction of surface wave spectrum in the nearshore. Next, the model is improved to include the effect of currents and eliminate the limitation of thin-mud-layer assumption. For this purpose, two models, one based on thin-mud assumption and one for mud of arbitrary thickness, are used to represent mud-induced damping and modulation of surface wave in the wave model. Therefore, the model is a more comprehensive predictive tool for wave propagation in coastal waters. The results show that the effect of opposing and following currents is highly dependent on wave frequency. Following (opposing) current decrease (increase) frequency dependent damping at low frequencies while they increase (decrease) it at higher frequencies. Also, the model based on thin-mud assumption may overestimate or underestimate wave damping. Understanding the interaction between waves, current and mud enable coastal engineers and scientists to better estimate wave forces, understand the fate of sediments in the coastal zone, and predict shoreline erosion.

There are several directions that the present model can be improved. In the present wave-current interaction model, the effect of a boundary layer at water/mud interface is ignored which can be included in the future researches. Furthermore, the results of the present model can be compared with the results of phase-averaged wave model SWAN. As discussed earlier, mud can show various rheological characteristics under different wave conditions. Properties of bottom mud layer such as density, viscosity, and thickness can vary broadly in the filed depending on hydrodynamic conditions and consolidation. Verifying the existing model with field measurements can be the subject of future research.

Last but not least, a preliminary field measurement of wave and flow over a seagrass meadow is conducted. In addition, a computational model for hydrodynamics of wave-vegetation interaction is linked to a computational biophysical model for seagrass growth. As a result of this integration, the wave-vegetation model provides improved information on leaf orientation that controls photosynthetic light absorption by the submerged plant canopy. Future research can investigate vertical variability in the flow on canopy-scale seagrass growth and flow and seagrass impact on sediment resuspension.

REFERENCES

Almashan N, Dalrymple R., 2015. Damping of waves propagating over a muddy bottom in deep water: Experiment and theory. J Coastal Engineering, 105:34-46.

Ardhuin, F., O'Reilly, W., Herbers, T., Jessen, P., 2003. Swell transformation across the continental shelf. part i: Attenuation and directional broadening. Journal of Physical Oceanography 33, 1921–1939.

Beyramzade, M., Siadatmousavi, S.M., 2017. Implementation of viscoelastic mud-induced energy attenuation in the third-generation wave model, swan. Ocean Dynamics URL: https://doi.org/10.1007/s10236-017-1118-4, doi:10.1007/s10236-017-1118-4.

Bouws E, Gunther H, Rosenthal W, Vincent C., 1985. Similarity of the wind wave spectrum in finite depth water: 1. spectral form. Journal of Geophysical Research: Oceans; 90(C1):975–86.

Bretherton F, Garrett C., 1968. Wavetrains in inhomogeneous moving media. ProcRoy Soc Ser A 302; 529–54.

Chan, I., Liu, P., 2009. Responses of bingham-plastic muddy seabed to a surface solitary wave. J Fluid Mech 618, 155–180.

Chawla A, Kirby J., 2002. Monochromatic and random wave breaking at blocking points. J Geophys Res,107: doi:10.1029/2001 JC001042.

Chen Q, Madsen P, Basco D., 1999. Current effects on nonlinear interactions of shallow-water waves. J Wtrway Port Coast Oc Eng, 125:176–86.

Chou, H.T., Foda, M.A., Hunt, J.R., 1993. Rheological response of cohesive sediments to oscillatory forcing. Nearshore and estuarine cohesive sediment transport, 126–147.

Crapper G., 1972. Nonlinear gravity waves on steady non-uniform currents. J of Fluid Mech, 52:713–24.

Dalrymple, R., Liu, P., 1978. Waves over soft muds: a two-layer fluid model. J. Physical Oceanography 8, 1121–1131.

De Wit, P.J., 1996. Liquefaction of cohesive sediments caused by waves. Oceanographic Literature Review 3, 252.

Eldeberky Y, Battjes JA., 1996. Spectral modeling of wave breaking: application to boussinesq equations. Journal of Geophysical Research: Oceans, 101(C1):1253–64.

Elgar S, Raubenheimer B., 2008. Wave dissipation by muddy seafloors. Geophysical Research Letters, 35(7).

Elgar, S., Raubenheimer, B., 2008. Wave dissipation by muddy seafloors. Geophysical Research Letters 35.

Gade, H., 1958. Effects of a nonrigid, impermeable bottom on place waves in shallow water. J. Marine Research 16, 61–82.

Hill, D., Foda, M., 1999. Effects of viscosity and elasticity on the nonlinear resonance of internal waves. Journal of Geophysical Research: Oceans 104, 10951–10957.

Hill, D.F., Foda, M.A., 1996. Subharmonic resonance of short internal standing waves by progressive surface waves. J. Fluid Mech. 321, 217–233.

Holland, K., Elmore, P., 2008. A review of heterogeneous sediments in coastal environments. Earth-Science Reviews 89, 116–134.

Hsiao, S.V., Shemdin, O.H., 1980. Interaction of ocean waves with a soft bottom. 685 J. Phys. Oceanogr. 10, 605–610.

Hsu, W., Hwung, H., Hsu, T., Torres-Freyermuth, A., Yang, R., 2013. An experimental and numerical investigation on wave-mud interactions. Journal of Geophysical Research: Oceans 118, 1126–1141.

Jain, M., Mehta, A.J., 2009. Role of basic rheological models in determination 690 of wave attenuation over muddy seabeds. Cont. Shelf Res. 29(3), 642–651.

Jamali, M., Seymour, B., Lawrence, G.A., 2003a. Asymptotic analysis of a surface-interfacial wave interaction. Physics of Fluids (1994-present) 15, 47– 55.

Jamali, M., Seymour, B.S., Lawrence, G.A., 2003b. A note on the resonant 695 interaction between a surface wave and two internal waves. J. Fluid Mech. 491, 1–9.

Jiang, F., Mehta, A.J., 1995. Mudbanks of the southwest coast of India iv: mud viscoelastic properties. Journal of Coastal Research, 918–926.

Jiang F, Mehta AJ., 1996. Mudbanks of the southwest coast of India. v: Wave attenuation. Journal of Coastal Research, 890–7.

Jiang, F., Mehta, A.J., 1996. Mudbanks of the southwest coast of India. v: Wave attenuation. Journal of Coastal Research, 890–897.

Kaihatu J. Application of a nonlinear frequency domain wave current interaction model to shallow water recurrence in random waves. J Ocean Modeling 2009; 26:190–250.

Kaihatu, J., Sheremet, A., Holland, K., 2007. A model for the propagation of nonlinear surface waves over viscous muds. J. Coastal Engineering 54, 752–764.

Kaihatu, J.M., Ardani, S., Goertz, J.T., Venkattaramanan, A., Sheremet, A., 2018. Wave Dissipation Mechanisms in Spectral Phase-Resolved Nonlinear Wave Models. Chapter 7. pp. 235–262.

Kaihatu JM. Improvement of parabolic nonlinear dispersive wave model. Journal of waterway, port, coastal, and ocean engineering 2001;127(2):113–21.

Kaihatu, J.M., Kirby, J.T., 1995. Nonlinear transformation of waves in finite water depth. Phys. Fluids 7, 1903–1914.

Kaihatu, J.M., Tahvildari, N., 2012. The combined effect of wave-current interaction and mud-induced damping on nonlinear wave evolution. Ocean Modelling 41, 22–34.

Karimpour A., and Q. Chen (2017). Wind Wave Analysis in Depth Limited Water Using OCEANLYZ, a MATLAB toolbox. Computers & Geosciences, 106, 181-189

Kirby J. Higher-order approximations in the parabolic equation method for water waves. J Geophys Res 1986; 91:933–52.

Kirby, J.T., Kaihatu, J.M., 1997. Structure of frequency domain models for random wave breaking, in: Coastal Engineering 1996, pp. 1144–1155.

Kranenburg, W., Winterwerp, J., de Boer, G., Cornelisse, J., Zijlema, M., 2011. Swan-mud: Engineering model for mud-induced wave damping. Journal of hydraulic engineering 137, 959–975.

Liao, Y.P., Safak, I., Kaihatu, J., Sheremet, A., 2015. Nonlinear and directional effects on wave predictions over muddy bottoms: central chenier plain coast, western louisiana shelf, usa. Ocean Dynamics 65, 1567–1581. doi:10.1007/s10236-015-0887-x.

Liu, P.L.F., Chan, I.C., 2007. A note on the effects of a thin visco-elastic mud layer on small amplitude water-wave propagation. Coastal Engineering 54, 233–247.

Maa, J.Y., Mehta, A., 1990. Soft mud response to water waves. j. waterw., port. J. Coastal Ocean Eng. 116, 634–650.

Macpherson, H., 1980. The attenuation of water waves over a non-rigid bed. J. Fluid Mech. 97, 721–742.

Mei, C.C., Krotov, M., Huang, Z., Huhe, A., 2010. Short and long waves over a muddy seabed. J Fluid Mech 643, 33–58.

Mei, C.C., Liu, K., 1987. A bingham-plastic model for a muddy seabed under long waves. J Geophys. Res. 92, 14581–14594.

Mendez FJ, Losada IJ. 2004. A perturbation method to solve dispersion equations for water waves over dissipative media. Coastal Engineering, 51:81–9.

Ng, C.O., 2000. Water waves over a muddy bed: a two-layer stokes' boundary layer model. Coastal Engineering 40, 221–242.

Ng C.O., CHIU HS., 2009. Use of mathcad as a calculation tool for water waves over a stratified muddy bed. Coastal Engineering Journal - COAST ENG J., 51. doi:10.1142/S0578563409001904.

Ng, C.O., Zhang, X., 2007. Mass transport in water waves over a thin layer of 735 soft viscoelastic mud. Journal of Fluid Mechanics 573, 105–130.

Nowachi, D. J. A. Beudin, and N. K. Ganju. (2017). Spectral wave dissipation by submerged aquatic vegetation in a back-barrier estuary. Limnol. Oceanogr. 00, doi: 10.1002/Ino.10456

Nwogu, O., Demirbilek, Z., 2010. Infragravity wave motions and runup over shallow fringing reefs. Journal of waterway, port, coastal, and ocean engineering 136, 295–305.

Philips OM., 1981. Wave interactions- the evolution of an idea. J Fluid Mech, 106:215–27.

Piedra-Cueva, I., 1993. On the response of a muddy bottom to surface water waves. J. Hydraul. Res. 31, 681–696.

Radder, A., 1979. On the parabolic equation method for water-wave propagation. J. Fluid Mech. 95, 159–176.

Rogers, W., Orzech, M., 2013. Implementation and testing of ice and mud source functions in WAVEWATCH III, NRL Memorandum Report. Technical Report. NRL/MR/7320-13-9462.

Safak, I., Sheremet, A., Davis, J., Kaihatu, J.M., 2017. Nonlinear wave dynamics in the presence of mud-induced dissipation on atchafalaya shelf, louisiana, usa. Coastal Engineering 130, 52–64.

Sharifineyestani, E., Tahvildari, N., 2019. Numerical modeling of current effects on nonlinear surface wave propagation over viscoelastic mud. Submitted to the journal of Ocean Modeling.

Sheremet, A., Stone, G.W., 2003. Observations of nearshore wave dissipation over muddy seabeds. J. Geophys. Res. 108, 3357–3368.

Shi, F., Kirby, J. T., Harris, J. C., Geiman, J. D. and Grilli, S. T., 2012, A high-order adaptive time-stepping TVD solver for Boussinesq modeling of breaking waves and coastal inundation, Ocean Modelling, 43-44, 36-51.

Smith R. Giant waves., 1976. J Fluid Mech, 77:417–31.

Smith R, Sprinks T., 1975. Scattering of surface waves by a conical island. J Fluid Mech, 72:373–84.

Soltanpour, M., Samsami, F., 2011. A comparative study on the rheology and wave dissipation of kaolinite and natural hendijan coast mud, the persian gulf. J Ocean Dyn 61, 295–309, doi:10.1007/s10236–011–0378–7.

Tahvildari, N., Jamali, M., 2012. Cubic nonlinear analysis of interaction between a surface wave and two interfacial waves in an open two-layer fluid. Fluid Dynamics Research 44, 055502.

Tahvildari, N., Kaihatu, J.M., 2011. Optimized determination of viscous mud properties using a nonlinear wave–mud interaction model. Journal of Atmospheric and Oceanic Technology 28, 1486–1503.

Tahvildari, N., Kaihatu, J.M., Saric, W.S., 2016. Generation of long subharmonic internal waves by surface waves. Ocean Modelling 106, 12–26.

Tahvildari N, Sharifineyestani E. 2019. A numerical study on nonlinear surface wave evolution over viscoelastic mud. 154:103557. doi: https://doi.org/10.1016/j.coastaleng.

Tahvildari, N. (2016), Numerical modeling of the interactions between nonlinear waves and arbitrarily flexible vegetation. Proceedings of 35th International Conference on Coastal Engineering.

Torres-Freyermuth, A., Hsu, T.J., 2010. On the dynamics of wave-mud interaction: A numerical study. Journal of Geophysical Research: Oceans 115.

Torres-Freyermuth, A., Hsu, T.J., 2014. On the mechanisms of low-frequency wave attenuation by muddy seabeds. Geophysical Research Letters 41, 2870-2875.

Turpin FM, Benmoussa C, Mei C., 1983. Effects of slowly varying depth and current 730 on the evolution of a stokes wavepacket. J Fluid Mech, 132:1–23.

Wei, G. and Kirby, J. T., 1995, A time-dependent numerical code for extended Boussinesq equations, Journal of Waterway, Port, Coastal and Ocean Engineering, 121, 251-261.

Wells, J.T., Coleman, J.M., 1981. Physical processes and fine-grained sediment dynamics, coast of surinam, south america. J. Sediment. Petrol. 54, doi: 10.1306/212F7E1E–2B24–11D7–8648000102C1865D.

Winterwerp, J., De Graaff, R., Groeneweg, J., Luijendijk, A., 2007. Modelling of wave damping at guyana mud coast. Coastal Engineering 54, 249–261.

Zeller, R. B., J. S. Weitzman, M. E. Abbett, F. J. Zarama, O. B. Fringer, J. R. Koseff. (2014). Improved parameterization of seagrass blade dynamics and wave attenuation based on numerical and laboratory experiments. Limnology and Oceanography 59 (1), 251–266.

Zhao, Z.D., Lian, J.J., Shi, J.Z., 2006. Interactions among waves, current, and mud: numerical and laboratory studies. Advances in water resources 29, 1731–1744.

Zimmerman, R. C., (2003). A biooptical model of irradiance distribution and photosynthesis in seagrass canopies. Limnol. Oceanogr. 48:568-585.

Zimmerman, R. C., C. L. Gallegos. (2016), GrassLight 2.14, A Simulation Model of Radiative Transfer and Photosynthesis in Submerged Plant Canopies, Old Dominion University.